THE UNIVERSITY OF
WARWICK

Library Declaration and Deposit Agreement

1. STUDENT DETAILS

Please complete the following:

Full name: Joseph Henry Harris

University ID number: 0505263

2. THESIS DEPOSIT

2.1 I understand that under my registration at the University, I am required to deposit my thesis with the University in BOTH hard copy and in digital format. The digital version should normally be saved as a single pdf file.

2.2 The hard copy will be housed in the University Library. The digital version will be deposited in the University's Institutional Repository (WRAP). Unless otherwise indicated (see 2.3 below) this will be made openly accessible on the Internet and will be supplied to the British Library to be made available online via its Electronic Theses Online Service (EThOS) service.
[At present, theses submitted for a Master's degree by Research (MA, MSc, LLM, MS or MMedSci) are not being deposited in WRAP and not being made available via EthOS. This may change in future.]

2.3 In exceptional circumstances, the Chair of the Board of Graduate Studies may grant permission for an embargo to be placed on public access to the hard copy thesis for a limited period. It is also possible to apply separately for an embargo on the digital version. (Further information is available in the *Guide to Examinations for Higher Degrees by Research*.)

2.4 *If you are depositing a thesis for a Master's degree by Research, please complete section (a) below. For all other research degrees, please complete both sections (a) and (b) below:*

(a) Hard Copy

I hereby deposit a hard copy of my thesis in the University Library to be made publicly available to readers (please delete as appropriate) EITHER immediately OR ~~after an embargo period~~ of ..... months/years as agreed by the Chair of the Board of Graduate Studies.

I agree that my thesis may be photocopied. YES / ~~NO~~ (*Please delete as appropriate*)

(b) Digital Copy

I hereby deposit a digital copy of my thesis to be held in WRAP and made available via EThOS.

Please choose one of the following options:

EITHER My thesis can be made publicly available online. YES / ~~NO~~ (*Please delete as appropriate*)

OR My thesis can be made publicly available only after.....[date] (Please give date)
~~YES / NO~~ (*Please delete as appropriate*)

OR My full thesis cannot be made publicly available online but I am submitting a separately identified additional, abridged version that can be made available online.
~~YES / NO~~ (*Please delete as appropriate*)

OR My thesis cannot be made publicly available online. ~~YES / NO~~ (*Please delete as appropriate*)

3. **GRANTING OF NON-EXCLUSIVE RIGHTS**

Whether I deposit my Work personally or through an assistant or other agent, I agree to the following:

Rights granted to the University of Warwick and the British Library and the user of the thesis through this agreement are non-exclusive. I retain all rights in the thesis in its present version or future versions. I agree that the institutional repository administrators and the British Library or their agents may, without changing content, digitise and migrate the thesis to any medium or format for the purpose of future preservation and accessibility.

4. **DECLARATIONS**

(a) I DECLARE THAT:

- I am the author and owner of the copyright in the thesis and/or I have the authority of the authors and owners of the copyright in the thesis to make this agreement. Reproduction of any part of this thesis for teaching or in academic or other forms of publication is subject to the normal limitations on the use of copyrighted materials and to the proper and full acknowledgement of its source.
- The digital version of the thesis I am supplying is the same version as the final, hard-bound copy submitted in completion of my degree, once any minor corrections have been completed.
- I have exercised reasonable care to ensure that the thesis is original, and does not to the best of my knowledge break any UK law or other Intellectual Property Right, or contain any confidential material.
- I understand that, through the medium of the Internet, files will be available to automated agents, and may be searched and copied by, for example, text mining and plagiarism detection software.

(b) IF I HAVE AGREED (in Section 2 above) TO MAKE MY THESIS PUBLICLY AVAILABLE DIGITALLY, I ALSO DECLARE THAT:

- I grant the University of Warwick and the British Library a licence to make available on the Internet the thesis in digitised format through the Institutional Repository and through the British Library via the EThOS service.
- If my thesis does include any substantial subsidiary material owned by third-party copyright holders, I have sought and obtained permission to include it in any version of my thesis available in digital format and that this permission encompasses the rights that I have granted to the University of Warwick and to the British Library.

5. **LEGAL INFRINGEMENTS**

I understand that neither the University of Warwick nor the British Library have any obligation to take legal action on behalf of myself, or other rights holders, in the event of infringement of intellectual property rights, breach of contract or of any other right, in the thesis.

Please sign this agreement and return it to the Graduate School Office when you submit your thesis.

Student's signature: [redacted] Date: 21/01/14

Stability of the Flow over a Rough, Rotating Disk

By Joseph H. Harris

A thesis submitted to the
University of Warwick
for the degree of
Doctor of Philosophy

University of Warwick, School of Engineering

August 2013

Contents

Table of Figures

Acknowledgements

I would like to thank my supervisor, Prof. Peter Thomas for his guidance and help throughout my research, and my unofficial co-supervisor Dr. Stephen Garrett who supervised from afar, and provided invaluable assistance to get the code working. I would like to acknowledge the financial support from the Engineering and Physical Sciences Research Council, without which I could not have completed this PhD. Finally, I would like to thank my parents, my sister and of course Izzy, who all prevented me from going mad during the last four years. I'm not sure they fully succeeded.

Declaration

This thesis is the result of research carried out between the dates of October 2009 and August 2013 in the School of Engineering of the University of Warwick. I declare that this thesis has not been submitted for a degree or diploma at another university or learning establishment. It is the result of my own work, except where explicitly stated. It consists of 34,526 words and 67 figures.

Summary

This thesis is concerned with discovering the effect of a distributed roughness on the boundary-layer stability of a rotating disk. The investigation uses both a local, linear stability analysis and machined aluminium disks rotating in water in conjunction with a hot-film anemometer system. The stability analysis applies a sinusoidal function to the surface of the disk which mimics anisotropic roughness similar to a grooved record. The new surface is used with the governing equations in order to calculate the new mean flow profiles for the now grooved surface at a variety of roughnesses. These new flow profiles are then used in the stability analysis.

The results show that the roughness has the effect of increasing the stability of the cross-flow instability mechanism by decreasing the velocity of the radial wall jet. Conversely, increasing roughness levels cause the growth of the streamline-curvature instability mechanism, something which is probably caused by a thickening of the boundary-layer seen in the velocity profiles. These two outcomes result in a predicted switch of the dominant instability mechanism on the disk.

The experimental arrangement confirms the results of the mean velocity profiles, and appears to show the appearance of the enlarged streamline-curvature instability at higher roughness levels. This instability appears as a small burst of frequencies at low Reynolds numbers centred on the numerically predicted neutral curve lobe. This burst dies down as it moves downstream, but appears to increase the amount of energy in the flow which hastens the onset of the cross-flow instability earlier than predicted. Before the emergence of this other mode at lower roughness levels, the roughness appears to delay the onset of the spiral vortices by pushing back the location of the initial cross-flow instability.

The experimental results also see a decrease in the number of spiral vortices seen around the circumference of the disk as roughness is increased. This result is thought to be due to the decrease in the growth rate of the cross-flow instability rather than any switch in the neutral curve positions.

1 Introduction

The problem of the flow over a rotating disk has been a prominent one for many decades. The subject has garnered much interest over the years for a multitude of reasons. The fluid dynamics community find it useful due to the clean and repeatable conditions for turbulence transition, and ease in which it allows one to study a three-dimensional flow field (Lingwood 1995a). It is of interest to the aviation industry because its similarity to a swept wing boundary-layer allows easier problem formation without the more elaborate geometries (Gregory et al. 1955). Since it is relatively hard to carry out experiments on scaled swept wing models in wind tunnels, the ability to perform such experiments on a rotating disk facility instead is a great advantage (Healey 2007). Another benefit is that the disk boundary-layer has a well-known exact similarity solution for the Navier-Stokes equations which features a boundary-layer of constant thickness, making numerical calculations a lot simpler than for a swept wing (Kármán 1921). Finally, there are of course industrial processes which involve rotating disk surfaces in their own right, about which one needs to know as much as possible to maximise the effectiveness of the process. Examples include rotating impellers (Visser et al. 1999), centrifugal pumps (Adkins & Brennen 1988), and chemical vapour deposition processes (Coltrin et al. 1989).

Roughness meanwhile, has historically been thought of as detrimental to boundary-layer flows, and in particular to pipe flows, where the effects of roughness on the pressure losses in pipes has been studied for hundreds of years (see the history by

Brown (2002)). Similarly, a review of the available data on the effect of roughness on the flat plate boundary-layer is presented by Dryden (2012).

More recently however, the effect of roughness on boundary-layer flow has developed a greater importance, since it was discovered that certain kinds of roughness could be beneficial to the stability of the flow and help control its structure and reduce drag (Carpenter 1997). While roughness is generally considered a scourge of a stable flow, many studies have found that carefully applied rough surfaces can delay transition to turbulence on certain geometries, and therefore studies in this area are clearly beneficial (Carrillo et al. 1996; Fransson et al. 2006).

The locus of the two subjects contains little in the way of stability studies, instead focusing mainly on how roughness affects the torque, or heat transfer of the rotating disk. Any stability research done on the rotating disk has dealt with smooth disks, or disks with one or more roughness elements attached to the surface. For this reason, the aim of this project is to study the effect of a *distributed* roughness on the incompressible rotating disk boundary-layer. It intends to discover how a distributed roughness can affect the points of initial instability, the transition location and the behaviour of the stationary vortices. The approach taken uses both numerical and experimental techniques to carry out a linear stability analysis which is then complemented by hot film measurements taken in a water tank for rotating disks with varying levels of roughness. The numerical method is an extension of the stability work done by Lingwood (1995a) and Garrett (2002) using a method developed by Yoon et al. (2007) to add roughness to a disk surface numerically.

The thesis is structured in the following way: Firstly, a review of the current literature surrounding the problem is summarised in Chapter 2. In Chapter 3 the numerical problem is formulated before performing the linear stability analysis and discussing the results in Chapter 4. In Chapter 5 the experimental set-up and procedures are briefly outlined and then the data gained from it is analysed in Chapter 6. Finally conclusions are drawn in Chapter 7.

2 Literature review

2.1 Flow structure

The pioneering study which addressed the rotating disk boundary-layer was performed by Theodore von Kármán (1921) who developed the problem and calculated the similarity solution velocity profiles in the boundary-layer. This meant introducing transformations to the equations of fluid motion which lead to reducing the governing partial differential equations to simpler ordinary differential equations. These transformations are only possible when considering 'self-similar' solutions, i.e. two velocity profiles at different radii only differ by a constant similarity factor. Advancing on von Kármán's work was Cochran (1934) a few years later, who noticed a few inaccuracies and errors in von Kármán's working. Cochran fixed these errors and went on to produce the first accurate numerical solution for the problem by numerically integrating the equations that von Kármán had laid out, thereby calculating the velocity distribution of the flow in the laminar region.

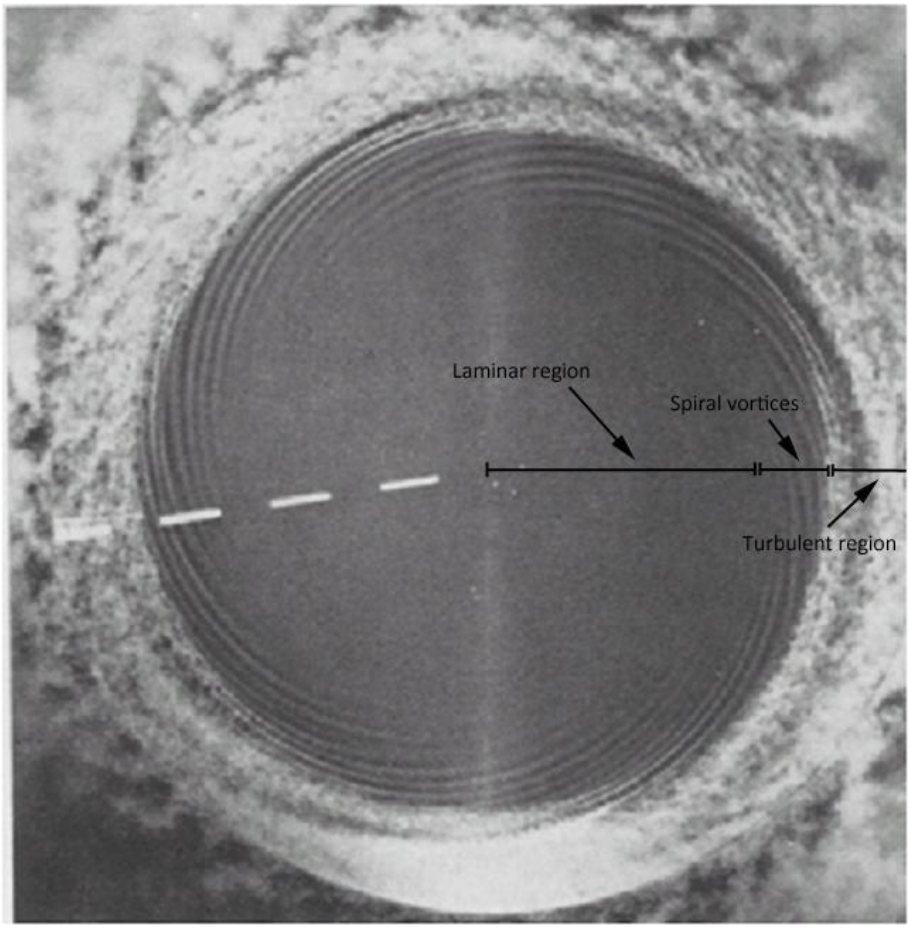

Figure 2.1 – Photo taken from Kobayashi et al. (1980), with annotations showing the three main regions of the disk; the laminar central region, the spiral vortices, and the turbulent outer region.

The structure of boundary-layer flow is relatively simple, compared to other three dimensional flow. Like most transitional flows, there are three main regions; laminar flow, transitional and fully turbulent (see Figure 2.1). The first velocity component across the whole disk is the azimuthal flow, as fluid at the disk surface is spun up by the moving wall to move circumferentially around the disk (Figure 2.2). However, the centrifugal forces on the fluid cause it to be thrown radially outwards as well, causing a cross-flow radial element perpendicular to the main direction of the flow. These two superimposed velocity components cause the resulting flow to move outwards in a spiral fashion. The third velocity component, the axial, physically acts to replace fluid lost at the edges of the disk by drawing fluid

downwards into the boundary-layer across the whole disk surface. In this way, the rotating disk flow acts like a centrifugal pump, drawing fluid down into the boundary-layer, and spinning it out from the centre of the disk outwards.

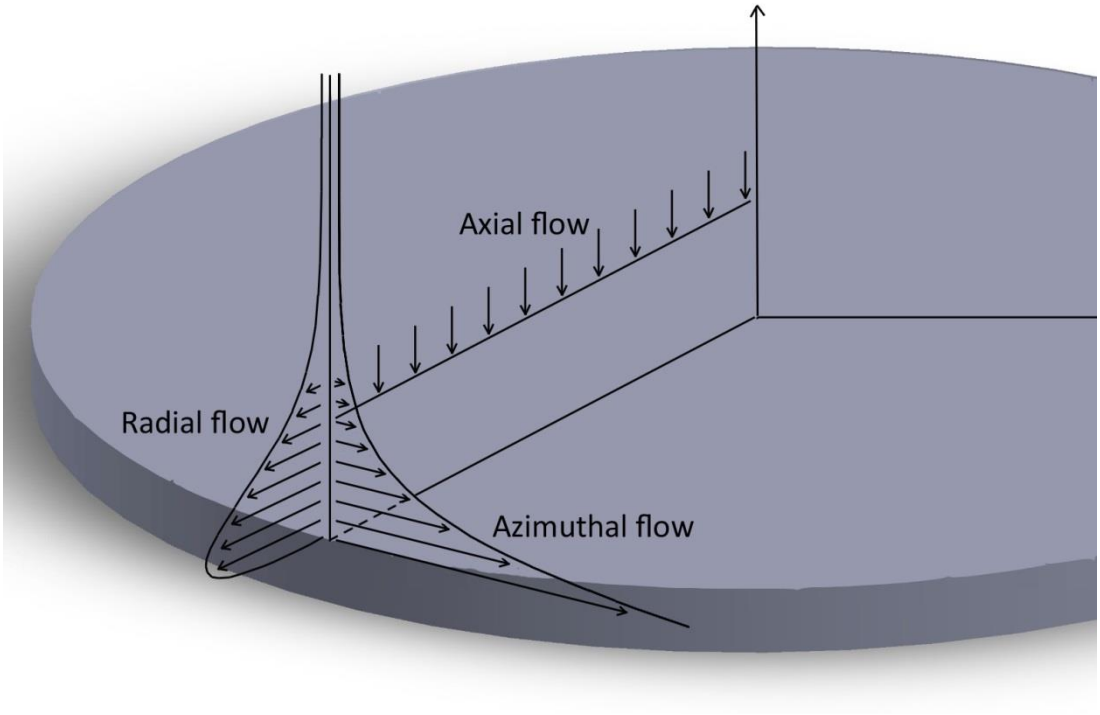

Figure 2.2 - An illustration of the three-dimensional flow on the surface of the rotating disk.

As the fluid travels through the central region of the disk, it remains laminar and steady. At some radius however, the flow will experience an instability which will develop into the distinctive, discrete spiral vortices that categorise the transitional middle region of the boundary-layer, seen clearly in Figure 2.1. The instability will be discussed later in this thesis. This unstable region eventually transitions into the final, turbulent region, which extends outwards to the edge of a finite disk, or indefinitely for an infinite disk.

The physical locations of these regions on the disk tend to occur at a relatively repeatable radius, compared with other transitional geometries, and for smooth,

polished disks with no protuberances can be predicted quite accurately. The radii of the regions physically move towards the centre of the disk when the rotation rate is increased, and drift further away when it decreases. This is due to the flow structure being linked, like all fluid flows, to the Reynolds number.

In most rotating disk studies, a parallel-flow approximation is applied. This approximation is used often in fluid mechanics problems as it provides simple linear equations to work with (Tollmien 1928; Schlichting 1933; Gaster 1974). In many other boundary-layer flows, the parallel flow approximation is used to account for variations of the Reynolds number in the streamwise direction due to an increasing boundary-layer thickness. However, for the disk, the thickness of the boundary-layer is constant. In the disk's case then, the reason for applying this approximation is to make the perturbation equations separable in terms of the radius length variable, r, the azimuthal angle, θ, and t. This is achieved by ignoring any changes of the Reynolds number with radius, and replacing any instances of the radius length variable r in the governing equations by Re, thus removing any dependence on r from them. The local Reynolds number in the case of the disk is determined by the dimensional velocity, $r^*\Omega^*$, the dimensional length scale, L^*, and the kinematic viscosity, ν^*.

$$Re = \frac{r^*\Omega^* L^*}{\nu^*} \tag{2.1}$$

The dimensional length scale can be expressed in terms of the kinematic viscosity and the rotational velocity.

$$L^* = \sqrt{\frac{\nu^*}{\Omega^*}} \tag{2.2}$$

Substitute this into the Reynolds number equation to get,

$$Re = \frac{r^*\Omega^*}{\nu^*}\sqrt{\frac{\nu^*}{\Omega^*}} = r^*\sqrt{\frac{\Omega^*}{\nu^*}} = \frac{r^*}{L^*} = r \tag{2.3}$$

Thus an increasing Reynolds number can be thought of in terms of simply moving outwards from the centre of the constantly rotating disk along the radius, or remaining at a constant radius on a disk that is speeding up.

The parallel flow approximation was shown to be valid by Cheng (1953) for boundary-layer flows provided the analysis is kept local, rather than applying globally to the whole surface. Thus the stability analysis used here will remain local in nature so as to invoke the parallel flow approximation, such as those used in studies by Malik (1981), Lingwood (1995a), Pier (2007), Garrett (2010) amongst others.

2.2 Stationary vortices

The vortices on the surface of the disk travel at different speeds in relation to the disk itself. There are many vortices which are travelling both more slowly and faster that the disk rotates, and thus these are known as travelling waves. The appearance of travelling waves on the boundary layer of the rotating disk have been well documented (Kohama 1987; Reed & Saric 1989; Jarre et al. 1996b; Corke & Knasiak 1998). These studies have found that travelling waves are more highly amplified than stationary waves, although in low disturbance environments such as the

rotating disk, stationary waves dominate and more likely to induce transition (Saric et al. 2003).

The waves which form the spiral vortices are travelling at the same speed and direction as the rotating disk, and so appear stationary with respect to the disk. This makes them easier to detect in experiments, and therefore this investigation will concentrate solely on stationary waves rather than travelling ones. This is mainly due to time constraints and the fact that the current experimental set-up only has one hot-film probe and so struggles to detect waves which change both spatially and temporally.

The spiral vortices that appear in the boundary-layer of a rotating disk are ever-present. Although they may not be observable without flow visualisation methods, the stationary vortices will always form, triggered by the initial conditions in the flow. This trigger is often known as the receptivity of the flow and for the rotating disk with no external disturbances or forcing, it is usually caused by minute roughness on the disk surface. Radeztsky et al. (1999) showed that flow over a swept airfoil, i.e. one with a cross-flow structure similar to a rotating disk, is very susceptible to instabilities caused by microns sized roughness. The investigation showed that stationary vortices could be enhanced via the use of small amplitude roughness elements in an otherwise clean background environment. Wilkinson and Malik (1985) revealed that the stationary vortices were most probably triggered by some small amplitude roughness or dust motes on the disk surface. Fedorov (1989) performed a linear perturbation analysis on the instabilities created via the cross-flow mechanism and found that in order to excite an instability with an initial

amplitude of 0.1% (assuming nonlinear breakdown occurs at 1%), the level of micro-roughness need only be 0.01 times the height of the displacement thickness. As Fedorov points out, these excitations are almost unavoidable and therefore will almost certainly be present on any rotating disk.

An early study by Smith (1946) done on the rotating disk boundary-layer in air, used hot wire probes to measure the wavenumber of the spiral vortices in the transition region, as well as the angle the vortices make with the radius. It was found that at a certain radius in the transition region, there were approximately 32 oscillations for every rotation of the disk, at an angle of 14°. The seminal study by Gregory et al. (1955) discovered that these values were a constant in the rotating disk system, as the angle was found to be 14° and 13°18’ from experimental and numerical observations respectively. They also discovered that the number of stationary spiral vortices in the central section was also a repeatable value, regardless of disk size, speed or fluid medium. Using a combination of china-clay visualisation and frequency data taken from acoustic microphones, they counted a total of between 28 and 31 stationary vortices on the disk surface. These values for the angle and number of vortices have since been confirmed by many studies since (Fedorov et al. 1976; Kobayashi et al. 1980; Kohama 1984; Wilkinson & Malik 1985) and have been taken as standard for the smooth disk flow.

2.3 Instabilities

The approach used to measure stability, for this as in many previous studies (Malik 1986; Lingwood 1995a; Garrett & Peake 2002), will be a linear stability analysis. The idea of a linear stability analysis is to superimpose infinitesimal perturbations on

top of the local mean flow, and see what these disturbances do as they flow downstream, or as time progresses. If they dissipate, then the flow is damped and stable at that point. However, if the perturbations grow, then the flow at that point is unstable.

There are two ways in which an unstable disturbance can affect the flow. Either the disturbance grows as it moves downstream; in which case it can only affect areas of the boundary layer downstream from the disturbance inception point, which is called a convective instability, or the disturbance remains fixed spatially, but grows temporally at this radial location to affect the flow around the inception point, including flow upstream. This is known as an absolute instability. The rotating disk boundary layer is known to include both types of instability, after Lingwood (1995a; 1996) proved the existence of the absolute instability in the boundary layer both theoretically and experimentally.

An unstable laminar flow is a precursor to transition to a turbulent flow. When performing a stability analysis, one can choose to explore the evolution of the perturbation as it develops in space downstream, which is known as a spatial analysis, or as it stays in place and grow over time, in which case it is known as a temporal analysis. In order to discover the existence and location of the absolute instability, Lingwood used a spatio-temporal analysis which is a combination of the two, as neither one of the former methods were sufficient for the rotating disk boundary layer.

In performing the stability analysis, the results obtained will show the Reynolds number at which the flow becomes unstable as well as the growth rates of these

disturbances. The points of instability can be plotted against a number of other variables such as azimuthal wavenumber or waveangle to generate neutral stability curves which help to visualise how stable a flow is overall. This visual overview helps to compare the potential stability of different flow situations. Note that a linear stability analysis cannot predict or explain any aspects of turbulence following transition, as this part of the flow necessarily contains nonlinear effects. In order to compare the numerical results with experimental data, an attempt will be made to keep our experimental boundary-layer in the linear regime by using only transitional roughness levels, for which a definition is given in Chapter 5.2.

There are generally accepted to be two main routes to instability in the rotating disk boundary-layer. The first is the cross-flow instability which arises from a point of inflection in the radial velocity profile, or when the second derivative of the radial component becomes equal to zero ($d^2U/dz^2 = 0$). Rayleigh (1879) proved therefore that an inflection point in a velocity profile was a necessary condition for an instability to occur, at least for parallel, inviscid flows. The cross-flow instability is therefore inviscid and is considered to be the dominant instability mechanism for the standard rotating disk flow in that it causes the spiral vortices which characterise the disk boundary-layer. The cross-flow instability was first discovered when Gray (1952) noticed that the transitional Reynolds number for a swept wing was lower than for an unswept wing. The swept wing contained the same stationary vortices caused by the cross-flow instability as on the disk, which triggered an early transition. The cross-flow instability has been numerically found to occur at a critical Reynolds number of 285-287 (Malik 1986; Mack 1985) and

experimentally to occur at anywhere from Re = 294-377 (Kobayashi et al. 1980; Malik et al. 1981).

The second known instability is the streamline-curvature instability. Through performing calculations with the Orr-Sommerfeld equations, which are essentially just stability analyses with Coriolis and streamline-curvature terms removed, many studies have found that this 'Type 2' instability does not appear. This is because the streamline-curvature instability is thought to be caused by a balance between viscous and Coriolis effects (Hall 1986), and therefore it makes sense that all signs of it disappear in stability results when the Coriolis and streamline-curvature terms are excluded (Lingwood 1995a) and at high Reynolds numbers (Lilly 1966). Itoh (1996) found that the strength of the streamline-curvature instability could be described using the parameter κ, which is defined as the ratio between the boundary-layer thickness and the radius of the curved streamlines. By varying the value of this parameter, it was shown that the critical Reynolds number of this instability increases to infinity as a curvature term decreased to zero, thus concluding that the instability was caused by the curved streamlines of the flow.

The streamline-curvature instability is rarely seen in experimental observations as, for stationary modes, it has a much lower growth rate than the stronger cross-flow disturbances, and tends to amplify travelling waves rather than stationary waves (Faller 1991). Since many experimental set-ups rely on detecting stationary waves, it seems natural that these lesser amplified streamline-curvature modes will fail to get picked up. When it is seen however, it seems to cause waves nearer the centre of the disk at an angle of -19° from the radial axis (i.e. angled in the opposite

direction to the spiral vortices) with a wavenumber of around 14-16 (Fedorov et al. 1976). These values have been confirmed numerically by Faller (1991) and Malik (1986) for the rotating disk, and by Tatro and Mollo-Christensen (1967) for the Ekman layer, which is similar to the rotating disk flow except the fluid is experiencing a solid body rotation almost equal to the velocity of the disk.

2.4 Transition

The point at which the spiral vortices break down into full turbulence is consistent and repeatable, in contrast to the more complicated pipe or flat plate transition points where transition into turbulence can vary enormously depending on many factors. Because of this repeatability, many experimentalists have been trying to pin-point its exact location. Many studies using visual methods such as china-clay or naphthalene, or data collection methods such as hot-wire or acoustical probes have narrowed the region of transition to a Reynolds number of between Re = 490 and 540 (A table of collated results can be found in Healey (2010)). It was discovered by Lingwood (1995a), that the repeatability of this location could well be due to an absolute instability occurring at Re = 510 (although this was later corrected to be 507.3) in numerical calculations and between Re = 504 and 514 found in experiments. Due to this absolute instability appearing within the region of measured transitional Reynolds numbers, Lingwood postulated that this leads to an unbounded linear response at these radii, which promotes transition around this Reynolds number.

Lingwood put the variation in transition Reynolds number (and in particular, ones much higher than her upper limit) down to discrepancies in judging transition

points, but Healey (2010) suggests another possibility; Healey noticed that due to the disks used in each experiment being of varying radii, they each had a different Reynolds number for their edge. He hypothesised that the edge Reynolds number could have an effect on the transition point, and that upstream effects from the edge could be stabilising the flow beyond what should be possible. He finds a correlation between the edge Reynolds number and the transition Reynolds number that could explain the transition numbers higher than expected from previous experiments. Imayama et al. (2013) performs a study specifically designed to test Healey's theory, and finds there to be only very weak correlation between the transition Reynolds number and the proximity to the edge of the disk. They hypothesise that the actual reason for large variations in transitional points are again down to differences in judging when transition has occurred.

2.5 Routes to turbulence

Once the boundary-layer has become unstable and the spiral vortices have formed, there remains the question of how the flow transitions into turbulence from there. There appear to be a few probable routes to turbulence that have been discovered for the rotating disk case. The first is the case in which there exists a very high amplitude travelling waves at low Reynolds numbers. Corke and Knasiak (1998) instigated high frequency travelling waves via the use of ink dots on the surface of a disk, and found that a pair of travelling waves formed together with a stationary wave in a resonant 'triad coupling', which lead to a high amplitude, low wavenumber stationary wave which dominated transition, leading to turbulence.

If no triad couplings are formed, stationary waves are formed as usual by the cross-flow instability and can lead to transition in two ways. Firstly, if they are of high amplitude they will form high frequency secondary instabilities which grow and cause rapid transition to turbulence. Balachandar (1992) performed a Floquet analysis for the 3D boundary-layer on a rotating disk and calculates the secondary instabilities by first working out the primary disturbance before adding it to the mean flow as a superposition and working out the secondary disturbance from this. He found that the critical amplitude for the primary disturbances was approximately 9%, above which the secondary instabilities would form and grow rapidly. These secondary disturbances took the form of counter-rotating vortices which occur at an angle from the primary spiral vortices, which had been seen a few years before by Kohama (1984) using smoke visualisations.

If the stationary waves have low disturbance levels and do not form secondary instabilities, then they may succumb to Lingwood's absolute instability at Re = 507. It is thought that perhaps beyond this Reynolds number no laminar flow can exist and thus provides an upper limit to the transition point. Lingwood (1995a) proved the existence of the absolute instability, a mode which grows in time at every spatial position, which will, given enough time, grow to cause non-linear behaviour which hastens the transition to turbulence. Because of this, the inviscid instability will occur regardless of external conditions, and so even disks in an incredibly clean environment will transition to turbulence at this point. However, it was then discovered numerically by Davies and Carpenter (2006), that despite the existence of an absolute instability on a local scale, globally the flow may still remain linearly

stable. Thus the role of the absolute instability on turbulent transition is still an uncertain one.

2.6 Roughness

Although theoretical studies often assume otherwise, surfaces in the real world cannot be completely smooth. In the field of fluid dynamics, small amounts of roughness on a micron-scale can have a large effect on the structure of a flow, and neglecting this roughness can result in some large discrepancies between theory and experiments. For this reason it is important to consider the flow over surfaces with roughness added, although due to the sheer variety of different types of roughness, this can often be very difficult. Roughness elements can differ in size, distribution and shape which all have different effects on the fluid and two experiments with seemingly similar roughness levels will display completely different flow characteristics.

Nikuradse (1933) carried out the seminal work on flow through rough pipes. He studied the pressure drop through pipes which had been roughened by adding sand grains to the walls of commercially bought smooth pipes. By measuring the diameter of the sand grains, he calculated a 'relative roughness' between this value and the diameter of the pipe. The majority of this work dealt with the pressure drop through pipes with a turbulent flow which is not relevant here, as the stability analysis is not valid for flows which become turbulent and nonlinear. However, he does note that for low Reynolds numbers, the resistance factor (and therefore pressure drop) is the same as for smooth pipes. This region is characterized by having the roughness projections lie completely within the laminar boundary-layer.

From this it can be ascertained that as long as the roughness elements remain within the boundary-layer, the pressure drop along the pipe should be equal to that of a pipe with smooth walls. Clearly pipe flow differs greatly from rotating disk flow, but an effort to keep the roughness protrusions within the boundary-layer for the disk will be made in an attempt to keep pressure gradients to a minimum.

Schlichting and Gersten (2004) use the regions present in the theory of the 'universal law of the wall' to describe three roughness regimes. For roughness below a certain level, they use the term *hydraulically smooth* to refer to a wall surface where the boundary-layer is not affected by the roughness. They also describe a regime where the roughness elements are so large they take up all of the wall boundary-layer, creating pressure forces which dominate the flow. They call this region *fully rough.* Finally, in between these two they define a regime known as the *transition region* which contains roughness elements large enough to affect the flow, but not so great that they create large pressure forces. From Nikuradse's findings above, in order to keep the protrusions within the boundary-layer the roughness used in this study will have to fall within the *transitional region* of roughness. Details on how this was achieved are found in Chapter 5.2.

Roughness can take many different forms. Floryan (1997) notes that there are three main classes of roughness shape. The first is the single two-dimensional roughness element, or trip wire, which itself can have a profile of many sizes or shapes. The second is a single three-dimensional roughness element such as a small raised block placed in the boundary-layer. These first two bear little similarity to 'roughness' as one would expect in the real world, but studies involving them benefit from a much

simplified flow and easily identifiable structures, and so are often used to mimic simple roughness. The third class is distributed roughness which covers the whole surface of the study, such as sandpaper or a corrugated surface.

Sandpaper is a common choice for creating rough surfaces (Leventhal & Reshotko 1981; Corke et al. 1986; Watanabe 1987), but aside from their average grain size, two sets of sandpaper will differ greatly in terms of height, pitch and distribution of sand grains. In addition to this, attempting to model a randomly rough surface such as sandpaper numerically becomes too difficult. For these reason, the roughness chosen for this study will be three-dimensional and distributed in nature, to try and match physical roughnesses found in real applications, yet will be simple enough to model numerically and produce experimental results which can be compared with others.

2.7 Boundary-layer control techniques

Boundary-layer control techniques have been of interest since it was found that delaying the point of transition on wings could decrease the effect of skin friction drag. In 1939, aircraft research engineers found that they could delay the transition point on a wing by applying suction across it through slots in its surface (see Braslow (1999) for a history of this type of control). A larger area of laminar flow over the wing surface meant less energy lost to skin friction drag in the areas where the flow was turbulent. Ways in which the flow could be kept laminar for as long as possible began to be developed and fell into two distinct groups. A short review of laminar flow control techniques is compiled by Saric et al. (2011).

Active flow control are methods which require an energy input to work, such as the suction method mentioned above and in later studies (Pfenninger 1946), or surface cooling (Wazzan et al. 1968). These flow control techniques work by forcing the second derivative of the velocity profile near the surface to be more negative (Reshotko 1984). The downsides to these in terms of use on aeroplanes are that they may possibly use as much energy to work as they would save through drag reductions. Similarly, they also require extra weight to be added to the aircraft which would negate the benefit of any fuel saved.

The second group of control methods are the passive type, by which no energy input is required to have the control effect. The method usually requires modifying the surface in some way such as adding a compliant layer (Carpenter et al. 2000) or the adding of leading edge 'tubercles' or scallops (Fish & Lauder 2006). Another popular technique is the modification of adding a rough surface.

2.8 Roughness as a control mechanism

The technique of using a rough surface to control the transition to turbulence has been widely considered in recent years. For example, airline component manufacturer Lufthansa Technik are experimenting with adding sharkskin-like riblets to the surface of the fuselage and wings of Lufthansa planes in an attempt to reduce drag and decrease fuel consumption by up to 1% (Lufthansa-Technik 2013). Understanding how such roughness works to delay the transition point is thus very important and there are many studies which work towards this understanding.

There are many ways in which a surface can be modified in order to simulate roughness. One way is look at singular points of roughness on an otherwise smooth

surface, and gauge how the flow reacts to this on a local scale. Many studies on the rotating disk in the past have usually dealt with these small roughness elements acting as a point source rather than a distributed roughness covering the whole disk surface (Jarre et al. 1996a; Wilkinson & Malik 1985; Mack 1985). The studies find that the spiral instabilities emanate from small point sources of roughness on the disk, whether they are naturally occurring or intentionally placed.

This method allows the authors to trip the flow and creates a localised, amplified instability in order to study it. In this case, the actual roughness used is not important; the same effect can be gained by introducing a puff of fluid into the boundary-layer instead (Lingwood 1996), although this latter study excites all frequencies rather than just stationary ones. However, the roughness element in the above cases is simply used as a controlled, repeatable path to a pure transition. Essentially, this is not full roughness, and so any effects to the boundary-layer will not be indicative of how the flow will react to a fully rough disk, which is the aim of this thesis.

Another way is to use a distributed random roughness, such as the sandpaper used experimentally by Watanabe (1987; 1993) which is more useful in creating a 'global' roughness to see how it affects the whole boundary-layer. However, random roughnesses are more difficult to simulate in a stability analysis. Authors have tried using a simulated suction (Floryan 1997) albeit for Poiseuille, Couette and Blasius flow, to model roughness and found that the suction induced a new type of instability which is dominant at low Reynolds numbers. A different author added a partial slip condition to the surface of the disk to mimic roughness and saw a

thickening of the boundary-layer and reduction in the flow velocities because of this (Miklavcic & Wang 2004).

Zoueshtiagh (2003) measured the transitional Reynolds number for the flow over a rough rotating disk submerged in water. Roughness levels of 170µm, 335µm and 1325µm were achieved by attaching quartz granules of differing diameters to the surface of smooth glass disks. It was found that there was no noticeable effect on the transition location until a threshold level of roughness was reached, upon which point, the critical Reynolds number fell sharply. However, at some of the higher rotation rates, the method of determining the transition point (via flow visualisation) was up to 20% in error. Therefore, there could have been effects unseen for the lower levels of roughness.

To make the process of modelling and quantifying roughness easier, many studies use riblets, or patterns of roughness in a variety of shapes. Configurations such as V-shapes (Wang et al. 2000), rectangles (Elsamni et al. 2007), triangular grooves (Baron & Quadrio 1993) have all been tried with varying degrees of success.

Longitudinal riblets have been shown to modify the flow profiles (something which could affect the instability mechanisms) and reduce drag by up to 10% by breaking up the coherence of the turbulent streaks or rolls (Sirovich & Karlsson 1997). This act of disrupting the coherence is thought to occur in two ways. The presence of rough elements on the surface helps to destroy any turbulent structures that form, while a cross-flow variation in the flow that is caused by the rough surface helps to stabilise the flow and prevent the turbulent structures reforming (Choi 2006).

One study by Fransson et al. (2006) found they could delay transition on a flat plate in a wind tunnel by using cylindrical roughness elements to induce a streaky base flow. This helps to reduce the exponential growth of Tollmien-Schlichting waves and shift the transition location downstream. Similarly, transition delays have been seen for swept wing boundary-layer flow. Radeztsky (1999) used random, natural-surface roughness to delay transition from 48% to 77% chord on a swept wing, while Reibert (1996) and Saric (1998) both used periodic roughness arrays to achieve similar results. More recently, Hosseini et al. (2013) performed direct numerical simulations in order to confirm the study by Saric, albeit with a more complex disturbance field, and produced results in agreement with Saric. They found that the leading edge cylindrical roughness elements delayed transition from 45% to 60% chord by damping the most unstable cross-flow mode as well as the secondary instabilities.

An attempt to mimic the three-dimensional form of shark scales and its role in reducing drag found that 3D riblets did reduce the drag by 6.85%, but this was less than the 9% achieved for the 2D case (Bechert et al. 2000). Manufacturing these complicated 3D riblets however, turned out to be a formidable undertaking, and so easier ways of creating roughness patterns are often sought.

Most studies build up 3D elements on the surface of a disk or flat plate to create roughness, but another method is to create a roughness pattern by instead cutting grooves into the material. Spiral grooves cut into an aluminium disk by a wet etching process helped to reduce drag by up to 15% by controlling the secondary

flow of the boundary-layer (Watanabe et al. 2007). They also found that the spiral grooves suppressed the generation of local vortices, and modified the boundary-layer velocity profiles by decreasing the flow velocities in both the azimuthal and radial directions.

Studies into the number of stationary vortices over rotating disks have always looked at smooth surfaces, or disks with isolated roughness elements. However, it has been noted that when the surface of the disk is not completely smooth, there is a noticeable effect on the number of vortices. Watanabe (1987) noticed that when there was a distributed roughness of 15µm applied to the disk, the number of stationary vortices decreased to 25, compared to 32 for the smooth case. In a later study on a rotating cone (for which the boundary-layer is qualitatively similar to the disk), Watanabe et al. (1993) added roughness of between 4.3µm and 18.7µm and noticed a decrease in the number of vortices seen as the roughness is increased. They postulated that the reason for this decrease was due to the roughness changing the mean velocity profile. Both of the above cases used sandpaper or emery cloth to create the rough surfaces, and as such they could only vary the grain size. The approach taken in this study is to use a more comprehensive range of roughnesses by varying both the roughness height and width.

3 Numerical formulation

To formulate the stability equations for the rough, rotating disk, the approach taken by Lingwood (1995a) and Garrett (2002) is adopted, incorporating a method set by Yoon et al. (2007) to control the surface roughness. The first step will be to add the rough surface to the disk geometry by replacing the standard flat radial axis with that described by a simple function which changes only with the radial coordinate. With this new geometry, the next step will be to calculate the governing equations which describe the mean flow components over this new disk and solve them to obtain the three-dimensional velocity profiles for disks with distributed roughness. Yoon et al. (2007) calculated mean flow profiles for their new disk surface geometry, but only looked at one roughness level at changing Rossby numbers. A similar method is used here to look at how the mean flow profiles change over a range of surface roughnesses. These mean flow profiles will then be used as a basis to conduct the linear stability analysis, in which the behaviour of small perturbations added to the mean flow are studied as they evolve downstream. This will be done using the framework and stability code developed by Lingwood mentioned previously, through which the perturbation equations are formed and then solved to determine the stability of the disk boundary-layer using these new flow profiles.

This method is justified by Lessen and Gangwani (1976) who state that according to investigations carried out by Tollmien (1928) and Schlichting (1933), the wall roughness should affect the boundary-layer stability primarily through the modification of the mean flow profiles, and that the stability is often very sensitive

to small changes in the mean profile. Hence performing stability calculations on the distorted theoretical flow is likely a valid technique to use.

3.1 Steady flow profiles

The geometry used is similar to many previous rotating disk studies; an infinite disk rotating in an incompressible, Newtonian fluid is presented, and described using a cylindrical coordinate system. The radial coordinate is taken to be r^* and the azimuthal coordinate to be θ. The disk rotates at a constant angular velocity Ω^* around the axial direction z^* (see Figure 3.1 for a diagram of the system). For this problem, a fixed frame of reference in which the rotating disk rotates is used, in contrast to other studies where the frame of reference rotates with the disk itself. Because of this approach, no Coriolis terms will appear in the governing equations, which simplify them somewhat. The steady flow components in these directions are u^*, v^* and w^*. The fluid itself has a pressure p^*, density ρ^* and kinematic viscosity ν^*. All dimensional quantities are indicated by asterisks. These dimensional quantities are scaled by a characteristic length-scale given by the boundary-layer thickness, $\lambda^* = \sqrt{\nu^*/\Omega^*}$ a velocity scale given by $\lambda^*\Omega^*$ and a pressure scale given by $\rho^*\lambda^{*2}\Omega^{*2}$.

As in many previous disk studies, the Reynolds number will be based on the disk rotation velocity $r^*\Omega^*$, kinematic viscosity of the water ν^* and dimensional length scale λ^*. Equation 2.3 therefore tells us, that for the rotating disk, the Reynolds number equates to the radial distance.

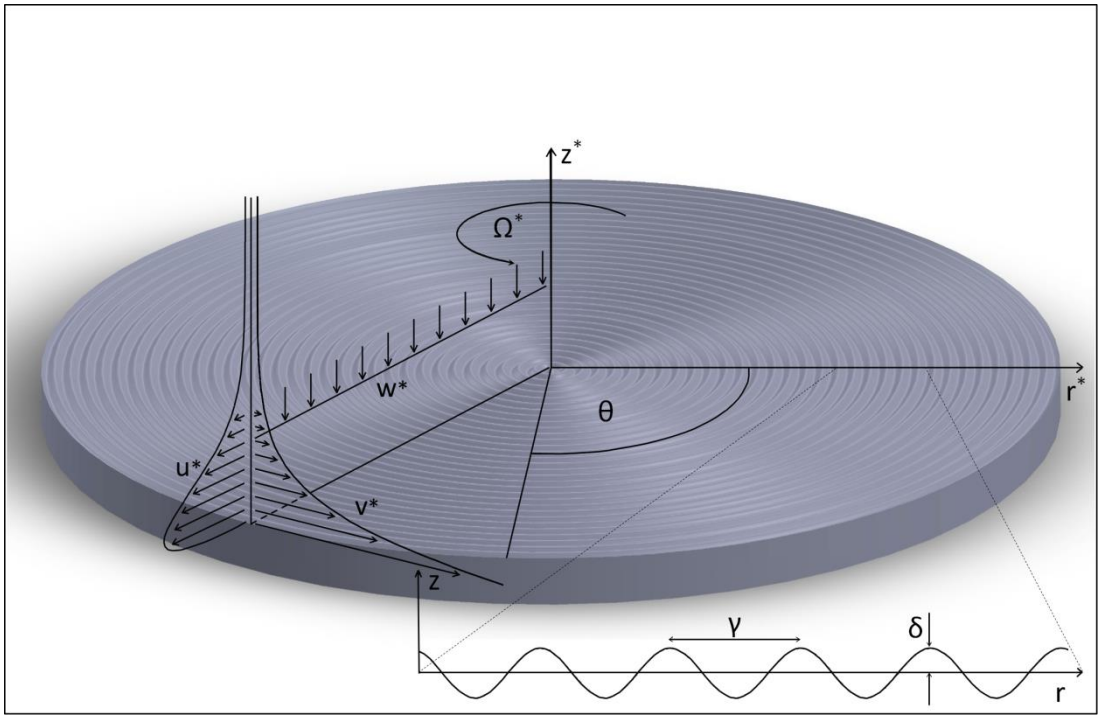

Figure 3.1 – Sketch of the disk surface, coordinate system and flow profiles.

In order to add a distributed roughness to the disk, the approach of Yoon et al. is to describe the surface of the disk as a function such as $s^* = a^* \cos(2\pi r^*/\gamma^*)$ where a^* is the amplitude and γ^* is the wavelength of the surface variation resulting in a 'wavy' surface such as in Figure 3.1. This function can of course be non-dimensionalised using the above scales to get

$$s = \delta cos\left(\frac{2\pi r}{\gamma}\right) \tag{3.1}$$

with δ and γ being the non-dimensional amplitude and wavelength parameters respectively. These are the control parameters which allow the amount of roughness on the surface of the disk to be varied, and it is useful to refer to them in terms of the ratio between the two, i.e. the roughness ratio δ/γ.

Before a system of governing equations with this new geometry can be developed, the wavy surface just created needs to be removed using the Prandtl transposition

theorem (Prandtl 1938) which is a method to transform a complex geometry onto a simpler one, without having to change the boundary conditions. This is done by switching to a new coordinate system (r, θ, ζ) where $\zeta = z - s(r)$ and similarly transforming all velocity components

$$U = u, \quad V = v, \quad W = -s'u + w \tag{3.2}$$

with the prime representing differentiation with respect to r. For the current study, we are only interested in situations where the disk is rotating rapidly enough to form a thin boundary-layer. In other words it is required that $Re^{-1} \ll 1$. Thus this boundary-layer assumption can be enforced by setting

$$\widetilde{W} = Re^{1/2} W. \tag{3.3}$$

Finally, variables closely related to von Kármán similarity variables to describe the velocity components are introduced

$$f(r, \zeta) = \frac{U}{r}, \quad g(r, \zeta) = \frac{V}{r}, \quad h(r, \zeta) = \widetilde{W} \tag{3.4}$$

In order to form the new governing equations, we first take the non-dimensionalised, cylindrical Navier Stokes equations and apply the transformations from Equation 3.2 and the boundary-layer assumptions before substituting in the variables from Equation 3.4. The result is the set of partial differential equations

$$2f + r\frac{\partial f}{\partial r} + \frac{\partial h}{\partial \zeta} = 0, \tag{3.5}$$

$$rf\frac{\partial f}{\partial r} + h\frac{\partial f}{\partial \zeta} + f^2\left(1 + r\frac{s's''}{1 + s'^2}\right) = \left(1 + s'^2\right)\frac{\partial^2 f}{\partial \zeta^2} + \frac{g^2}{1 + s'^2}, \tag{3.6}$$

$$rf\frac{\partial g}{\partial r} + h\frac{\partial g}{\partial \zeta} + fg = \left(1 + s'^2\right)\frac{\partial^2 g}{\partial \zeta^2} - fg, \tag{3.7}$$

subject to the boundary conditions

$$\begin{aligned} f(r) = h(r) = 0, \quad g(r) = 1 \quad &\text{at} \quad \zeta = 0, \\ f(r) = g(r) = 0 \quad &\text{as} \quad \zeta \to \infty \end{aligned} \tag{3.8}$$

where the flow at the disk surface is subject to no-slip conditions and there is quiescent fluid far from the disk. In creating Equations 3.5-3.7, we have invoked the assumption that there is no pressure gradient in the radial direction, or $\partial p/\partial r = 0$. This is considered valid as long as the roughness ratio remains small, according to Le Palec et al. (1990). The justification is that if the surface roughness ratio is small, there is less variation from peaks to trough of the sine function that could result in a difference of pressure in between. The equations reduce to the familiar von Kármán equations as the roughness function on the disk becomes flat i.e. as $s(r) \to 0$.

These partial differential equations can be solved easily using the commercial NAG routine D03PEF. The routine reduces the PDEs to a system of ordinary differential equations in ζ using the method of lines. This routine has been used successfully on a number of occasions by Garrett and co-workers (Garrett & Peake 2002; Garrett et al. 2010; Samad & Garrett 2010; Barrow & Garrett 2013).

Spatial discretization of the PDEs is done using the Keller box method (Vajravelu & Prasad 2013), which is an implicit scheme with accuracy of the second order. This method replaces the second order derivatives with first order derivatives by introducing additional replacement variables, before writing the difference

equations using the central difference method. The points for this method are taken to be at the four corners of a box, hence the name. The equations are then linearized, removing higher order terms, before being solved by a backwards difference method.

The equations are solved at an initial radius $r = 0$ using the backwards difference method for 100 points between the surface of the disk $\zeta = 0$ and a height of $\zeta = 20$. This solution is then used to solve the next iteration at the next radius as the routine moves outwards.

The initial solution at r_{init} is found by using the series solution method used by Banks (1965). The method replaces the velocity components in the PDEs (f, g, h) with series expansions in terms of r and because r_{init} is small we can reject higher order terms and simply look at leading order $O(r^0)$ terms. As it turns out, using the series expansion method results in the initial solution at $r = 0$ being the original von Kármán disk profile for all s, and so the initial input for the system at $r = 0$ is simply the smooth von Kármán profiles.

Due to the cyclical nature of the sinusoidal surface, the solved profiles that are produced are slightly different depending on their location i.e. they vary slightly over one period of the wavelength γ. To remedy this, and produce a single profile with no dependence on radial location, an ensemble average of the profile is taken from 100 single profiles over one period of the sine wave. This ensemble averaging makes physical sense since the scale used for the roughness length is very small in relation to the larger scale at which the similarity dominates. In reality, there would be no discernible variation of the viscous fluid over the smaller length scale. The

effectiveness of this averaging and the whole mean flow method will be tested by experimental verification in Chapter 6.1.

3.1.1 Code validation

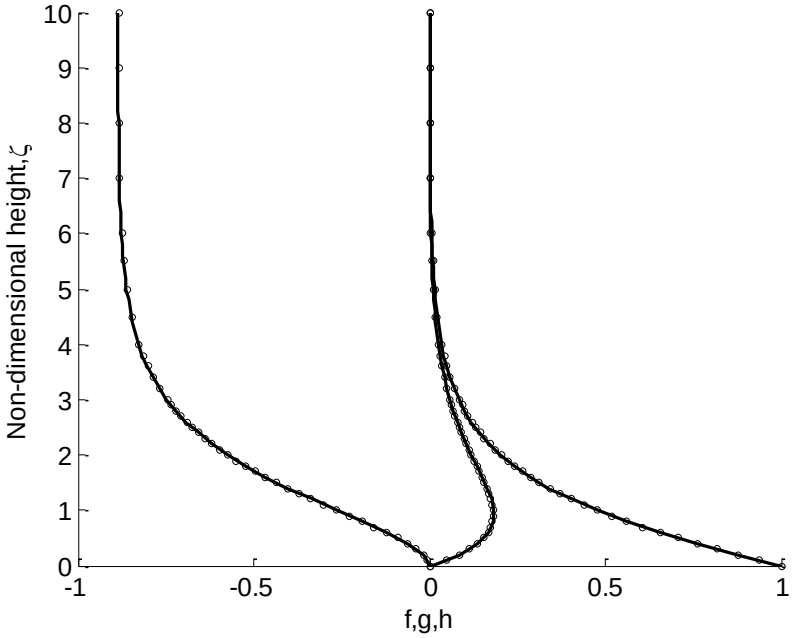

Figure 3.2 - Velocity profiles for the f, g and h components. (-) shows 'smooth' results from the D03PEF routine with δ = 0, γ = 1. (o) shows results taken from (Owen & Rogers 1989).

In order to validate the results generated by the NAG routines, the velocity profiles for the smooth case where $\delta = 0$ and $\gamma = 1$ can be compared to previously generated profiles. As can be seen in Figure 3.2, the velocity profiles for all three coordinates (solid lines) are compared against profiles taken from Owen and Rogers (1989) (circles) for $\delta = 0$ and $\gamma = 1$. For all three velocity components, the smooth flows are similar.

3.1.2 Results

Figures 3.3-3.5 show the three velocity components for disks with varying roughness. The results are taken at an arbitrary radius of $r = 4$ and averaged over one wavelength, since the solution is independent of radial location. There is a

noticeable effect as the roughness is increased from a smooth disk $\delta/\gamma = 0$ through to $\delta/\gamma = 0.2$. For the radial component, the effect is to decrease the velocity of the wall jet and increase the overall thickness of the boundary-layer. A similar effect was seen experimentally on a flat plate boundary-layer by Leventhal and Reshotko (1981) where sandpaper roughness caused a thickening of the Blasius (flat plate) boundary-layer, and also by Baron and Quadrio (1993) who saw a thickening of the viscous sublayer in turbulent flow over triangular riblets. The decrease in velocity makes physical sense since the friction of the roughness would act to hold back the base of the wall jet. Lessen and Gangwani (1976) plotted the disturbed velocity profiles of the flow over a flat plate with a wavy surface and found there to be a mean backflow for the streamwise profile caused by the zero flow effect at the crests and valleys of the wall. It could be that a similar result causes a reduction in the wall jet by adding a small backflow element to the forward facing jet.

For the radial profiles, the inflectional point on the radial profile is shifted upwards as can be seen more clearly in Figure 3.6. This figure simply plots the first derivative of the radial profile ($df/d\zeta$) for each roughness, so that the height of the inflection point is more visible.

This could be significant to the stability of the flow since the point of inflection in the mean flow profile is considered to be the direct cause of the cross-flow instability, and any changes in its location could affect the behaviour of the instability in turn. Although not shown in Figure 3.6, the upward trend of the inflection point continues up to roughness ratios of $\delta/\gamma = 0.375$. Thereafter the

inflection point begins to fall again. However, it is thought that this result is due to limitations in the code rather than an indication of how the flow might behave. According to Le Palec (1990), the assumption of an unchanging pressure difference across the sinusoidal profile can only be justified for mild roughness, i.e. small δ/γ. For this study therefore it was decided to keep $\delta/\gamma = 0.375$ as an upper limit on the amount of roughness.

In the study by Lessen and Gangwani (1976), an inflection point was induced in the mean flow profile of the flat plate with the addition of the wavy surface. There was no comparison between increasing levels of roughness and position of the inflection point in their paper however, so it is not known if this effect is related to the upward trend seen in Figure 3.6 or if it is simply a consequence of the slower wall jet and thickened boundary-layer.

The azimuthal component also sees a thickening of the boundary-layer, but sees an overall increase in the velocity at every point in the boundary-layer. The axial component meanwhile, has a thickening, as well as an increase in fluid being entrained into the boundary-layer, to make up the extra fluid passing through the other directions. Any change on the axial component will have less effect on the stability of the flow however as the boundary-layer assumptions made in equation 3.3 ensure that the axial flow is an order of magnitude smaller than the other components. Comparisons between these profiles and experimental observations are made in Chapter 6.1.

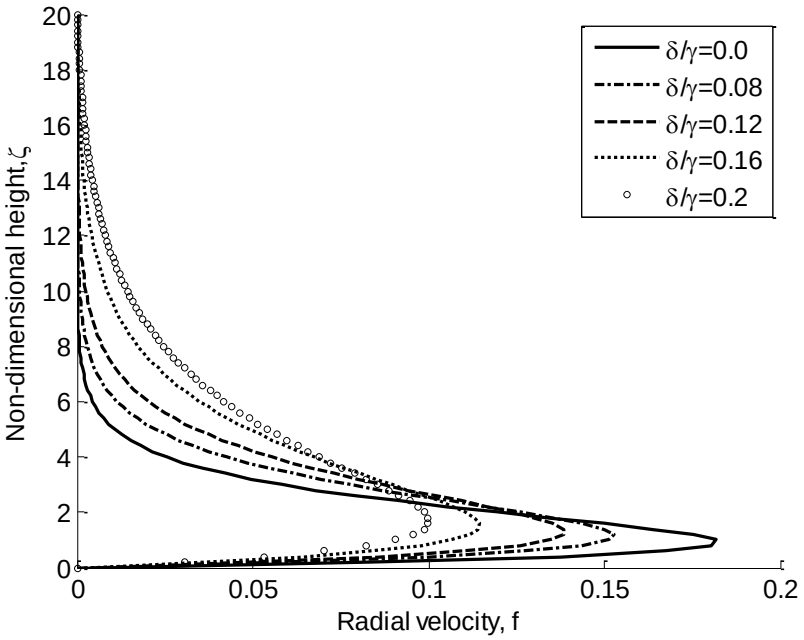

Figure 3.3 - Radial velocity profile for increasing roughness ratio.

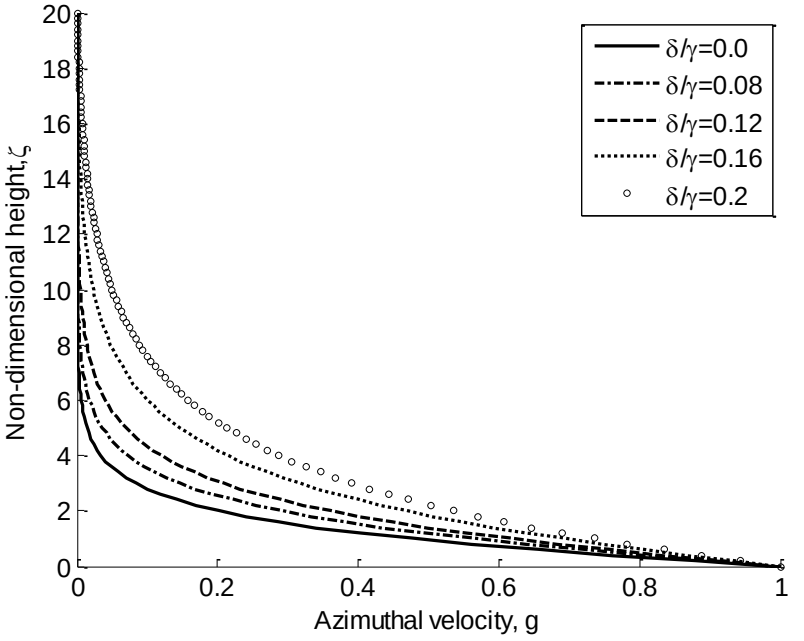

Figure 3.4 - Azimuthal velocity profile for increasing roughness ratio.

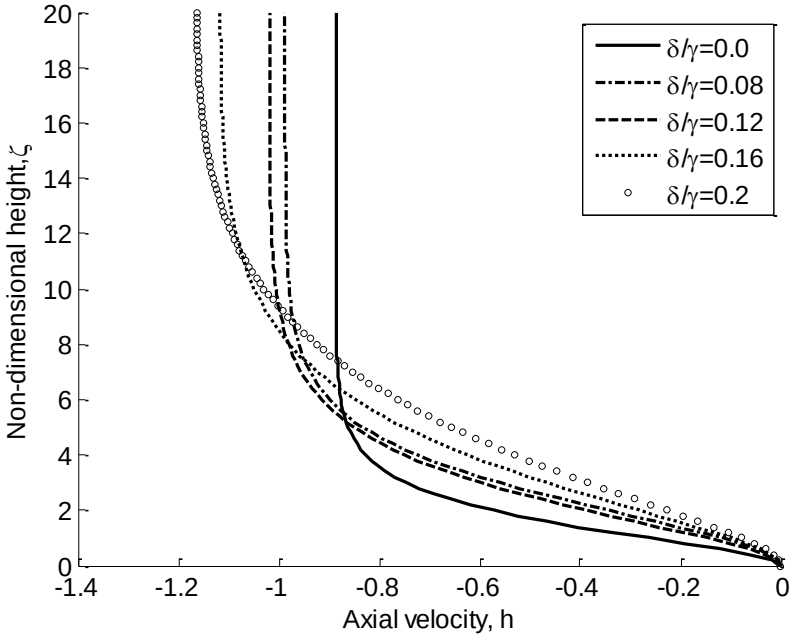

Figure 3.5 - Axial velocity profiles for increasing roughness ratio.

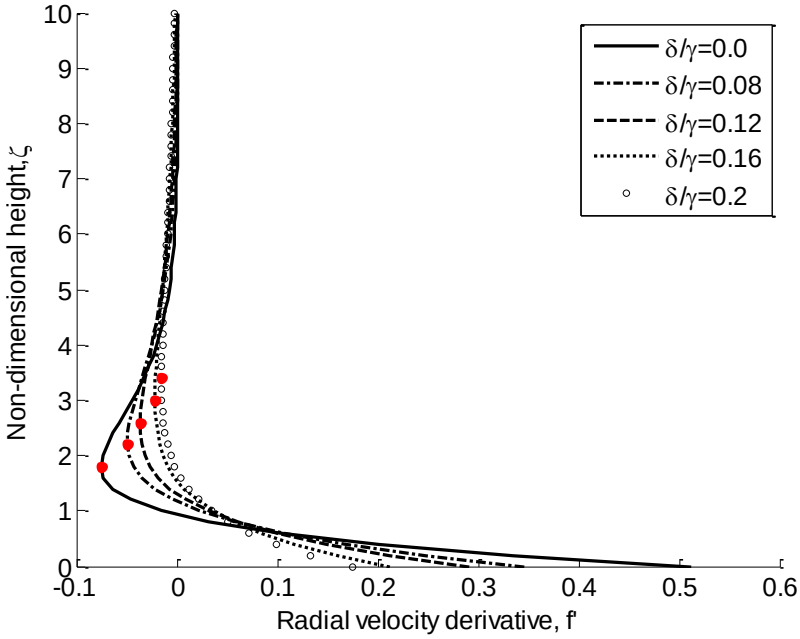

Figure 3.6 - Derivative of the radial profile showing the points of inflection.

3.2 Deriving the perturbation equations

Once the steady state velocity profiles for the sinusoidal rough surface are found, they can be used to predict the stability of the flow for the range of values of δ and γ. The method in this section follows closely the method used by Lingwood (1995b) and Garrett (2002). First, the perturbation equations which will be used to track the flow's stability must be derived. Infinitesimally small perturbing quantities are added to the averaged steady flow profiles which are then substituted into the boundary-layer equations. We will use upper-case barred symbols for the perturbed flow components, and lower-case hatted symbols for the perturbing quantities for clarity. The steady state components are as before.

$$(\overline{U}, \overline{V}, \overline{W}, \overline{P}) = (U + \hat{u}, V + \hat{v}, W + \hat{w}, P + \hat{p}) \tag{3.9}$$

The perturbations take the normal mode form

$$(\hat{u}, \hat{v}, \hat{w}, \hat{p}) = (u, v, w, p)e^{i(\alpha r + \beta\theta + \omega t)} \tag{3.10}$$

In this form, α is the wavenumber in the radial direction, and β the wavenumber in the azimuthal direction, while ω is the frequency of the perturbation. As mentioned in Chapter 2.3, the stability analysis can be temporal and therefore have a complex frequency, or spatial and have complex wavenumbers instead. Because it more closely corresponds to physical situations, we're interested in how the waves grow spatially, and therefore both α and β will be complex, with the real part describing the wavenumber, and the imaginary part describing the growth rate of the wave in each direction. Due to the azimuthal periodicity of the disc, there can be no growth of the waves in the azimuthal direction and hence, we can set $\beta_i = 0$.

Due to the transformation carried out in Equation 3.2, the computed velocity components do not currently compare to the physical domain. The radial and azimuthal components have not changed but the axial flow component is affected by the wavy floor and so a transformation such as the following may be necessary

$$W = s'U + \widetilde{W}. \tag{3.11}$$

However, looking at Equation 3.11 it is obvious that averaged over the length of one wavelength $s'U$ reduces to zero, and thus W and $\widetilde{W}$ are approximately the same. Therefore as long as any future surface function remains oscillatory, any dependency on radial location can be averaged out.

Replacing the velocity components in the cylindrical, dimensionless, steady Navier Stokes equations with Equations 3.9 and 3.10 and then simplifying gives us the following equations:

$$-i\omega u + iU\alpha u + iV u\bar{\beta} + \frac{Wu'}{Re} + wU' + \frac{Uu}{Re} - \frac{2Vv}{Re} = -ip\alpha \pm \frac{u\alpha^2}{Re} - \frac{\bar{\beta}^2 u}{Re} + \frac{u''}{Re} \tag{3.12}$$

$$-i\omega v + iU\alpha v + \frac{Vu}{Re} + i\bar{\beta}Vv + \frac{Wv'}{Re} + wV' + \frac{Uv}{Re} + \frac{Vu}{Re} + \frac{Vw}{Re} = -i\bar{\beta}p - \frac{v\alpha^2}{Re} - \frac{v\bar{\beta}^2}{Re} + \frac{v''}{Re} \tag{3.13}$$

$$-i\omega w + iU\alpha w + iVw\bar{\beta} + \frac{Ww'}{Re} + \frac{wW'}{Re} - \frac{2Vv}{Re} = -p' \pm \frac{w\alpha^2}{Re} - \frac{w\bar{\beta}^2}{Re} + \frac{w''}{Re} \tag{3.14}$$

$$iu\alpha + \frac{u}{Re} + \frac{w}{Re} + i\bar{\beta}v + w' = 0 \tag{3.15}$$

In the above, the mean flows have been subtracted and the equations have been linearized to remove terms of higher order, since the perturbations are already very small and so any terms of higher order would be negligible. Re is locally constant and as such does not change with r, hence we have replaced all instances of radial distance r with Re, while $\bar{\beta} = \beta/Re$. The prime in Equations 3.12-3.15 indicates differentiation with respect to the axial coordinate ζ.

We can write the perturbation Equations 3.12-3.15 in a different way by using a set of transformed variables taken from Lingwood (1995a).

$$\phi_1 = \left(\alpha - \frac{i}{Re}\right)u + \bar{\beta}v \tag{3.16}$$

$$\phi_2 = \left(\alpha - \frac{i}{Re}\right)u' + \bar{\beta}v' \tag{3.17}$$

$$\phi_3 = w \tag{3.18}$$

$$\phi_4 = p \tag{3.19}$$

$$\phi_5 = \left(\alpha - \frac{i}{Re}\right)v - \bar{\beta}u \tag{3.20}$$

$$\phi_6 = \left(\alpha - \frac{i}{Re}\right)v' - \bar{\beta}u' \tag{3.21}$$

This allows us to express the perturbations as the following six ordinary differential equations:

$$\phi_1' = \phi_2 \tag{3.22}$$

$$\phi_2' = \phi_3 Re\left(\left(\alpha - \frac{i}{R}\right)U' + \bar{\beta}V'\right) i\phi_4 + \left(\alpha^2 + \bar{\beta}^2 - \frac{i\alpha}{Re}\right)Re + W\phi_2 - 2V\phi_5 + \left(\left(\alpha^2 + \bar{\beta}^2\right) + iRe\left(\alpha U + \bar{\beta}V - \omega\right) + U\right)\phi_1 \tag{3.23}$$

$$\phi_3' = -i\phi_1 - \left[\frac{\phi_3}{Re}\right] \tag{3.24}$$

$$\phi_4{}' = -\frac{\phi_3}{Re}\left(\left[\alpha^2 + \bar{\beta}^2\right] + iRe\left(\alpha U + \bar{\beta}V - \omega\right) + W'\right) + \left[\frac{iW\phi_1}{Re}\right] - \left[\frac{i\phi_2}{Re}\right] \tag{3.25}$$

$$\phi_5' = \phi_6 \tag{3.26}$$

$$\phi_6' = 2V\phi_1 + \left[\left(\bar{\alpha} - \frac{i}{R}\right)V' - \bar{\beta}U'\right]Re\phi_3 + \left[\left(\bar{\alpha}^2 + \bar{\beta}^2\right) + iR\left(\bar{\alpha}U + \bar{\beta}V - \gamma\right) + U\right]\phi_5 + \bar{\beta}\phi_4 + W\phi_6 \tag{3.27}$$

It is noted that these equations are identical to those derived by Lingwood. The result of this formulation is that the addition of roughness only changes the form of the steady flow and not the perturbation equations.

3.3 Solving the perturbation equations

In order to solve the eigenvalue problem posed by Equations 3.22-3.27, we set out the boundary conditions as follows, which are now in a rotating frame of reference

$$\begin{aligned} \phi_i &= 0 \quad \text{at} \quad z = 0 \\ \phi_i &= 0 \quad \text{as} \quad z \to \infty \end{aligned} \tag{3.28}$$

where $i = 1,2 \ldots 6$. This ensures that the disturbances die out after leaving the boundary-layer. The problem needs to be solved for certain combinations of values of α, β and ω for inputs of the parameters Re, δ and γ. Hence we form the dispersion relation:

$$D(\alpha, \beta, \omega; Re, \delta, \gamma) = 0 \tag{3.29}$$

The spatial branches are calculated using the same process used by Lingwood (1995a) and Garrett (2002) using code provided by Lingwood. The eigenvalue problem is solved using a double precision, fixed-step-size, fourth order Runge-

Kutta integrator with Gram-Schmidt orthonormalization and a Newton-Raphson linear search procedure.

For user determined values of the Reynolds number and roughness levels and for a starting value of β_r the code increments through increasing values of β_r and calculates α_r and α_i at each point. As mentioned previously, since we are only interested in the growth of the perturbations downstream in the radial direction, we can set $\beta_i = 0$. This disallows any growth in the azimuthal direction and provides an axisymmetric amplitude distribution.

Since we are assuming that the spiral vortices we are looking for are stationary, we can set the frequency of the vortices to be equal to the frequency of the disk speed, i.e. they are stationary with respect to the disk and therefore we ensure $\omega_r = \beta$.

Thus we get the convective instability spatial branch in the α-plane for a certain Reynolds number and roughness ratio. We use this branch to tell us whether the flow is unstable or not at that point by looking at the radial wave growth rate α_i. If $\alpha_i > 0$ then the perturbation will be damped and fade away, but if $\alpha_i < 0$ then the disturbance will grow and an instability will form at that Reynolds number or radius. The points at which the branch becomes unstable (drops beneath the α_r axis in the complex α-plane) can then be found.

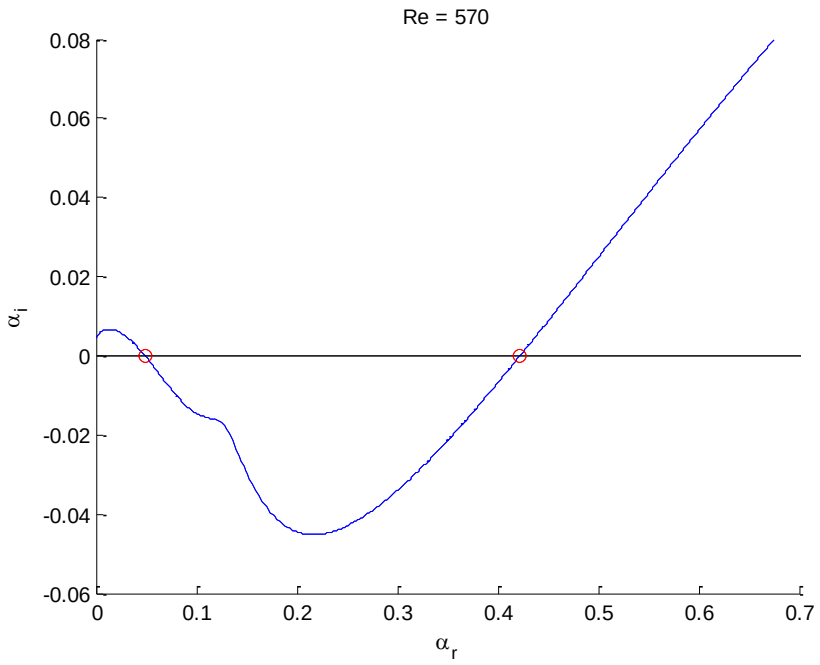

Figure 3.7 - Example of a spatial branch taken at Re = 570 for a roughness ratio of $\delta/\gamma = 0.167$. Circles indicate points of neutral stability.

Figure 3.7 shows an example branch developing in the α-plane for a certain Reynolds number. The code tracks the branch as it develops with increasing values of β_r from left to right. Initially at low α_r the flow is stable and all perturbations will be damped. Then as the branch drops below the x-axis, the perturbations become unstable and excited. The growth rate of these disturbances is linked to the distance they fall below the x-axis. In other words, the more negative α_i becomes, the higher the growth rate of the excited perturbation. The points at which the branch crosses the x-axis are important as these display the limits of the unstable region; the neutral stability points.

Whilst keeping the roughness variables the same, the Reynolds number can be incremented and the eigenvalue problem solved again to find the zero-growth neutral stability points at successive radii. In this way a neutral stability curve can

be built up in the manner of many preceding studies (Brown 1961; Lingwood 1995a).

4 Numerical results

4.1 Neutral curves

Neutral curves are produced for a range of different roughness ratios for a disk with a sinusoidal roughness pattern, and the comparisons between them are presented here. As is standard for neutral curve plots, the Reynolds number of the flow is plotted against different variables, namely α_r, β_r and the angle of disturbance ε in order to see the range of stability that the flow should have.

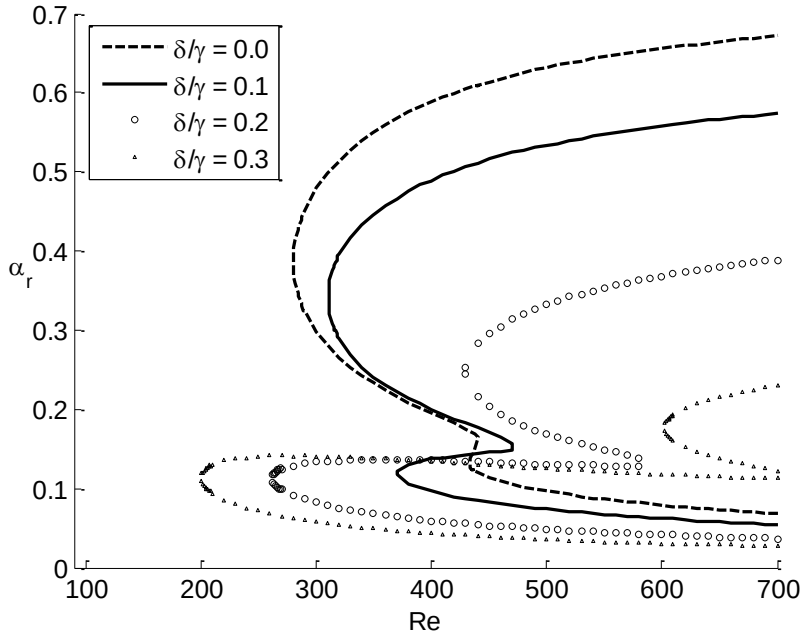

Figure 4.1 - Neutral curve plot against α_r with increasing roughness ratio.

Figure 4.1 shows the stability curve for the rough rotating disk with increasing levels of roughness ratio. The ratio $\delta/\gamma = 0$ represents a smooth disk surface, and comparisons between the shape of this curve and curves from other studies are positive. It is known that 'upper' lobe of this curve is caused by the Type 1, or cross-flow instability in the boundary-layer flow, while the 'lower' lobe is caused by Type

2, or the streamline-curvature instability (Malik 1986). For the smooth case, it can be seen that the upper lobe is much larger, and first occurs at a much lower Reynolds number than the lower lobe. From this it can be ascertained that for smooth disk flow, and for low conditions of roughness, any unstable flow is most likely caused by the cross-flow instability as the flow moves outwards with increasing radius. In this case, the onset of the cross-flow instability is found at about Re = 281±1 for the smooth disk, which compares favourably to the values of 285 and 287 obtained by Malik (1986) and Mack (1985) respectively; the small discrepancy is most likely due to truncation and rounding errors.

As the ratio of the roughness level is increased however, some changes become apparent in the stability of the flow. Firstly, the overall size of the area of instability decreases, becoming thinner and suggesting an overall stabilising effect of the roughness. Secondly, the upper lobe decreases in size significantly, whilst shifting to higher Re. Lastly, the lower Type 2 lobe begins to increase in size, growing in both width and length and shifting upstream to lower Reynolds number.

The reduction of the main cross-flow instability lobe as roughness is increased can be explained by the decrease in the mean flow velocity of the radial wall jet seen in Chapter 3.1. This reduction in the strength of the cross-flow element of the boundary-layer would explain the stabilisation of that instability, as the mean velocity and vorticity of the flow passing through the inflection point will be less, and so the tendency to become unstable will also be reduced.

Similarly, the growth of the small, streamline-curvature instability lobe can also be explained by physical changes in the mean flow velocity profiles. Recalling the

parameter $\kappa = \delta/r_o$ derived by Itoh (1996) to describe the effect of the streamline-curvature, we see that it is dependent on two factors; the radius of the curved streamlines, and the thickness of the boundary-layer. The streamline radius is simply the local radius of the resultant velocity streamlines. As the wall jet velocity decreases and the azimuthal velocity remains approximately steady, the streamlines of the resultant flow become a tighter curve with a smaller radius. In addition to this, in Chapter 3.1 a thickening of the boundary-layer was observed as roughness was increased, thus increasing the value of δ. Together, these two changes increase the streamline-curvature parameter κ. Hence, it can be seen that as the mean velocity profiles experience this thickening, and the streamlines gain a tighter radius of curvature, the result is a growth in the streamline-curvature instability mode.

These changes in the neutral curves become significant at between ratios of 0.1 and 0.2 where the unstable mode at the lowest Re switches from the upper lobe to the lower lobe. In fact, this switch in the location of the critical Re occurs at approximately $\delta/\gamma = 0.12$. This could signify a switch in the dominant mode, although more crucially one must look at growth rates of each instability mode rather than just simply where the flow becomes unstable.

4.2 Instability growth rates

To do this, we look at the size of the growth rate, $-\alpha_i$ and see how it changes with roughness ratio at each Reynolds number. Figure 4.2 shows the relative growth rates of the different roughnesses by plotting them on a third axis normal to the

plane of the neutral curves in Figure 4.1. This approach is consistent with that taken by Garrett (2010)

For the smooth disk case shown in Figure 4.2a, as expected, the Type 1 cross-flow instability growth rate is much larger than the Type 2 streamline-curvature instability. In fact, for the smooth case, the growth rate of the lower lobe (to the left of the 3D plot) is barely visible, which conforms to the widely held view that the cross-flow instability dominates the flow over a smooth disk at all radii for stationary modes.

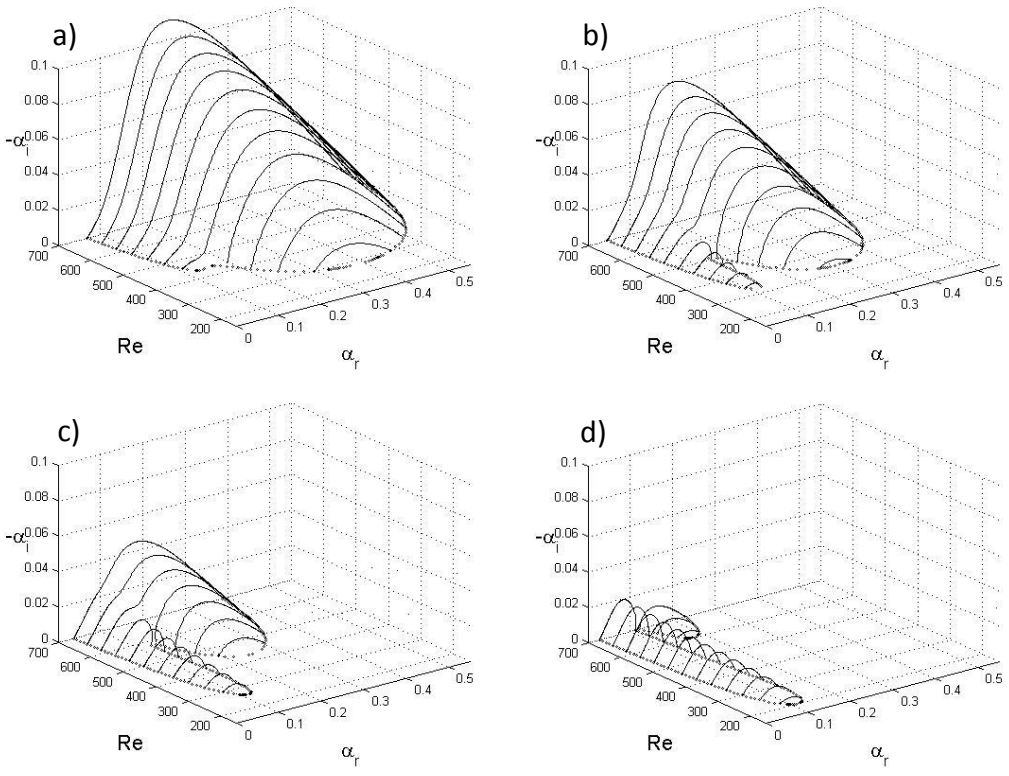

Figure 4.2 - Instability growth rates for the neutral curve of the smooth disk a) $\delta/\gamma = 0$ and rough disks b) $\delta/\gamma = 0.12$, c) $\delta/\gamma = 0.2$, d) $\delta/\gamma = 0.3$.

If the roughness ratio is increased to 0.12, the point at which the modes switch in Figure 4.1, we see once again the growth of the streamline-curvature mode and the reduction of the cross-flow but it is clear from Figure 4.2b that the growth rate of

the latter mode still dominates. Any Type 2 instability that forms will quickly be dominated by the growth rate of the Type 1 instability many times larger than it. Increasing the roughness ratio further to 0.2 (Figure 4.2c) sees an additional reduction in the growth rate of the cross-flow mode and for a short range of Reynolds numbers, the growth of both instabilities is approximately equal. (The cross-flow eventually dominates after Re=550, but we know from previous studies that this region is likely to be both turbulent and nonlinear in nature, and thus the linear stability behaviour at that point is moot). This level of roughness therefore could be a second possible switching point in the development of the rough boundary-layer flow, as it details the critical roughness needed for the growth rate of the Type 2 instability to overcome the Type 1. For roughnesses above this critical level, such as in Figure 4.2d, it can be seen that the streamline-curvature mode both occurs further upstream and dominates in terms of growth rate as Re increases.

In terms of growth rates, it can be seen from the whole of Figure 4.2 that although roughness has an effect on both instability modes, it is perhaps most influential on the Type 1 cross-flow instability. Increasing roughness up to a ratio of 0.3 has the effect of reducing the growth rate of this mode from $-\alpha_i > 0.1$ in the smooth case down to $-\alpha_i < 0.02$ for the largest amount of roughness. Meanwhile, the roughness only acts to increase the Type 2 mode from $-\alpha_i < 0.01$ to $-\alpha_i \approx 0.02$. Thus any changes in the stability or structure of the flow may well be due to the roughness reducing the cross-flow instability rather than promoting the streamline-curvature mode. Looking at the steady flow profiles from Chapter 3.1, it seems

most likely that this reduction in the cross-flow mode is caused by the roughness influencing the height of the inflection point in the boundary-layer and reducing the velocity of the wall jet. This conclusion is based on how the radial profile and the inflection point are so closely linked with the formation of the cross-flow instability in the literature.

4.3 Azimuthal wavenumber

Another variable that can be investigated in terms of the neutral stability is the azimuthal wavenumber β_r which is the real part of the azimuthal quantity $\bar{\beta}$ used in Equations 3.12-3.15. The azimuthal wavenumber is a value that can be directly compared to the physical quantity of the number of vortices seen around the disk. As mentioned in Chapter 2.2, the general consensus for the experimental smooth disk is a value of between 28-32 fully developed spiral vortices. For numerical studies, values as high as 113 have been seen (Gregory et al. 1955), but this value was calculated without considering viscous, Coriolis and streamline-curvature effects. In Chapter 3.2 the parameter β was replaced in Equations 3.12-3.15, and so to convert the azimuthal wavenumber back to the physical number of vortices, it needs to be multiplied by the Reynolds number at which the value was taken.

$$\beta = \beta_r Re \tag{4.1}$$

Using this formula, we can plot the points of neutral stability against the number of vortices expected at that Reynolds number to form Figure 4.3. Unsurprisingly, there is a stabilising effect of the increasing roughness ratio again, as the region of instability decreases in size. Similarly to Figure 4.1 one can still observe the shrinking of the upper lobe and the growth of the lower lobe, but also there is a

new interesting effect. The vortex number at which instability first occurs noticeably decreases as well. For the smooth case, the instability first occurs at Re = 281 with a vortex number of approximately 22, which is consistent with previous smooth disk stability calculations (Malik 1986). It is worth pointing out that this value for the number of vortices is not directly comparable to those seen in experiments, since this is the initial value for the vortex number, at the first point of instability. In experiments, the spiral vortices generally are not visible until further downstream when they have increased in number through bifurcations. Jarre et al. (1996b) note that the discrepancy between the wavenumber of 22 seen in the numerical curves and their experimental observations of 32 could be caused by the nonlinear effects present on the disk, which are not taken into account with the linear stability study. This idea is supported by the earlier work of Wilkinson and Malik (1985), who kept nonlinear effects to a minimum during their experiments by using a flow control panel to draw away any turbulent forcing. With these low turbulence levels, they managed to record the exact number of vortices at each radius of the disk. In Figure 6 of their paper the number of vortices increases sharply from the critical location of Re=289 to reach a value of approximately 23 vortices, before then slowly increasing through vortex bifurcations to the familiar value of 32.

The most unstable azimuthal wavenumber increases with Re from the critical value, and the experimentally observed values reflect this increase. Thus, an important result is that as the level of roughness is increased in this study, the initial critical vortex number decreases, dropping to 20 for the upper lobe at a roughness ratio of

0.2. For the lower lobe, the reduction in vortex number is even more noticeable; a reduction from 21 for the smooth case, to 11 for a roughness ratio of 0.2.

It was first noticed by Stuart (1955) and confirmed by Malik (1986) that the wavenumber is greatly susceptible to changes in viscosity. Malik notes that the wavenumber at high Reynolds numbers, where viscous effects are negligible, differs greatly from the wavenumber at the critical point. Because of this, it makes sense that the viscous mode is affected to a higher degree than the inviscid when subjected to increasing roughness.

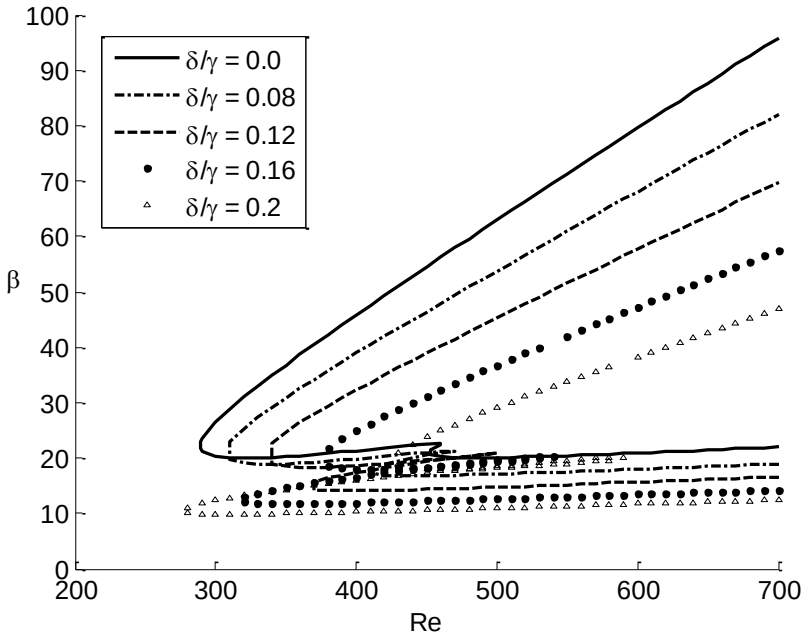

Figure 4.3 - Neutral curve plot against β with increasing roughness ratio.

This reduction in initial vortex number shows some similarity to the reduction of spiral vortices seen by Watanabe et al. (1993) as they increased the size of the roughness on their disk. Because of the link between critical wavenumber and number of developed spiral vortices, it seems likely that this stability result is the

cause of the effects seen by Watanabe, and will be confirmed with experiments in Chapter 6.

The values of the initial vortex numbers from the curves in Figure 4.3 can be recorded along with the values taken from other curves for ratios not shown here.

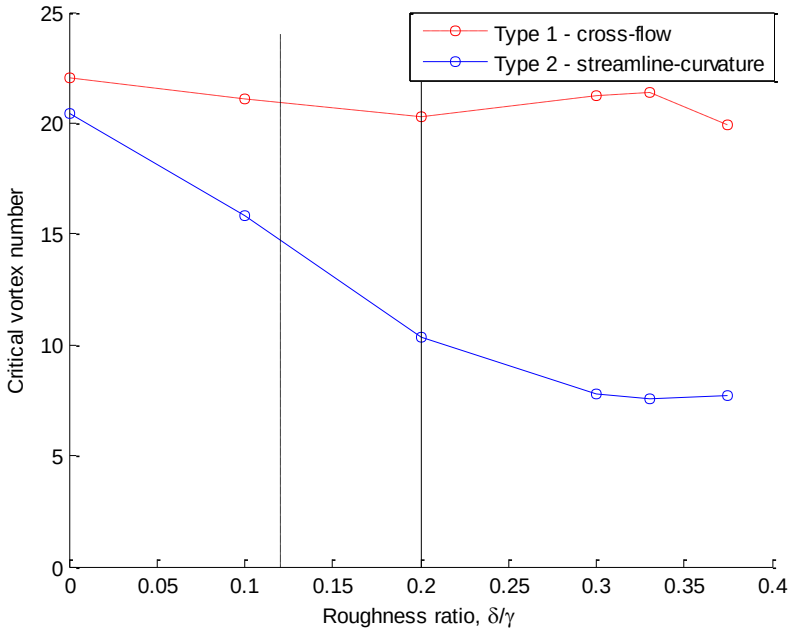

Figure 4.4 - Initial azimuthal wavenumber for Type 1 lobe and Type 2 lobe. Vertical lines indicate possible mode switch locations.

From Figure 4.4 we can see that the predicted trend of the number of azimuthal vortices is indeed downwards with increasing roughness ratio, with the slope of the Type 2 lobe greater than the Type 1 lobe. Because of this difference in slope, one might expect that if there was a switch of the dominant modes, one of the observable changes in the experimental data could be a change in the slope of spiral vortex number too, providing of course that the Type 2 mode still appear as vortices once dominant.

The possible switch locations have been added to the plot; the point at which the critical Re for the Type 2 lobe overtakes Type 1 ($\delta/\gamma = 0.12$), and the point at which the growth rate of the Type 2 lobe dominates Type 1 ($\delta/\gamma = 0.2$). At one of these points, one might expect to see a sudden drop in the number of observed experimental spiral vortices as the mode switches from the upper slope to the lower.

It is also pertinent to look at the critical Reynolds number at which the instabilities first form for each roughness ratio. This will give us the range of Reynolds numbers for which one would expect to see instabilities first forming in the experimental data.

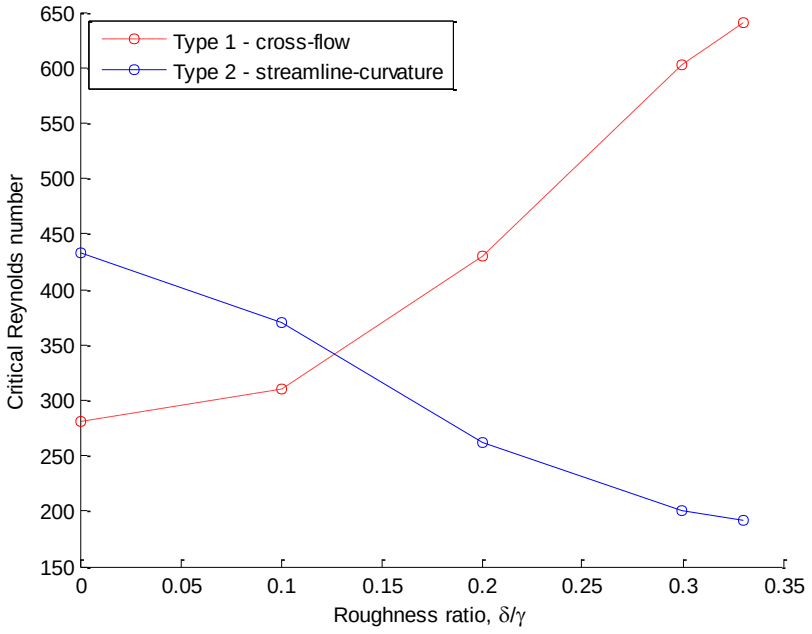

Figure 4.5 - Points of initial instability taken from neutral curves for increasing roughness ratio.

Figure 4.5 shows clearly the point at which the switch between the two lobes for the critical Reynolds numbers occurs. The markers show the decreasing Reynolds numbers for the initial cross-flow instability location and the increasing location of

the streamline-curvature instability. These curves are another way in which one can look for mode switches, by comparing them to the experimentally obtained points of initial instability and looking for any change in the behaviour as the roughness is increased. The results of this will be discussed in Chapter 6.6.

An important point to note is that if there is no mode switch to the streamline-curvature mode, and instabilities continue to be caused solely by the cross-flow mode, then the point of initial instability should, in theory, be delayed by increasing the amount of roughness. This in turn could have the effect of delaying transition to turbulence.

4.4 Wave angle

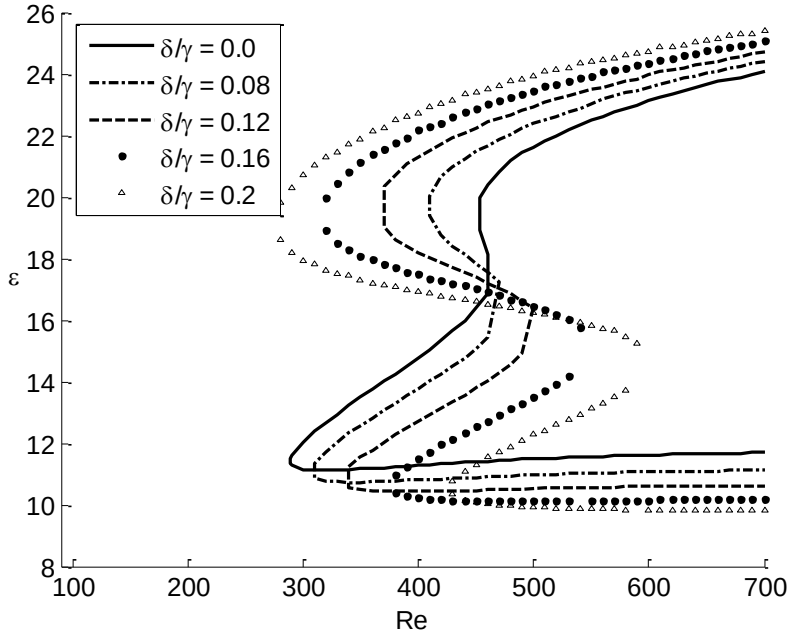

Figure 4.6 - Neutral curve plot against ε with increasing roughness ratio.

The range of neutral stability can be viewed through one other parameter plane, the angle of propagation of the disturbances, or wave angle ε. This parameter is

simply the angle of the resultant wave with respect to the radial axis, and can be calculated simply using the formula

$$\varepsilon = \tan^{-1}\left(\frac{\bar{\beta}}{\alpha_r}\right) \tag{4.2}$$

Figure 4.6 shows the relationship of changing neutral curve with increasing roughness ratio. Note that for the wave angle neutral curve, the lobe representing the cross-flow instability is on the bottom, while the streamline-curvature lobe is on the top. The situation is the same as before, with growth of the Type 2 mode and a reduction in the Type 1. However, there is a difference in that we do not see as great a shift in the values for the initial wave angle for Type 1, and there seems to be no shift at all for Type 2. It does not therefore seem that the wave angle is affected by roughness in the same way that the wave number is.

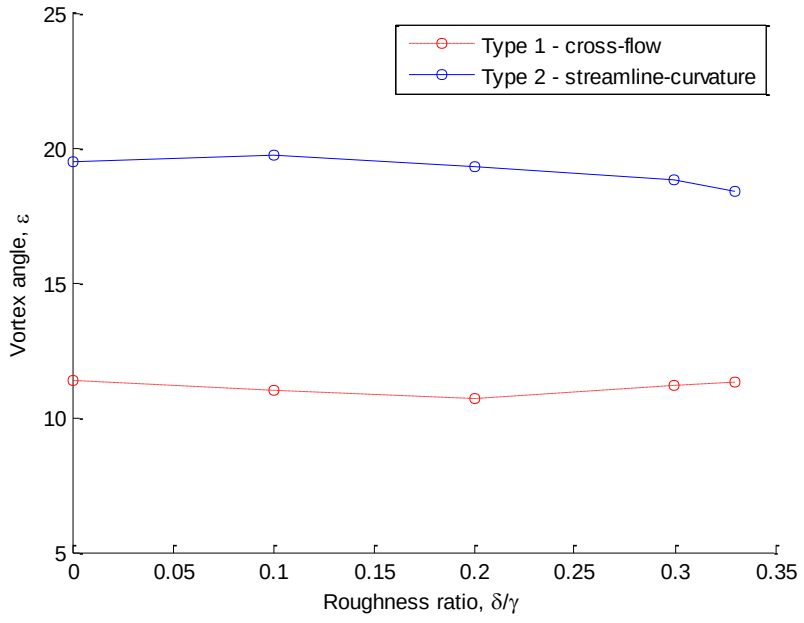

Figure 4.7 - Predicted initial wave angle with increasing roughness ratio

This is consistent with Stuart (1955) and Malik (1986), who both note that wavenumber is more susceptible to changes in viscosity than the wave angle, and so it seems plausible that roughness affects the former more than the latter as well. Nevertheless, there remains the switch between the two lobes in this plot as well. While the typical 13° wave angle seen in most experiments up to now is linked to the Type 1 mode instability, perhaps as the mode is switched there will be a shift in the angle of the wave as roughness is increased. The predicted initial wave angle for both modes is shown in Figure 4.7 for increasing roughness ratio. Similar to the plot for predicted vortex number, one might expect the wave angle to increase to around 19° should there be a switch to the Type 2 instability, otherwise there should be no expected change of the wave angle. Experimental results addressing this issue are presented in Chapter 6.2.

5 Experiment arrangement

5.1 Experimental equipment

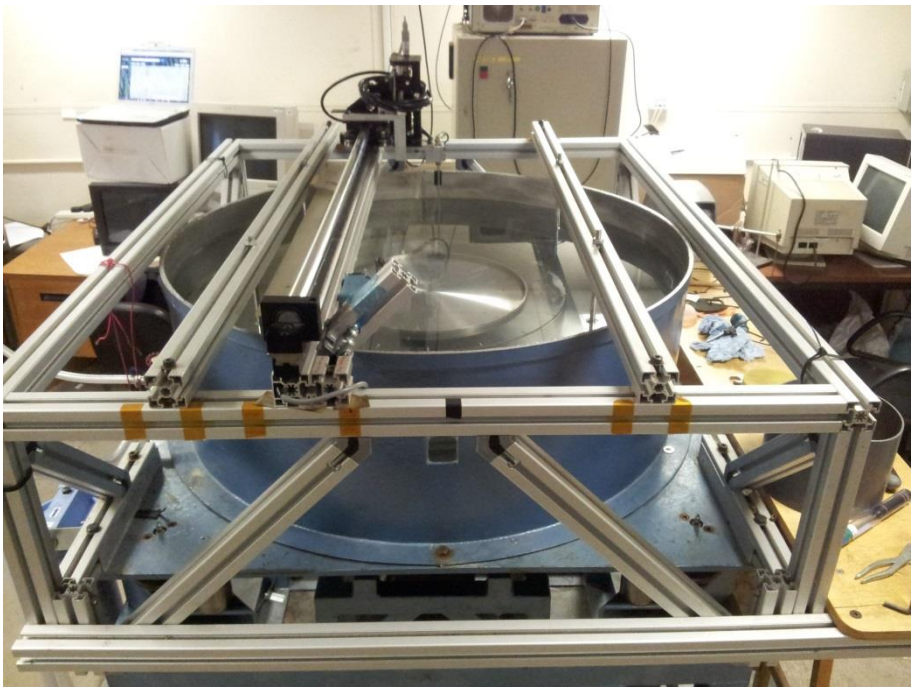

Figure 5.1 - Rotating disk facility

The rotating disk facility shown in Figure 5.1, and in diagrammatic form in Figure 5.2 already existed at the University of Warwick at the beginning of this study having been developed by Colley as part of his PhD project (Colley 1997), and so it was only necessary to adapt it for use. Any technical details more detailed than those described here can be found in his thesis. The facility consists of a 500 litre tank surrounding a rotating turntable, above which a 2-axis traverse moves a hot film probe holder in the radial and axial directions. The traverse allows the probe to be positioned at increments of 1mm in the radial direction and smaller increments of 10µm in the axial direction (with accuracies of 0.5mm in the radial direction, as this is done by eye on a fixed scale, and 1µm in the axial using a Vernier scale).

Therefore the probe can be placed at a number of radii in the flow and at multiple heights in the boundary-layer. Since the flow is axisymmetric, the need for positioning in the azimuthal direction does not arise. From Equation 2.3 it can be seen that the Reynolds number of the flow is based on the radial distance along the disk and the rotational speed and is given by:

$$Re = r\sqrt{\frac{\Omega}{\nu}} \tag{5.1}$$

From Equation 5.1 it can be seen that the range of Reynolds numbers on the disk can be changed by increasing or decreasing the rotation rate Ω for fixed radial distances, or for fixed rotational velocities by moving the radial location further outwards.

The height of the probe in the boundary-layer above the disk can be compared to the theoretical non-dimensional height by converting using the formula

$$\zeta = Z^*\sqrt{\frac{\Omega}{\nu}} \tag{5.2}$$

where Z^* is the dimensional height, Ω is the rotational velocity and ν is the kinematic viscosity of the medium. This allows the height to be compared to other studies using different equipment as well as theoretical axial dimensions as well.

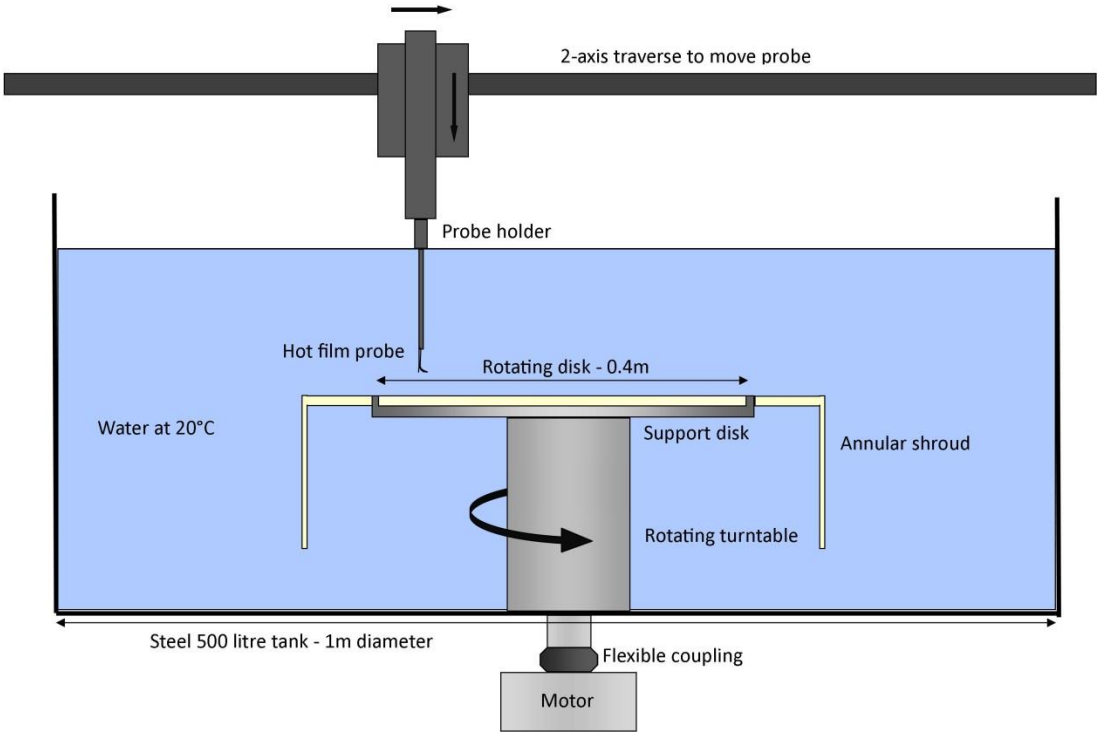

Figure 5.2 - Rotating disk tank set-up.

The disk itself sits on a steel support disk, which itself is bolted to a rotating turntable in the centre of the tank. The disk rests on three levelling screws which ensure the disk is as flat as possible with respect to the traverse axis and probe. The whole tank rests on four air-filled rubber supports, which reduce any vibrations from the motor travelling through the floor and into the tank via the frame.

The turntable is rotated by a Bosch brushless DC servo motor which is connected via a flexible rubber coupling to reduce vibrations. The motor is controlled by a separate PC running the Trio Motion software package. The software utilises programs written in the Trio BASIC language, which coordinate the motion of the motor as well as the triggered timing of the data collection. The disk is spun by the motion controller at a rotational velocity of $\Omega = 2\pi f_D$ where f_D is the rotating frequency of the disk in hertz and Ω is in radians per second. The motor's speed is accurately controlled via a feedback loop by an encoder placed on the shaft. Using a

tachometer, the velocity of the disk was found to be accurate to within ±0.002 rev/s, or approximately ±0.01 rad/s.

Surrounding the disk and support disk in the tank is the Perspex annular shroud which helps prevent recirculation of the turbulent flow and subsequent turbulent noise being introduced back into the boundary-layer and stimulating the flow early. The benefits of this shroud are discussed in the paper by Colley et al. (2006), where results taken using the shroud have substantially less noise than results taken with a lid over the disk, such as in other rotating disk studies. Care is taken to ensure that the shroud is level with the edge of the disk and not impinging the rotation of it, causing unnecessary vibrations. The shroud itself is suspended from the top of the tank support frame and can be raised and lowered at each of the four corners, thus ensuring it is as flush as possible with both the support disk and the main disk. The small gap between the disk edge and the shroud is approximately 1-2mm.

The water in the tank is filtered mains tap water, which can then be filtered again through an underwater circuit to remove particles of less than 0.1µm. The circuit that the water is pumped round remains submerged at all times in order to prevent cascading in air. This reduces the amount of air saturated in the water and helps prevent air bubbles forming on the hot film surface during testing. After being filtered, the water is left to stand overnight to allow for any air in the system to leave.

To keep the water at a constant temperature, the room in which the tank sits is temperature controlled to be at approximately 20°C, and subsequently the water

remains within 0.1°C of this value and does not change over the time period of a few hours; the time it takes to perform one set of results.

The velocity fluctuations are measured by a hot film probe connected to an IFA300 hot film anemometer system supplied by TSI Instruments Ltd. Hot film anemometry is ideal for use in this situation as it can deal with the rapid fluctuations present in the rotating disk boundary-layer. The system uses hot film rather than hot wire probes, since the former are designed to be more rugged and offer better measurements in low velocity liquid flows. The probes themselves are TSI model 1218-20W single sensor, right angled film probes which are made from a tungsten wire 1mm long and 50µm wide with a platinum coating. Data from the hot film probe is fed through an A/D converter into a PC running TSI ThermalPro software for data analysis.

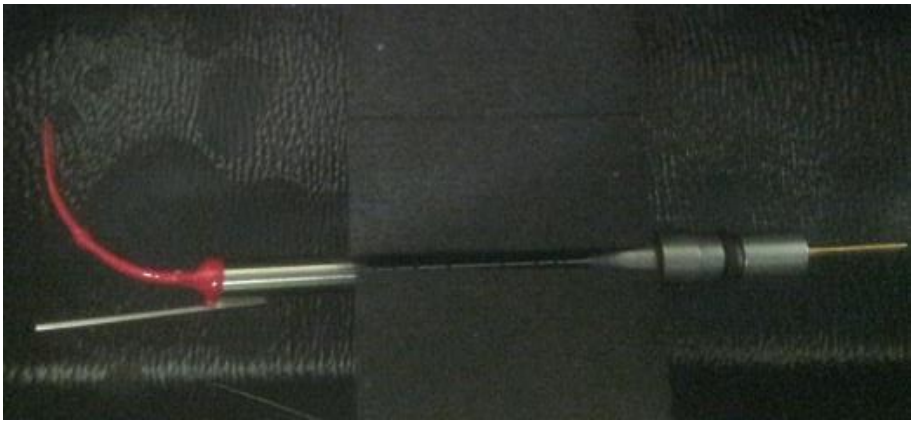

Figure 5.3 - TSI 1218-20W hot film probe.

Each probe has a wire 'heel' protruding from the back which protects the sensor from touching the wall of the boundary-layer it is measuring (see Figure 5.3). This heel was used to calculate the distance of the probe from the surface of the disk. Before testing, the distance between the bottom of the heel and the sensor was

measured using a microscope, then the probe carefully lowered onto the slowly rotating surface until a quiet noise indicated the heel was just scraping the disk. This point would then be recorded as the lowest possible position of the probe in the boundary-layer. This was done as carefully as possible to avoid damaging the surface of the disk.

Due to the actual probe sensor being offset from the probe shaft by 12.7mm, it was necessary to shift the probe traverse each time the need arose to switch between azimuthal and radial readings. When the probe was recording radial data, the probe sensor would be lined up with the probe shaft on the radial axis of the disk, but for azimuthal readings, simply turning the probe holder 90° causes the sensor to be offset from the radial axis by 12.7mm. This means that the probe sensor wire is no longer parallel to the radial axis and is no longer facing directly into the azimuthal flow. To remedy this, the whole probe traverse would be moved 12.7mm whenever the probe was rotated to account for this offset and ensure the azimuthal readings were as accurate as possible.

Velocity readings are triggered by an optical sensor on the main rotating shaft, just above the flexible coupling. A metallic reflective timing mark triggers the infra-red sensor once per revolution, which then begins the data acquisition, allowing the anemometer system to collect data from the same angular position on the disk each time. This is especially important for when the data is ensemble averaged in Chapter 6.2.

Data is acquired at 1000Hz for 1.024 seconds at a time before a low pass filter of 300Hz is applied to remove unwanted higher frequencies.

5.2 Roughness

To help determine the roughness levels necessary to produce significant roughness effects, we choose to use the classic classification scheme which categorises a surface as either *hydraulically smooth, transitional* or *completely rough* (Schlichting & Gersten 2004) mentioned earlier. These classifications were developed primarily for flat plate and pipe flow roughnesses in a turbulent flow rather than for three-dimensional rotating disk flow, but the likelihood is that the levels of roughness will at least be the correct order of magnitude, and are therefore justified since no better scheme is available for use.

The classification scheme uses the roughness parameter Θ to describe the level of roughness, where

$$\Theta = \frac{k_s v^*}{\nu} \tag{5.3}$$

In which k_s is the typical roughness height, ν is the kinematic viscosity and $v^* = \sqrt{\tau_0/\rho}$ is the friction velocity, where τ_0 is the wall shear stress and ρ is the density of the fluid. The scheme uses the following values for the roughness parameter to describe the surface; hydraulically smooth for $\Theta < 5$, transitionally rough between $5 < \Theta < 70$ and completely rough for $\Theta > 70$.

For operating conditions typical within the experimental facility, Equation 5.3 produces estimates for the roughness height needed to induce the above regimes on our disks, resulting in a transitional regime of between 36µm and 500µm. Thus this study will need a level of roughness which is within this range, while the smooth comparison case will need to be below the lower bound of 36µm. By using

Equation 5.2 in conjunction with the numerical values of the boundary-layer profiles taken from Owen and Rogers (1989), it is possible to calculate the formula for the physical thickness of the boundary-layer. If one takes the edge of the boundary-layer as the point where the azimuthal flow is reduced to 1% of the disk speed, then the following formula describes the physical thickness of the boundary-layer using Table 3.1 from Owen and Rogers:

$$\text{Boundary-layer thickness} = 5.5\sqrt{\frac{\nu}{\Omega}} \tag{5.4}$$

For this study, the disk will be rotated between 6.28 rad/s and 10.99 rad/s and thus the boundary-layer thickness can be varied between 1.66mm and 2.19mm. The lower bound of the transitional roughness regime can therefore be as little as 1.6% of the boundary-layer, while the upper bound can be as much as 30%. By varying both the roughness height and the boundary-layer thickness (via the rotation speed) a wider variety of roughness effects can be studied.

5.2.1 Disk manufacture

In order to successfully compare any experimental results with numerical data, a rough disk surface needed to be produced that would mimic as closely as possible the wavy surface described by Equation 3.1. Many different ways of producing rough surfaces were considered; from rapid-prototyping the disk using resin, which proved to be too expensive, to gluing sandpaper to the surface, which did not produce a roughness with enough control over the height and pitch of the roughness elements. Instead, it was decided to cut grooves into an aluminium disk in a concentric pattern, as seen in Figure 5.4 to simulate the sinusoidal surface function.

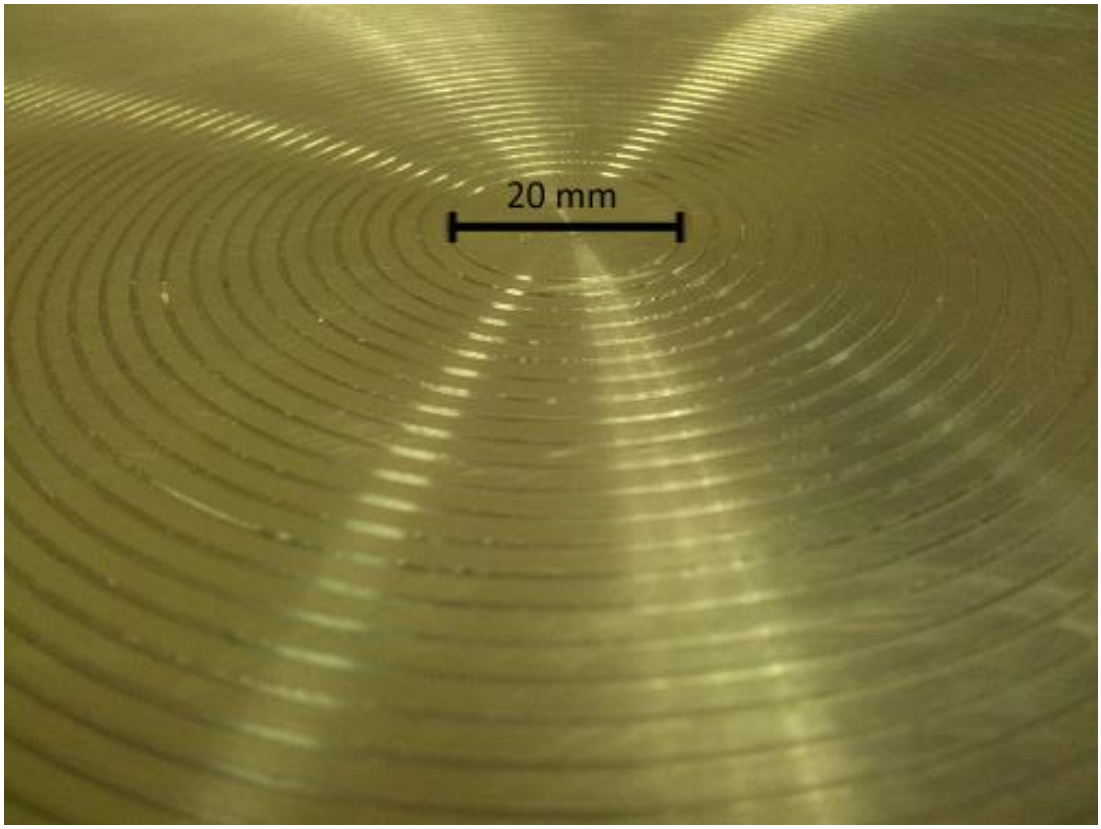

Figure 5.4 - Grooved disk example.

The disks were made using grade T6082 aluminium plate cut into 390mm diameter circles which were 12mm thick. The top surface of the disk was machined to be as smooth as possible. Grooves were then cut into the top surface of each disk using a lathe and an acutely angled lathe tool. The grooves were cut to different depths and at different distances apart as determined by Table 5.1 below.

Visually, the disk in Figure 5.4 looks very similar to that used in the numerical study. To properly compare with the sinusoidal surface function, and to enable us to see the profile of the rough surface however, the disks were placed on a Taylor-Hobson Talysurf Profiler. The profiler rests a sharp point on the disk surface and draws it along for a reasonable distance. The minute height changes of the point as it moves over the grooves helps develop a trace of the surface. The trace showed that the

amount of roughness on the surface of the aluminium disks between the grooves was in the smooth regime mentioned previously, i.e. in the order of 10 microns. One of the resulting traces for a rough disk is shown in Figure 5.5 where it is superimposed over a cos wave which has a roughness ratio of 0.1. The disk used was one with a groove depth of 0.1mm and a groove pitch of 0.5mm. This superposition shows that the cos wave is an adequate approximation for the grooved surface of the disk.

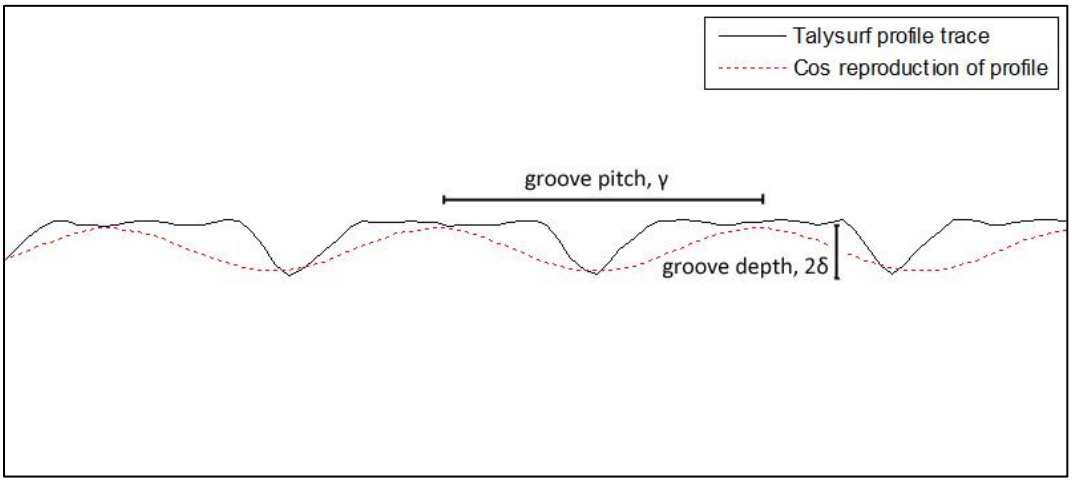

Figure 5.5 - Comparison between rough disk trace and surface function.

The comparison In Figure 5.5 helps to visualise how the depth of the profile trace is related to the amplitude of the cos wave. Because the total height of the wave from trough to peak is 2δ, the groove cut into the disk must be equal to 2δ in depth. Thus the effective height with which to calculate the roughness ratio needs to be using half the manufactured depth. With this in mind, 12 disks were manufactured with groove depths and pitches that gave a range of roughness ratios, as well as 5 disks with the same ratio (0.1) but different roughness depths, to see if this has any effects on the flow.

Groove depth	Groove pitch	Effective δ	Effective γ	Ratio δ/γ
100	300	50	300	0.167
100	400	50	400	0.125
100	500	50	500	0.100
100	700	50	700	0.071
100	750	50	750	0.067
200	1000	100	1000	0.100
300	500	150	500	0.300
300	1500	150	1500	0.100
400	2000	200	2000	0.100
500	750	250	750	0.333
500	1250	250	1250	0.200
500	2500	250	2500	0.100

Table 5.1 - Manufactured aluminium disks. All dimensions are in microns.

As can be seen in Table 5.1, all the disks are within the transitional roughness regime mentioned above i.e. have a groove depth between 36µm and 500µm (provided the classification scheme is applicable to the rotating disk case), and yet cover a range of roughness heights and ratios.

To compare the rough disks with a smooth case, a hydraulically smooth disk had to be made as well. For this, a 388mm diameter glass disk cut from 10mm float glass was manufactured. The disk was measured using the Talysurf profiler to have an average roughness height of 9µm, which places it in the smooth regime. The glass disk has the advantage of having a smoother, less corrodible surface compared to a polished metal surface.

5.3 Operating procedure

To operate the facility, the following procedure needs to be performed. Firstly, the tank is filled with mains tap water, passed through a 0.5µm filter, until the height of the water is a few centimetres below the top of the tank. This provides enough water in the z-direction to cover the disk beyond the boundary-layer as well as reducing the likelihood of the whole body of water rotating with the disk. The water

in the tank is then pumped round a circuit for a few hours, through a smaller 0.1µm filter to remove any remaining particles which could affect the hot film probes later. To rid the water of any air bubbles, the water is then allowed to stand overnight, with approximately 25ml of bleach added to the water to prevent algae formation in the water. It was found that even with the water being changed every couple of weeks, the water being kept relatively warm at 20°C allowed algae and other contaminants to form fast enough to interfere with the probe, so the bleach was added to inhibit this algal growth. As the amount added is only 0.006% of the total amount of water in the tank, there should be no damage to the probe, nor any difficulties with changes in viscosity or electrical conductivity of the water. Additionally, every few weeks, the sensor of the probe would be cleaned with distilled water to clean off any contaminants built up.

With the total mass of water now in the tank, the air-filled supports holding it up can be pumped up to ensure no vibrations are transmitted through the frame from the motor. Air is added to each of the four rubber supports until the tank is suspended by them, while the tank is kept level via the use of a spirit level.

Once the water has settled, the disk can be placed on top of the support disk, and levelled using the three levelling screws underneath. By attaching a plunger-type micrometer to the probe holder and lowering it onto the surface, each disk can be levelled to a satisfactory degree each time a new disk is used. Each screw is usually levelled to within ±0.01mm of the others. Any out-of-flatness after this levelling has taken place is due to the disk not being completely flat between the screw locations, resulting from the manufacturing process and about which nothing can

be done. The main effect of this on the results is that it introduces a large peak in the frequency data around 1Hz, i.e. approximately one disturbance per rotation, which can be ignored. Using the micrometer, it was found that the maximum amount of out-of-flatness for any of the aluminium disks was < 0.15mm. This value is unfortunately in the same order as the roughness grooves, but due to the averaging used to create both the mean flow profiles and the velocity traces, this should not have an effect on the results, as any change in velocity caused by the changing height of the disk will be averaged over the course of one rotation. The smooth glass disk was found to be considerably flatter due to the floating process used to create it, and had a maximum out-of-flatness of 0.01mm. After the test disk is installed, the Perspex shroud is lowered around the disk and secured tightly to prevent vibrations during rotation.

The probe can then be placed in the probe holder, and rotated to either take radial or azimuthal readings (along with the associated adjustments of the probe traverse to reflect the sensor offset). The probe can then be lowered until it is at the desired height over the surface of the disk, using a micrometer scale to measure the distance above the disk. Once the probe is in place, the disk can then be spun up to the correct rotational speed, ready to take readings.

5.3.1 Calibration

In order to plot velocity profiles, it was necessary to be able to calibrate the hot film probes successfully. To calibrate a hot wire or film probe, it needs to be placed in a known mean flow where the voltage can be recorded at that known velocity. In previous studies on this facility, calibration was done using the radial traverse axis

to pull the probe through the tank at a variety of speeds. However, halfway through this current study, the radial traverse mechanism broke irreparably, and so an alternative calibration method needed to be developed. One of the ideas for a replacement was to attach the probe to a radial 'arm' which itself is connected to the centrally rotating turntable (with the support disk removed). Thus, the probe could be swung around in a circle at different speeds to simulate the linear velocity needed for calibration. However, there were problems with this, as it was found that the probe moving through the water increased the bulk velocity of the flow too much, causing an unreliable resultant velocity of the probe (Bertrand & Couderc 1978). Instead, it was decided to use a technique used by Lingwood (1996) to calibrate hot wire probes when there is no mean flow. For flow over a disk, the only known reference velocity is the speed of the disk surface, and so using the assumed theoretical velocity profiles over the surface of the disk, one can predict the velocity of the flow at a measured height above it. Placing the probe at this height above the disk, the rotation speed can be altered to increase and decrease the flow velocity, and a calibration curve can be created by measuring the probe voltage at these known velocities. The probes were therefore calibrated each time (once every few days) over the smooth glass disk, and these calibrated probes were then used for the flows over both the smooth and rough disks.

5.3.2 Yaw angle correction

Because the main fluid flow in the boundary-layer is made up from a superposition of both the radial and azimuthal flow components, there exists the problem of 'yaw

angle correction'. Any probe angled to measure a specific flow component, will experience effective 'along sensor cooling' from the perpendicular flow component. Hence a yaw angle correction will need to be applied to correct for this (Bruun 1995). This yaw angle is not necessarily the same for all heights above the boundary-layer either, as the ratios of radial and azimuthal components vary as you move up through the boundary-layer. Usually, the effect is either corrected for during calibration, or is calculated to be negligible. Colley et al. (1999) performed some simple tests to gauge the effect of yaw angle correction on the probe results for the facility used in this study. They discovered there to be a slight effect, and developed correction factors to deal with it, but did not use them in their own velocity profile data. For this study it is assumed that for any effect that does present itself, it should be approximately similar between different disk surfaces, and so can be ignored.

5.3.3 Velocity profile experimental procedure

The test disk is placed on the support disk in the tank of filtered water, and levelled using the three support screws underneath. The probe is attached to the probe holder and lowered into place above the disk, facing either azimuthally or radially depending on which velocity is to be measured. The height at which the probe resides above the disk is noted, and the probe is positioned at the radius required for a particular Reynolds number. The disk can then be spun up to the desired speed. The probe is then lowered to just above the surface of the disk; as close as possible before the 'heel' of the probe touches the disk. Readings are then taken at intervals of 0.1mm through the boundary-layer to plot the velocity at each height. Each point is made from an average of 3 readings, which itself is an average of a

block of 1024 points taken over one rotation of the disk. Profiles at Re = 300, 400 and 530 are taken for a range of disk roughnesses. All readings of height are non-dimensionalised via Equation 5.2 while velocities are non-dimensionalised by dividing by Ωr.

6 Experimental results

6.1 Velocity profiles

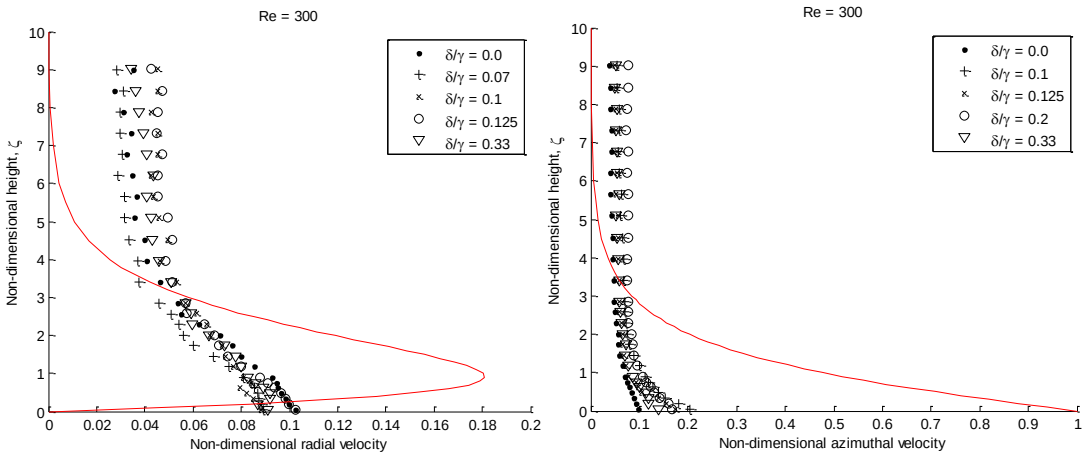

Figure 6.1 – Radial (left) and azimuthal (right) velocity profiles for disks of increasing roughness at Re = 300, Ω = 7.85. Solid line curve shows theoretical curve for a smooth disk.

Figure 6.1 shows the mean velocity profiles taken for 5 disks of varying roughness ratios at a Reynolds number of 300, i.e. in a laminar region of the boundary-layer. A theoretical curve taken from Owen and Rogers (1989) is shown for comparison. All experimental curves display the correct qualitative behaviour, yet there exists a discrepancy between them and the theoretical curves; they do not agree quantitatively. At high ζ this is to be expected, as the velocity of the flow far from the disk does not tend to zero in the manner predicted by theory. This is due to the core of fluid rotating above the disk which stems from the finite arrangement of the enclosed tank. Colley et al.(1999) noticed a similar discrepancy in their velocity profiles, and therefore positive fluid flow at high ζ is not necessarily anomalous.

However, the situation at smaller values of ζ cannot be explained in the same way. All five disks shown in the figure, experience a large reduction in velocity and definite slip at the wall that cannot be explained at this point. This predicted slip at the wall for all profiles is physically impossible. A yaw angle correction would perhaps explain a reduced velocity close to the disk for the azimuthal curve, but not a similar circumstance for the radial, which would experience a larger velocity here from the ‘along sensor cooling’ of the azimuthal flow.

The discrepancy cannot be caused by either the roughness or the out-of-flatness of some of the rough disks either, since the smooth disk profile is reduced by an equal amount, suggesting the problem is inherent in the anemometry system.

As all the profiles seem to be affected in the same way, it was decided to ignore the deviation from the theoretical curve and instead compare the profiles between each disk to see how the roughness affected the experimental results.

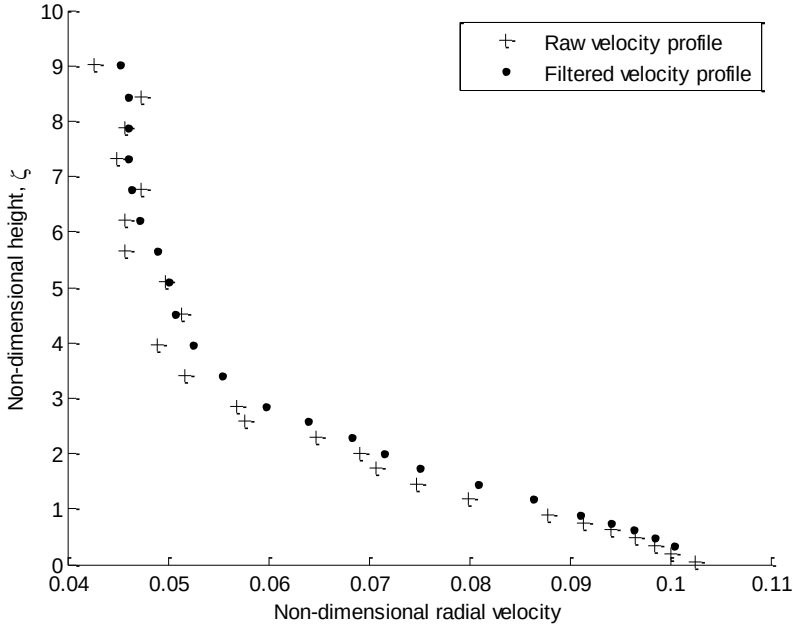

Figure 6.2 - Comparison of raw and filtered velocity profiles.

In order to decrease the amount of scatter in the mean velocity results, the points have been smoothed slightly with a 3-point moving average filter. This enables relevant features such as the inflection point to be observed more easily while retaining the general shapes of the curves. A clear example of this filtering is shown in Figure 6.2, from which it can be seen that the filtering does not alter the shape or position of the curve to a great extent. Instead it merely makes it easier to pick out the position of the inflection point.

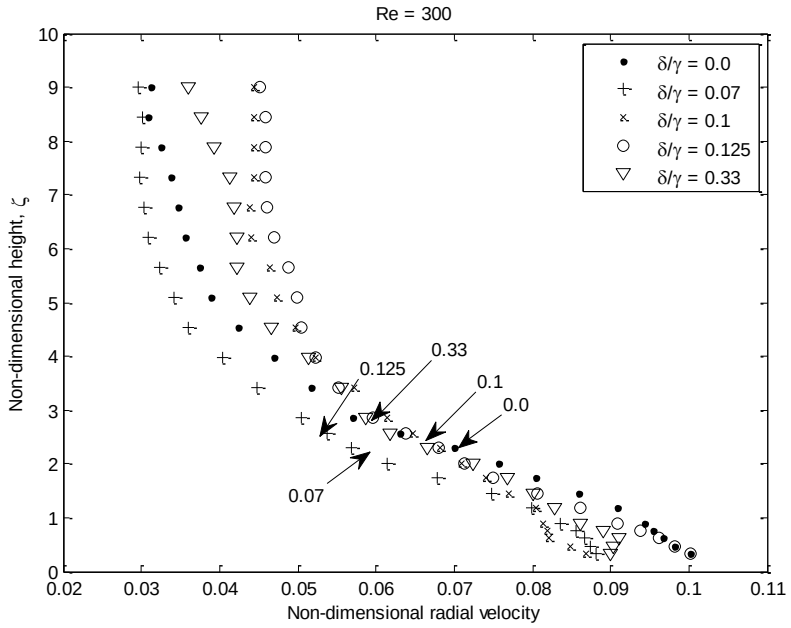

Figure 6.3 - Radial velocity profiles for disks of increasing roughness at Re = 300, Ω = 7.85. Arrows indicate the points of inflection for each curve.

Figure 6.3 shows the experimental radial profiles from Figure 6.1 in finer detail without the theoretical curve and with the smoothing filter added. Looking at the shape of the curves in Figure 6.3, as the roughness is increased from the smooth case with $\delta/\gamma = 0$, it can be seen that all the disks suffer from a drop in maximum velocity of the wall jet. This corroborates with what was found in the theoretical calculations in Chapter 3.1 as seen in Figure 3.3. The other feature seen in the numerical profiles, namely a thickening of the boundary-layer is seen for roughness ratios of 0.1, 0.125 and 0.33, but not 0.07. This is understandable since the boundary-layer thickening effect may not be noticeable for such a small amount of roughness. However, it seems that the general trend in the profiles does seem to match the numerical profiles. For each curve, the point of inflection has been marked with an arrow. Again with the exception of the 0.07 disk, there is an upward trend in the height of the inflection point in the boundary-layer, with the

increase in roughness ratio. This endorses what was seen in the numerical profile results. It is worth pointing out that the thickening of the boundary-layer and subsequent increase in the height of the inflection point are most likely not due to the roughness height simply protruding into the boundary-layer and forcing the profiles upwards. The physical heights of the roughness for the 0.07, 0.1 and 0.125 disks are all equal; the ratios differing only in roughness pitch, and thus these effects appear to be caused by the changing roughness ratio itself.

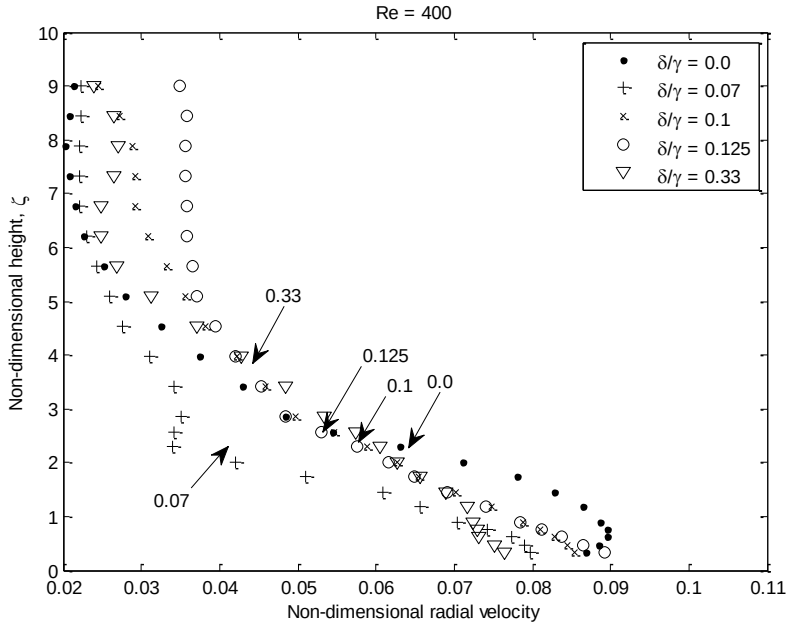

Figure 6.4 - Radial velocity profiles for disks of increasing roughness at Re = 400, Ω = 7.85.

The profiles do not change significantly as we move downstream to Re = 400 in Figure 6.4 which is as we would expect; previous velocity profiles for rotating disk studies have all shown the non-dimensional profiles to remain the same independent of radius, providing they remain in the linear region (Lingwood 1996; Zoueshtiagh et al. 2003). The fact that the experimental profiles do not vary as they move downstream helps validate the similarity solution made in the numerical

derivations earlier. The points of inflection again move upwards with increasing roughness ratio, proving that this feature is independent of radial position also.

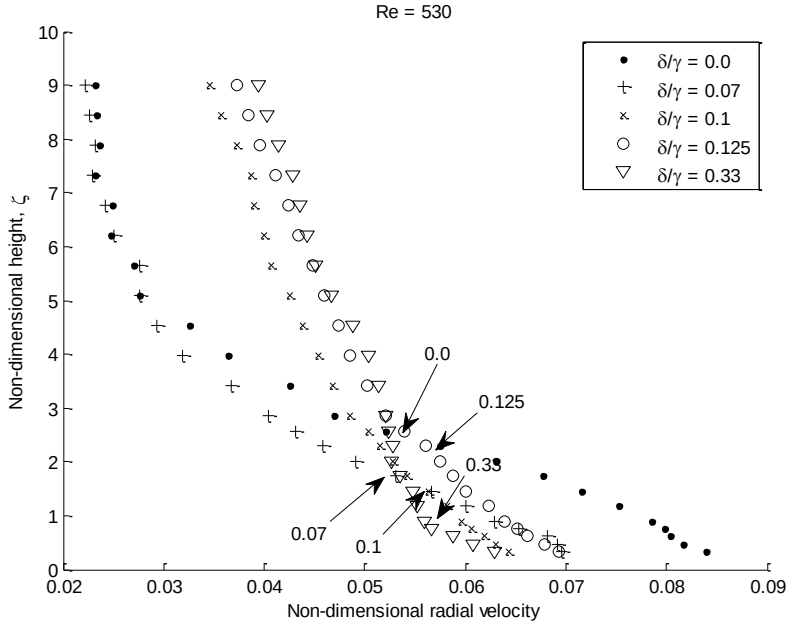

Figure 6.5 - Radial velocity profiles for disks of increasing roughness at Re = 530, Ω = 7.85.

Figure 6.5 shows the corresponding profiles for higher Reynolds number at Re = 530. The flow at this Reynolds number will be well into the transition region, if not fully turbulent for some of the disks. The effects seen in the laminar regions are once again visible, only now they are a lot more pronounced with the decrease in wall jet velocity and thickening of the boundary-layer much more obvious. This will in part be due to the expected change of shape of the profiles in a turbulent regime (see Lingwood (1996) and Colley et al. (1999) for the effects of turbulence on boundary-layer profiles) but it may also be due to the fact that the roughness has an even greater effect on the flow when turbulence is emerging. The steady profiles formed in Chapter 3.1 are only valid for laminar flow and so no comparisons can be made for experimental profiles taken at higher Reynolds numbers, but it is

interesting to see this effect continue into the turbulent regime. The inflection point effect however does not seem to continue past transition. Rather than increasing in height with increasing roughness, it appears the opposite is true for profiles in the turbulent region. The steep nature of the curves at this radius of the disk appears to force the inflection point down. Since the flow at this point is already turbulent, any effect the inflection point may have on the instability of the flow is irrelevant however.

These results for the radial velocity profiles are similar to those found by Watanabe et al. (2007) when they looked at the effect of cutting fine spiral grooves into a rotating enclosed disk. Watanabe cut fine spiral 0.1mm deep grooves into a disk, to look at the effects on drag reduction. In Figure 10 of their paper, they plot the modified velocity profiles for a smooth disk and for a disk with spiral grooves, and show that for the grooved disk there is a definite reduction in velocity at all radii. There does not seem to be any thickening of the boundary in their study, although this could be due to the disk being enclosed, thus affecting the boundary-layer as z increases.

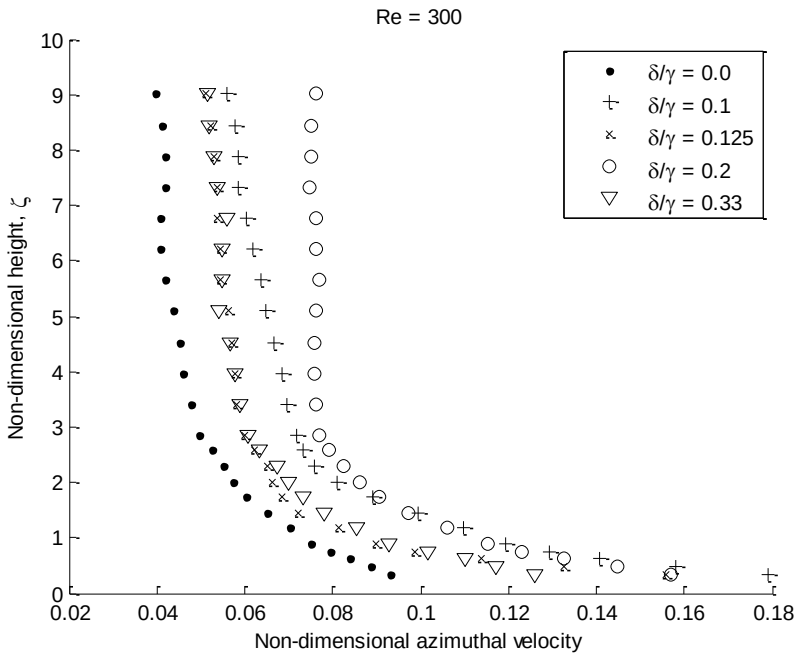

Figure 6.6 - Azimuthal velocity profiles for disks of increasing roughness at Re = 300, Ω = 7.85 rad/s.

For the azimuthal velocity profile, a similar effect is seen whereby the flow velocity increases as roughness is introduced. Figure 6.6 shows this relationship for a Reynolds number of 300. The theoretical profiles in Figure 3.4 for the azimuthal flow component predicted a thickening of the boundary-layer as roughness increased. This does seem to be apparent here as the rough profiles all experience an increase in velocity throughout the boundary-layer suggesting a thickening, were the profiles to continue upwards to higher ζ. The profiles at other radii show the same effect and so are not shown here.

While the results seen here for the azimuthal flow profiles do agree somewhat with the numerical results, they do not agree with the azimuthal profiles seen in Watanabe at al. (2007). The effect of adding the spiral grooves in Watanabe's study was to decrease the total velocity of the azimuthal profiles. This too may be an effect of the enclosure of the disk.

The experimental results for both sets of profiles help validate the ensemble averaging used to remove the changing profiles over each wavelength in the numerical calculations. It seems that any minute changes that may occur over the small distance of one wavelength are negligible over the larger length scale of the radius of the disk.

Overall, it seems that the experimental profiles compare favourably with those produced by the NAG routine in Chapter 3.1, at least in showing the thickening of the boundary layer and the reduction of the radial wall jet. Without more conclusive experimental results performed with a more reliable calibration system, these results are the best that can be managed for now. At this stage, they do at least point towards the use of the modified velocity profiles in the stability code being the right path to take, and lead the way to be able to compare the stability results of both studies.

6.2 Velocity fields

Rather than looking solely at the steady basic flow at discrete Reynolds numbers, it is more useful to see how the whole flow looks under the influence of roughness. To do this, it is necessary to record as much of the flow as possible using the hot film probe. However, because the probe can only be in one location at once, the flow field needs to be built up slowly; adding regions of the flow field over time, using the assumption that the features of the boundary-layer that we are interested in are steady and do not change between each result. Of course, this assumption will negate any travelling waves or effects which change with time, but since in our numerical study we have only looked at stationary waves by stating

that $\omega_r = \beta$, we can continue to look solely at disturbances which do not vary temporally.

To do this the probe is positioned at one radius and a certain height, and a velocity trace is taken for one rotation of the disk, thus recording the flow field for a thin radius. The probe is then moved radially outwards, and another trace is taken, gradually building up the whole flow field at that height. The non-dimensional height of the probe above the disk was taken to be $\zeta = 1.23$ as this was close to the measured maximum of stationary vortex perturbations by Lingwood (1996). The velocity traces were taken at 31 radial intervals of 5mm across most of the 195mm radius of the disk. This produced results across the whole spectrum of Reynolds numbers, from laminar flow to turbulence, ensuring that the transition region was captured. As in previous studies, (Jarre et al. 1996b; Lingwood 1996; Colley et al. 1999) rather than only taking the results for a single rotation of the disk, many rotations were collected and then ensemble averaged to create one velocity trace. This ensemble averaging reduces the signal to noise ratio and further removes any contributions from travelling waves in the time series, although it clarifies any stationary waves and makes them easier to pick out. For this study it was decided that 50 rotations should be taken at each radius and averaged, thus increasing the signal to noise ratio by a factor of $\sqrt{50}$ (MacDonough & Whalen 1995). To ensure that the features of each individual trace are added at the right point, the optical trigger mechanism mentioned in Chapter 5.1 causes the anemometer to acquire data at the exact same point at each rotation. This means that stationary features in the flow at specific azimuthal locations are not removed by the averaging.

Flow fields were created for all 12 rough disks as well as the smooth glass disk at a selection of 4 different rotation velocities. The reason for this was to see if the roughness effect changes as the boundary-layer decreases or increases in thickness. When the disk velocity is increased, the non-dimensional roughness height which is scaled to the boundary-layer thickness decreases accordingly (while the roughness ratio stays the same). So the disks are spun at 4 angular velocities to gauge the effect on the flow. Spinning the disks at different velocities also has the benefit of changing both the noise levels and Reynolds number range on the disks. For example, a disk rotating at the slowest speed, 6.28 rad/s will have low noise levels and hence flow structures will be easier to pick out, but that same disk will have a maximum achievable Reynolds number of 488 at the edge, and therefore may not capture the entire transition region. The fastest spun disks, at 10.99 rad/s will capture the entire region, but will have much greater levels of noise.

Because of the difficulties in ensuring that the probes were kept calibrated for long enough periods of time to record the entire flow field, and because of problems with the accuracy of the calibrated probes, it was decided to run the these experiments without calibrating the probes. This is the same approach taken by Jarre et al. (1996b) as they were only interested in the relative growths of the Fourier modes and not the exact velocity of the flow. From here on, we will only be presenting our results in terms of fluctuating voltage rather than velocity, as this will still display all the perturbations and flow structures, but without the necessity for lengthy calibration between runs.

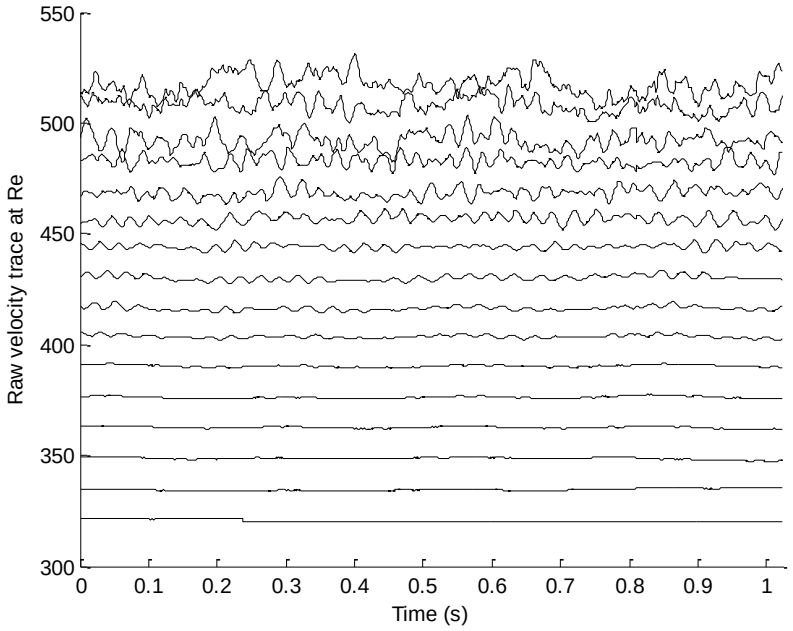

Figure 6.7 - Peak normalised, ensemble averaged traces of raw voltage signals. Each trace represents the azimuthal velocity component at that Reynolds number. Traces were taken on the smooth glass disk at a height of $\zeta = 1.23$ and $\Omega = 7.85$ rad/s.

Figure 6.7 shows the velocity field for the smooth disk. The data shows the flow passing from laminar with no disturbances at Re=321, to individual vortices appearing and multiplying as they move downstream with increasing Reynolds number. The stationary vortices (travelling vortices have been removed by the ensemble averaging process) are regularly spaced and are relatively smooth by Re=428, and there are approximately 27-28 of them. By tracking individual vortices at successive radii and using the time axis to calculate their angular position using trigonometry, the angle the spiral makes with the azimuthal axis can be calculated. For this disk, the wave angle is approximately 12°, which puts it very close to the 13°-14° seen in previous investigations.

Beyond Re=460 the vortices start to become less regular and begin to break down, while by Re=500 the flow has lost its periodicity and is well on the way to becoming

turbulent. In the above plot, the peak normalised traces have been amplified by a small factor to make the individual vortices easier to see, so the size of the fluctuation peaks between different velocity field plots cannot be directly compared.

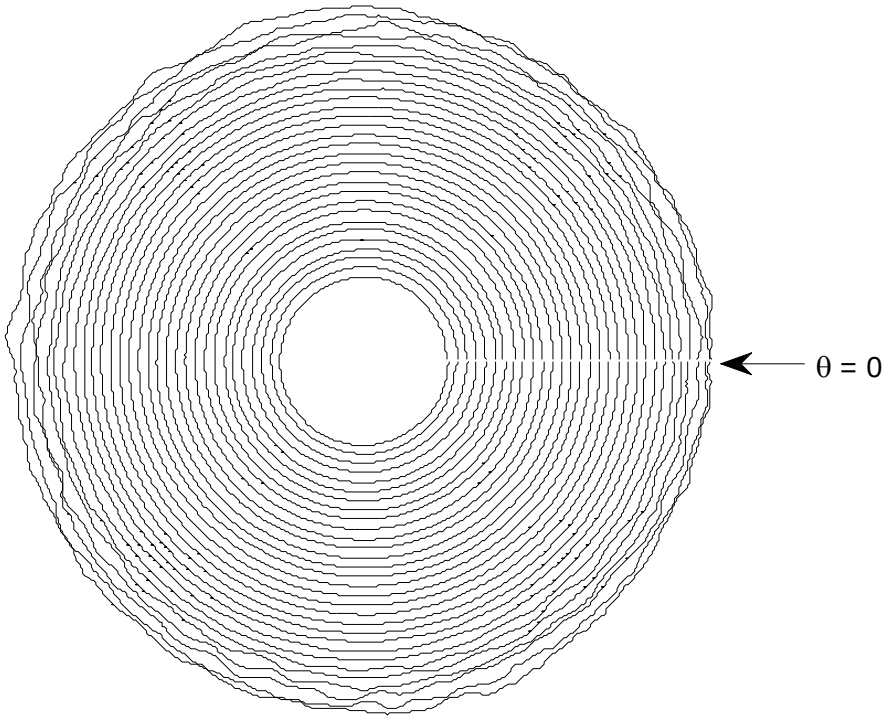

Figure 6.8 - Polar plot of fluctuation data from Figure 6.7.

To get a better idea of how the velocity fluctuations look in relation to their position over the disk surface, one can plot them on a polar coordinate system, setting t = 0 as $\theta = 0$ and positioning each trace at its appropriate radius on the disk. The resultant polar plot shown as Figure 6.8 gives us a good impression of the regions of the disk, although in this case it is harder to pick out the individual vortices around the disk.

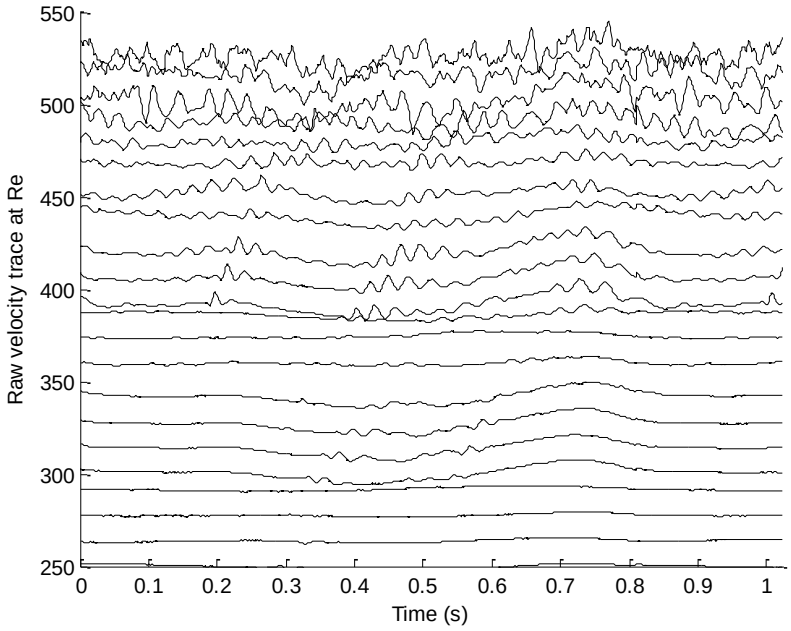

Figure 6.9 - Peak normalised, ensemble averaged traces of raw voltage signals. Each trace represents the azimuthal velocity component at that Reynolds number. Traces were taken on a $\delta/\gamma = 0.1$ rough disk at a height of $\zeta = 1.23$ and $\Omega = 7.85$ rad/s.

Figure 6.9 shows a similar velocity trace plot for a rough disk example of ratio 0.1. Once again the development of the spiral vortices can be seen from their genesis at certain radii on the disk. As they multiply and grow, they eventually transition to turbulence until all periodicity is lost near the edge of the disk. Although the stationary vortices are visible in the above plot, it becomes more difficult to count exactly how many there are with increasing levels of noise, and so to aid in counting the exact vortex number, the frequency content of the data was extracted in Chapter 6.3.

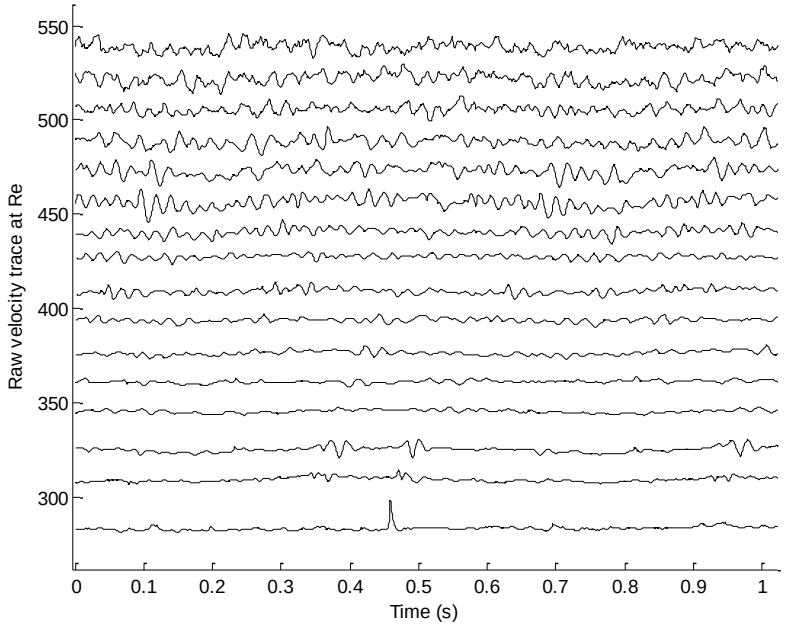

Figure 6.10 - Peak normalised, ensemble averaged traces of raw voltage signals. Each trace represents the azimuthal velocity component at that Reynolds number. Traces were taken on a $\delta/\gamma = 0.3$ rough disk at a height of $\zeta = 1.23$ and $\Omega = 10.99$ rad/s.

Figure 6.10 shows the flow field for a disk with a roughness ratio of 0.3. The flow field looks similar to those at lower roughness levels, aside from perhaps a larger amount of noise which comes from rotating at higher rate. There does not appear to be any discernable effect of the roughness on the velocity flow fields. The vortices appear to form and spread in the same manner seen by Wilkinson and Malik (1985) on a smooth, clean disk. Indeed, one of the most surprising similarities between that study and this one is the manner in which the vortices are initially formed. For the smooth, clean disk in Wilkinson and Malik, the vortices first appear as a single peak in the velocity trace at low Re. One might expect the addition of the azimuthal roughness in this study to affect the way in which this initial vortex formation occurs, but the single peak appearing at Re=260 in Figure 6.10 appears to show the vortices being formed in the usual way, i.e. caused by small dust motes or debris on the disk surface which then spreads out into multiple vortices. This shows

that while the roughness may or may not affect the instability modes or vortex numbers, it appears to have no effect on the manner in which the spiral vortices are formed; the vortices still appear to be excited by a single discrete roughness element rather than the azimuthal grooves.

6.2.1 Wave angle

For the case presented above it is also possible to calculate the angle the spiral vortices make by following a particular spiral peak as it travels outwards. The angle the vortices make with the radial axis can be calculated using trigonometry to be between 13° and 14°, which is similar to what was seen for the smooth disk case. The accuracy for these angles is based on the distance in time between stationary vortices at different radii, and the radial distance between each velocity trace, which is only accurate to 0.5mm. Thus the total accuracy of the calculated angle is only precise to ±1°. In addition, some of the disk flow fields (particularly ones rotating at higher velocities) are simply too noisy to be able to track individual stationary vortices and calculate the wave angle.

Despite these limitations, the wave angle for the majority of disks and speeds were calculated and plotted against the roughness ratio.

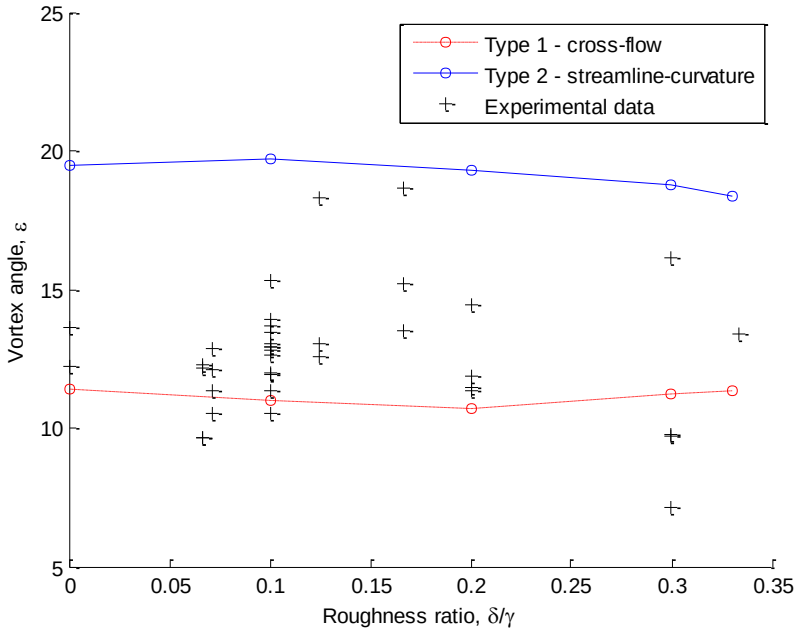

Figure 6.11 - Experimental wave angles compared against numerically derived values

From Chapter 4.4 it was seen that the increasing roughness ratio did not have a great effect on the wave angle in terms of the neutral stability curve. Neither the Type 1 nor the Type 2 lobes altered much with regards to the wave angle, although it was surmised that if there was a switch in the dominant mode, then the wave angle may also switch from the 13° associated with the Type 1, to the 19° associated with the Type 2.

Looking at Figure 6.11, it would appear to confirm the numerical result that the wave angle does not change with increasing roughness ratio. Even allowing for the imprecision of the wave angle measurement, the perceivable trend in the data is that the angle remains between 10-15° regardless of roughness. Similarly, this result shows that there is no evidence of a switch to a wave angle associated with the Type 2 instability.

6.3 Frequency fields

Due to the velocity flow fields for each disk being observationally quite similar, and because it is problematic to identify and distinguish the exact number of vortices present from the flow fields, a useful technique is to calculate the frequency content of the data and use this to work out the number of vortices at each Reynolds number. A Fast Fourier Transform is applied to each velocity trace individually before being ensemble averaged to create a frequency-amplitude plot of the flow at that Reynolds number, with only the most commonly occurring frequencies remaining after the averaging. Once again a flow field can be built up using the velocity traces at increasing radii. The Fast Fourier transform produces a plot of the most commonly occurring frequencies and their amplitude. Therefore any structures in the flow that appear periodically show up strongly in the Fourier plot and we can use this to pick out the number of vortices formed in the flow. We square the amplitude of these frequency spectra to produce the power and display it as $A(f)^2$. Knowing the power contained in the signal is useful for producing neutral stability curves in Chapter 6.5.

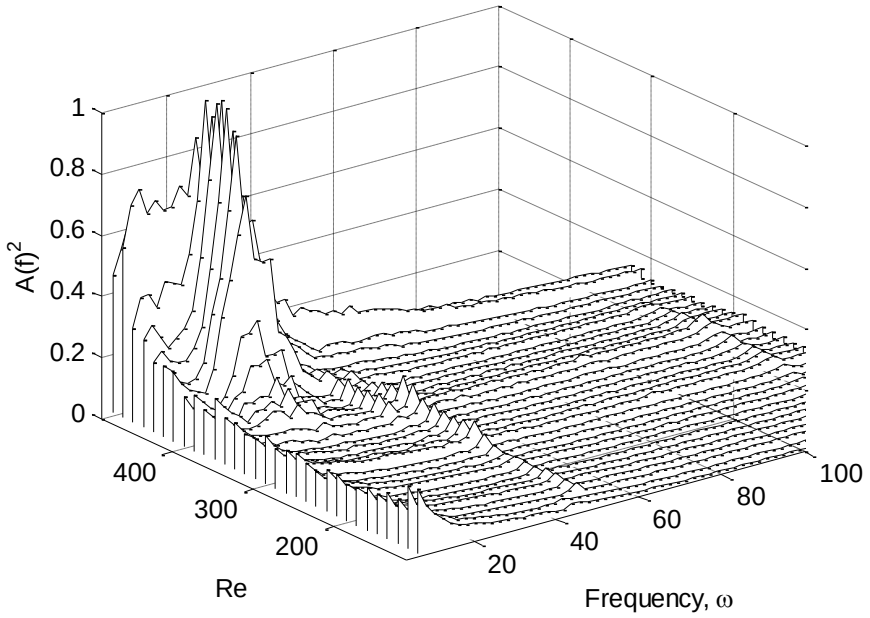

Figure 6.12 - Frequency flow field for a smooth glass disk rotating at $\Omega = 6.28$ rad/s.

Figure 6.12 shows the frequency plot for the smooth glass disk, in a similar plot to that seen in Jarre et al. (1991). Each line on the plot shows the frequencies at a certain radii, showing the evolution of the frequency content of the flow as it moves downstream to higher Reynolds numbers. The z-axis plots the normalized energy content of the flow $A(f)^2$ at that frequency. The data has been normalised against the largest value in the dataset, usually a peak in the spectra for the flow at highest Re. This normalisation ensures that small amplitude features in the laminar region of the flow are not lost. Meanwhile, the frequency f per sample has been divided by the disk rotation in hertz f_D to allow us to look at 'disturbances per disk rotation', ω rather than 'disturbances per second'. See Colley et al (1999) for further clarification of this.

The thin line of disturbed frequencies running at a frequency of $\omega = 50$ is thought to arise from a mains frequency of 50Hz being introduced through the probe

voltage rather than stemming from any part of the flow (additional subharmonic peaks at 100Hz and 150Hz help confirm this). It was thought that this aberration could be caused by vibrations from the motor, but tests found that this was not the case. The amplitude of these frequencies is small and does not affect the flow results.

The frequency field otherwise shows a packet of disturbed frequencies which begin at approximately Re ≈ 340 before growing in energy towards the edge of the disk. This peak is centred on a value of $\omega = 28$ which suggests there are approximately 28 vortices spread out azimuthally around the disk at that point. This compares favourably to all other experimental reports which put the number of spiral vortices at between 28 and 32 (Wilkinson & Malik 1985). Similarly, numerical studies place the point of initial cross-flow instability at Re ≈ 285 (Malik 1986), so a disturbance appearing a small distance downstream at Re ≈ 340 satisfies this also.

The smaller peak running at a low frequency at all radii are disturbances which arise from the imbalance of the disk causing a peak at $\omega = 1$ and can be disregarded as they have no consequence to the flow structure.

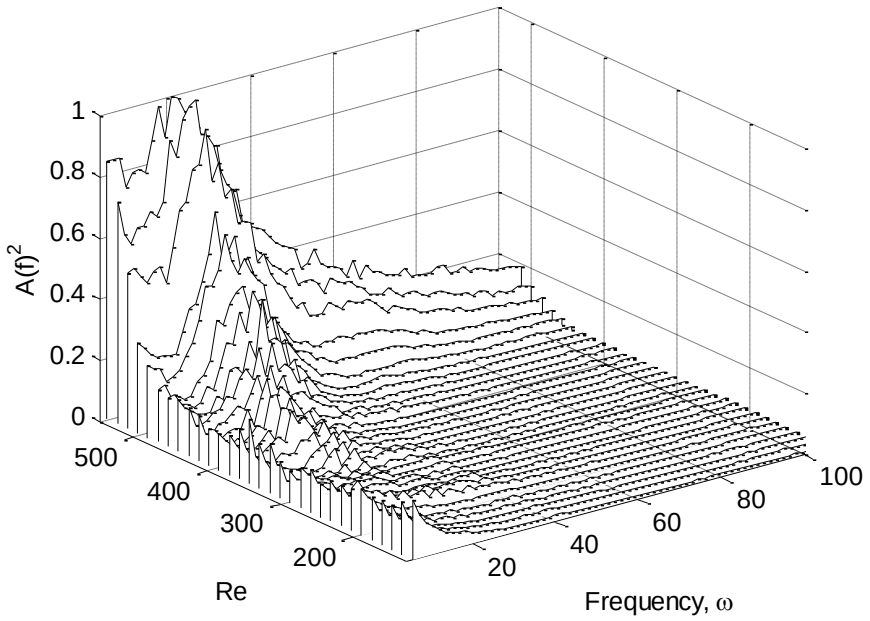

Figure 6.13 - Frequency flow field for a $\delta/\gamma = 0.1$ disk rotating at $\Omega = 7.85$ rad/s.

The comparable frequency flow field for a rough disk is shown in Figure 6.13. The figure displays similar characteristics to the smooth case, including a large peak representing the spiral vortices in the transition zone. The peak for this disk is centred on $\omega = 25$ which amounts to a drop in the number of vortices present, compared to the smooth case. Also visible in this plot is a sharp increase in the broadband frequencies that signify the onset of turbulence in the flow past a Reynolds number of approximately 500. While the 3D plot is an acceptable way of showing the packets of frequency content in the flow field, it is not suited to gauging the exact number of vortices present or the exact transition points between regions of laminar flow, instability and turbulence. Another and perhaps better way of visualising the data is in a contour plot.

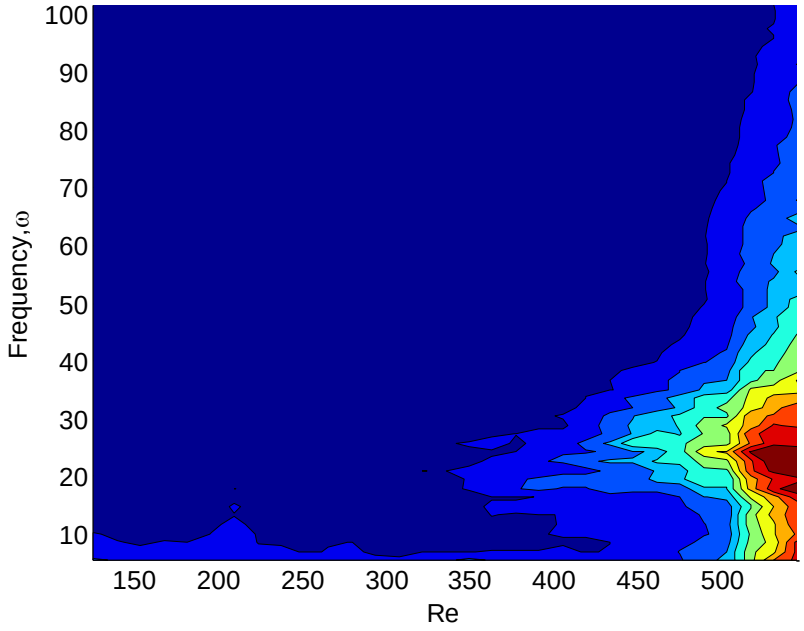

Figure 6.14 - Results from Figure 6.13 shown as a normalised contour plot.

The normalised contour plot shown in Figure 6.14 visualises the vortex peak more clearly than in the 3D plot. It plots the power of the frequency spectra in contours with graduations of 0.1 from 0 to 1. From this figure it is easier to see the vortex peak centred on $\omega = 25$, as well as the points where the instability first begins (Re ≈ 335) and also the approximate region where the flow become turbulent. As the flow breaks down from discrete spiral vortices, the Fourier content of the boundary-layer becomes a much broader spectrum of frequencies, in this case occurring around Re = 500 (more thorough means of determining the turbulent transition point are discussed in Chapter 6.7).

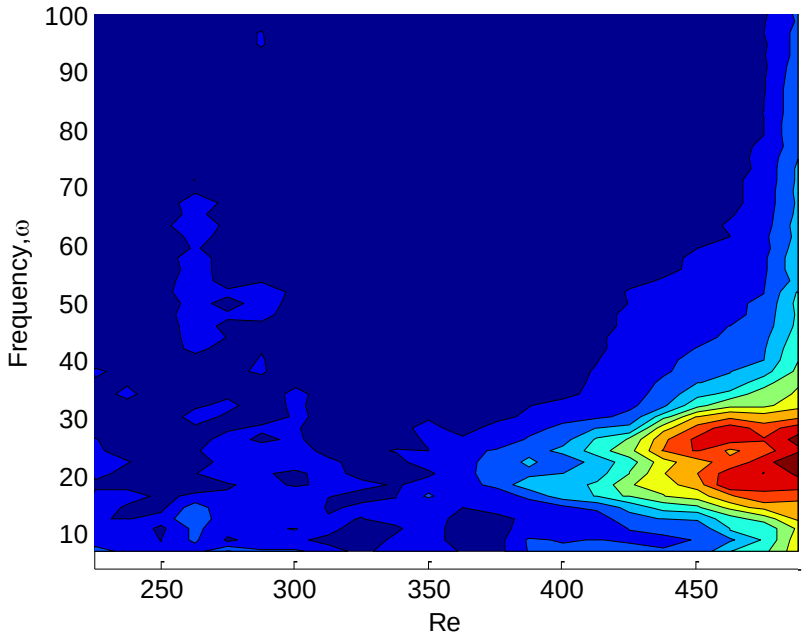

Figure 6.15 - Contour flow field for a $\delta/\gamma = 0.2$ disk rotating at $\Omega = 6.28$ rad/s.

If we increase the roughness further still, we can see the peak shift further to a lower number of vortices. The main peak in Figure 6.15 is centred on $\omega \approx 22$. Interestingly, for higher Reynolds numbers just before the transition to turbulence, the frequency packet for this disk seems to contain two separate peaks in this plot; one at $\omega \approx 28$ and a larger one at $\omega \approx 22$. These arise from the range of unstable wavenumber forming a superposition pattern which results in two stronger wavenumbers appearing in the frequency content rather than one.

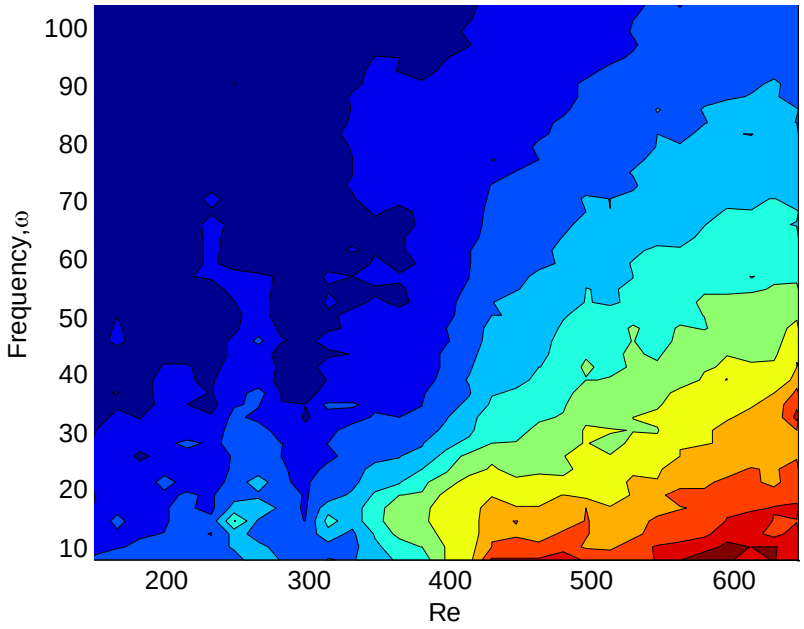

Figure 6.16 - Contour flow field for a $\delta/\gamma = 0.33$ disk rotating at $\Omega = 10.99$ rad/s.

Keeping the roughness level at $\delta/\gamma = 0.33$ and increasing the rotation speed to $\Omega = 10.99$ rad/s gives the flow seen in Figure 6.16. The increase in rotation speed has amplified the amount of noise present in the flow field, which is perhaps to be expected, yet the spiral vortex peak is still visible, something which would not be possible in the 3D plot or the velocity trace. The vortex peak for this high level of roughness is centred on $\omega \approx 16$, roughly half the vortices compared to the smooth glass case.

6.4 Vortex number

We can record the locations of the vortex peaks for all of the disks used in the study (rounded to the nearest whole vortex number), at four different rotation speeds, and plot them against roughness ratio to perceive the effect of increasing roughness ratio on vortex number.

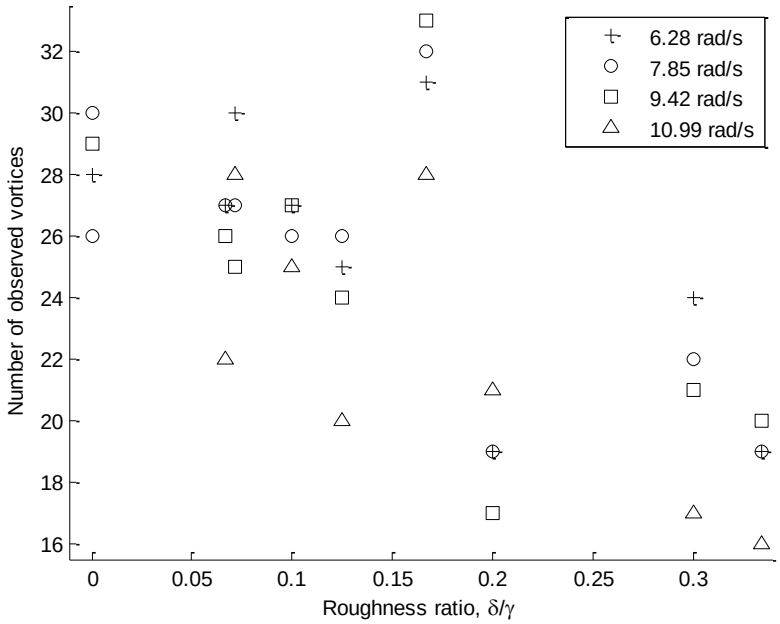

Figure 6.17 - Vortex numbers taken from frequency contour plots

In Figure 6.17, the data for only one of the $\delta/\gamma = 0.1$ disks has been displayed rather than all five to improve the clarity of the image, but otherwise all disk data is displayed at four different speeds. The plot shows there to be a general trend of decreasing vortex number with increasing roughness ratio. For each disk running at four different speeds, it seems that the faster the disk rotation, the fewer azimuthal vortices present. For almost every disk the rotation rate of 10.99 rad/s produces the lowest number of vortices, with more vortices appearing as rotation rate decreases. This result seems counter-intuitive, but is discussed later.

The $\delta/\gamma = 0.167$ disk appears to show a discrepancy whereby it does not follow the trend of having a low number of vortices. To explain this, one needs to look at the properties of the disk in Table 5.1. Although it does have a high roughness ratio, the actual roughness depth of the grooves for this disk is of the shallowest type,

only 0.1mm. It is thought that because the grooves are shallow, and close together, the surface of the disk acts as smooth rather than rough.

To test this theory, the data of Figure 6.17 can be re-plotted and rather than plotting the vortex numbers against roughness ratio, they are plotted against non-dimensional roughness. In other words, we ignore the distance between the grooves and simply plot the number of vortices against the groove depths scaled by the boundary-layer thickness to make them non-dimensional.

$$\text{Non-dimensional roughness height} = \delta\sqrt{\frac{\Omega}{\nu}} \qquad 6.1$$

The non-dimensional roughness height helps explain why the number of vortices decreases as the rotational velocity increases. While the physical roughness depth may stay the same, the boundary-layer becomes thinner as the disk is spun faster, and thus the non-dimensional depth of the roughness grooves becomes larger in comparison to the height of the boundary-layer.

Because the boundary-layer thickness is scaled by the rotation speed of the disk (see Equation 6.1), the data is now displayed independent of rotation speed, although the markers used to distinguish these speeds are still shown for reference.

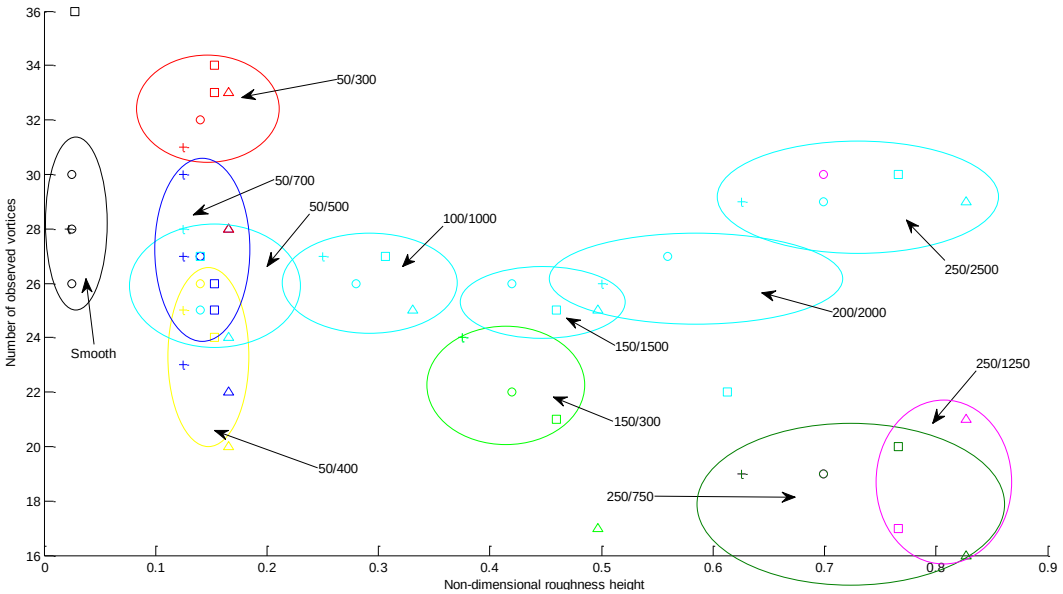

Figure 6.18 - Vortex data from Figure 6.17 plotted against non-dimensional roughness height. Disk speed markers are the same as in Figure 6.17 and arrows indicate the delta/gamma of the roughness pattern used in microns. All the $\delta/\gamma = 0.1$ disk data has been plotted this time.

Thus in Figure 6.18 we observe that the discrepancy of the $\delta/\gamma = 0.167$ (50µm/300µm) disk is not as noticeable, as the fact that it has such a shallow roughness places the vortex data much closer to the smooth case. However, the disk still does not behave in a similar manner to the other rough disks as will be discussed below.

While all the data points have been included in Figure 6.18 for completeness, it is perhaps easier to visualise as shown in Figure 6.19. For this plot, the number of vortices seen at the four different speeds for each disk has been averaged and plotted against the average non-dimensional roughness height for those results, essentially reducing each cluster of data to just one point.

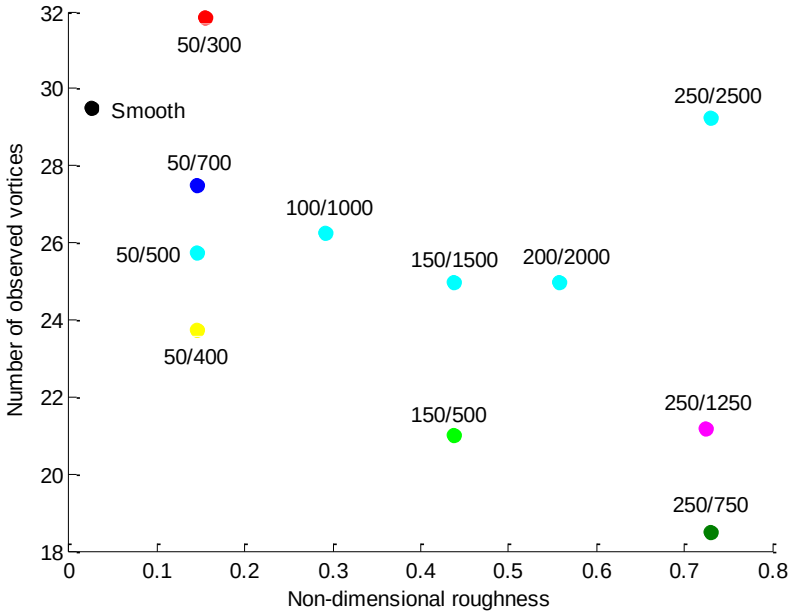

Figure 6.19 - Data from Figure 6.18 after averaging with respect to the number of vortices and the non-dimensional roughness.

It is clear from Figure 6.19 that in the case of roughness, the number of vortices is dependent on more than one variable. Simply increasing the non-dimensional roughness depth does not necessarily decrease the number of vortices, as can be seen by looking at the results for the $\delta/\gamma = 0.1$ disks (cyan markers). Increasing the roughness height in this case causes no discernable difference in the number of vortices, other than for the 250µm/2500µm disk. It seems that the reason for this is that the roughness ratio also needs to be increased for there to be an effect, i.e. for results which have the same or similar roughness depth (δ); a decrease in vortices is only seen when there is also a drop in roughness width (γ).

This is where the $\delta/\gamma = 0.167$ disk proves to be a disparity again however. For the data between 0.1 and 0.2, which have a similar non-dimensional roughness, there is a drop in vortex number with a decrease in roughness width, and yet the 50µm/300µm disk does not fit this trend, as it should be below the 50µm/400µm

disk but is instead higher up the vortices axis. This suggests again that perhaps the roughness grooves are too close together and act as smooth for this disk.

This noticeable effect of increasing the distance between the grooves can possible be explained by referring to a paper by Floryan and Asai (2011) in which the linear stability characteristics of flow over distributed roughness was calculated for channel flow. They discovered that as one increases the distance between the roughness grooves or ridges, the roughness transitions from acting like a distributed roughness to becoming more like isolated roughness elements, and results in a stabilising effect on the streamwise vortices. They noted that this transition phenomenon was enacted a lot faster in roughness shaped as 'trenches' or grooves such as in the study presented here, than rough 'ridges'.

It could be that in Figure 6.18 for roughness patterns which have equal roughness heights, the distance between the grooves reacts in much the same way. As the groove separation increases, the roughness elements act as isolated roughness elements and stabilise the stationary vortices, ensuring that the number of spiral vortices remains high. This can be seen most effectively for the seemingly anomalous 250µm/2500µm disk which has a large groove separation distance, and for which the number of vortices remains equal to the smooth case. For patterns where the grooves are closer together, any disturbances caused by the roughness are coupled and the roughness behaves as a single system. The effect of this more unstable distributed roughness system appears to be a decrease in the number of vortices which could be due to the roughness disrupting their formation.

It is noted by Floryan and Asai that roughness elements spaced further apart are more likely to produce travelling waves, structures not considered in this study. It would be interesting to look at travelling waves in a future investigation to see if they did indeed increase as the distance between the grooves increased.

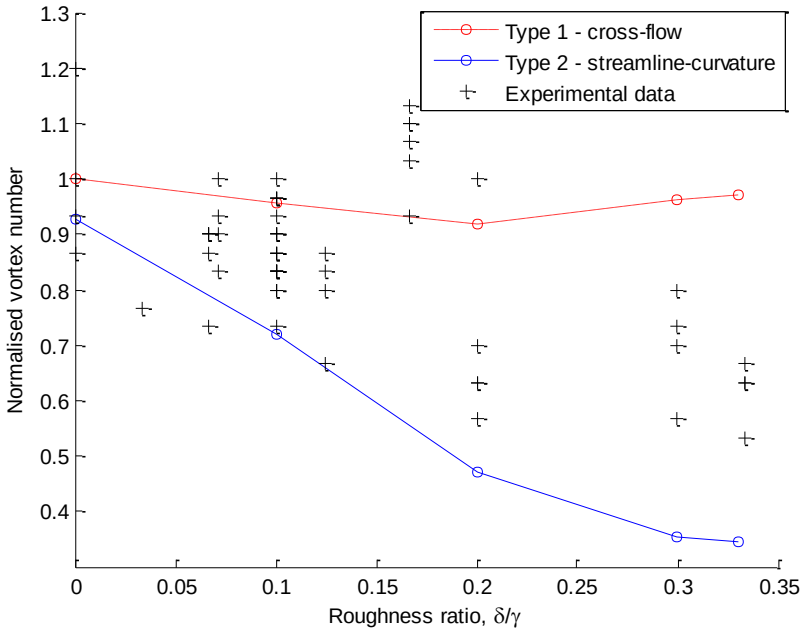

Figure 6.20 - Observed vortex number and numerical wavenumbers for both modes at various roughness ratios. All data has been normalised with the smooth case values.

In Chapter 4.3 the initial vortex number was plotted as predicted by the numerical code. However, comparing these values for the vortex number at the point of initial instability with the above experimental vortex numbers would be inconclusive, since the latter have developed as they moved downstream. The number of vortices at the onset of instability is usually lower than when the vortices are fully developed. For example, Wilkinson and Malik (1985) counted the number of vortices as they evolved downstream, showing that they start off with a few disturbances triggered by debris on the disk before rapidly increasing to a value of

around 22 vortices at the point of initial instability, before slowly developing into the familiar 30 vortices.

To compare the experimental and theoretical vortex numbers, it is instead easier to normalise both sets of data by dividing by the smooth case value. The numerical initial vortex numbers are divided by the value of the Type 1 lobe at $\delta/\gamma = 0$, i.e. 22, while the experimental data points are divided by the average number of vortices observed over the smooth glass disk, 30. Thus all data has been normalised by the equivalent value for the smooth disk. The result is the plot in Figure 6.20 which shows the expected slope of the change in vortex number predicted by the numerical neutral curves, and the corresponding slope of the experimental results as the roughness ratio is increased.

In Chapter 4.3 it was surmised that by counting the number of vortices seen on the experimental disks, one may be able to observe the point at which the Type 2 instability overcame the dominant Type 1 cross-flow instability. Looking to the data presented in Figure 6.20, it can be seen that while most of the data points fall between the two predicted slopes (aside from the anomalous $\delta/\gamma = 0.16$ rough disk) there is no obviously visible switch at any point. Instead, the normalised number of vortices appears to follow a steeper slope from the start. Clearly the roughness is having an effect on the vortex number, but it is unclear which instability mechanism is causing this effect. Although the number of vortices appears to follow the steeper slope of the Type 2 mode, it seems unlikely that the growth of the streamline-curvature mode is causing this effect, based on the size of the Type 2 growth rates seen in Chapter 4.2. The growth rates simply are not large

enough at low roughness ratios to have such an effect on the formation of the vortices. However, the largest change in the growth rates occurred not in the Type 2, but the reduction of the Type 1 mode (see Figure 4.2). From the offset of small roughness ratios, the growth rate of the Type 1 instability began to shrink noticeably. It seems likely that it is this reduction that is causing the deleterious effect on the vortex numbers; as the growth rate of the Type 1 instability falls, fewer spiral vortices are formed.

6.5 Neutral curves

Similar to the numerical data, an important tool in visualising the stability of a flow is to plot the curve of neutral stability. This allows us to see where in the flow the instabilities are likely to occur and compare the differing stability of various flows. It is possible to put together a curve of neutral stability using the energy levels taken from the Fourier transforms. The energy in the signal is proportional to the square of the amplitude of the frequency spectrum, and so by squaring the modulus of the amplitude we can see an approximation of the energy in the signal at each Reynolds number. As we move either upstream or downstream, the response of the energy in the flow can tell us what a disturbance in the boundary-layer is likely to do should an instability form. For example, if there is a fall in energy, a disturbance is likely to be damped and die away, whereas if the energy increases as we move downstream, the instability will more likely grow. Thus the point where the energy in the flow reaches a minimum is a point where a disturbance is neither going to decay nor grow, a point of neutral stability.

This method has been used in previous studies, including by Jarre et al. (1996b) to plot the neutral curve for the smooth disk and compare with theory and also by Colley et al. (1999) to produce the neutral curve for the compliant disk case.

For differing values of the frequency ω, the power of the frequency spectrum is plotted at each Reynolds number, to give a sense of how the energy in the flow changes as it moves downstream. Then, at each ω, the point of minimum energy can be found by applying a curve of best fit to the energy data. The location of this point of minimum energy is found for a range of frequencies and plotted to give the neutral stability curve for that disk.

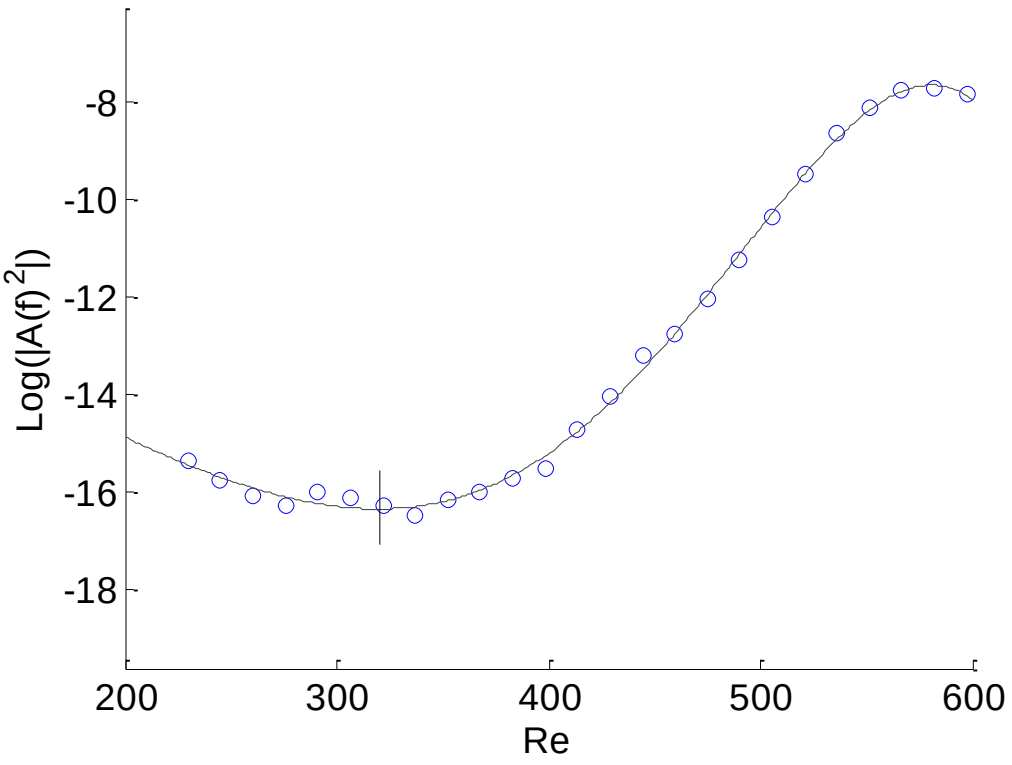

Figure 6.21 - Amplification diagram for the frequency of 16 Hz for a rough disk of ratio 0.1 rotating at 9.42 rad/s. Data has been smoothed with a 3 point moving average filter. Vertical line shows the point of minimum energy. Interpolation curve (solid line) is a fifth degree polynomial.

Figure 6.21 shows an example amplification diagram for a frequency of 16 Hz taken on a disk of roughness $\delta/\gamma = 0.1$. The vertical axis is plotted on a logarithmic scale for ease of viewing. The overall shape of the amplification curve is of an initially slight decrease in the energy in the flow, reaching a minimum, which is indicated by the vertical line. A curve of best fit has been added to aid in finding the minima. After this point of minimum energy, the instability and fluctuations in the system causes a sharp increase in the energy contained in the flow, leading up to saturation at high Reynolds numbers, indicating nonlinear behaviour and the onset of turbulence. The position of the minima can be recorded along with the minima at the whole range of frequencies and plotted together as in Figure 6.22.

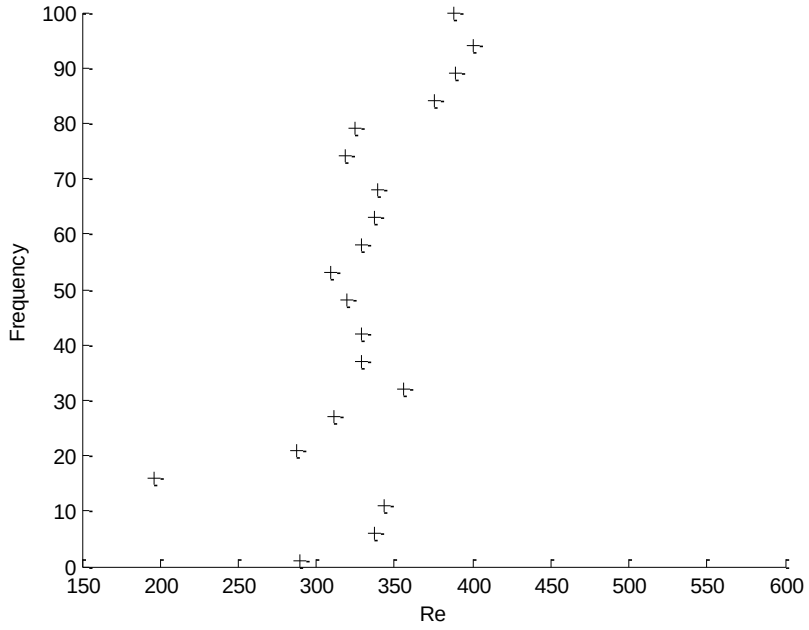

Figure 6.22 - Experimental neutral curve for $\delta/\gamma = 0.1$ disk rotating at 9.42 rad/s

The figure shows a front of neutral instability centred mainly between Re=300 and Re=400, with an apparent peak around a frequency of ω≈20. This appears

reasonable, since the initial vortex peak taken from the contour plot for this disk was centred on 20, at a Reynolds number of Re=380.

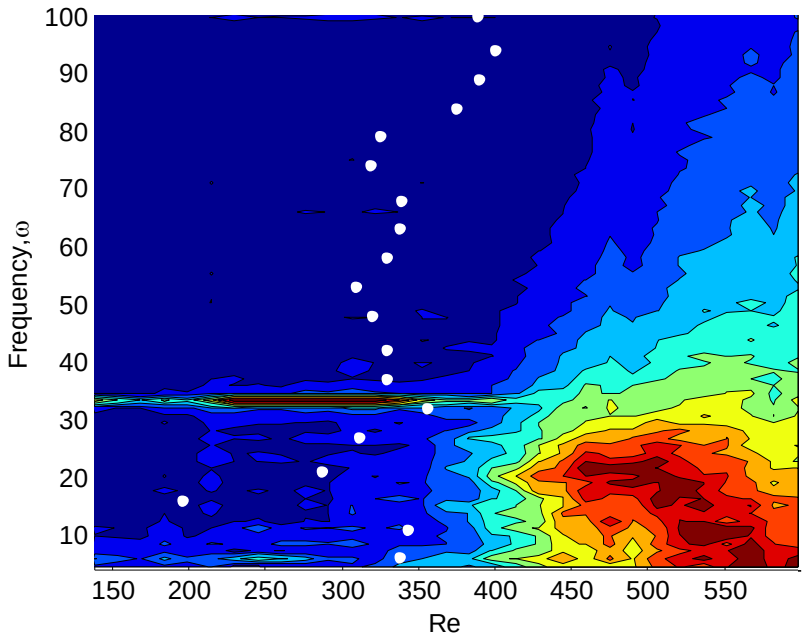

Figure 6.23 - Neutral stability curve superimposed over frequency contour map for $\delta/\gamma = 0.1$ disk rotating at 9.42 rad/s.

We can superimpose the neutral curve on top of the frequency contour map (see Chapter 6.3) for the same disk to see how they compare. As mentioned before, the solid black line centred on ω=33.3 arises from an electrical fault causing mains 50Hz voltage to appear in the probe data and can be ignored (the disk in this case is rotating at 1.5 revolutions a second which shifts the fault downwards by a factor of 1.5). Aside from this, there is a clear peak in the neutral curve matching the central peak on the contour plot. The points of neutral stability (and therefore regions of initial instability) occur further upstream than the visible effect on the contour plot which is due to low levels of disturbance not being picked up by the contour map. Other than this, the fronts of both appear to match up qualitatively. This helps validate both the contour maps and the method for obtaining the neutral curves.

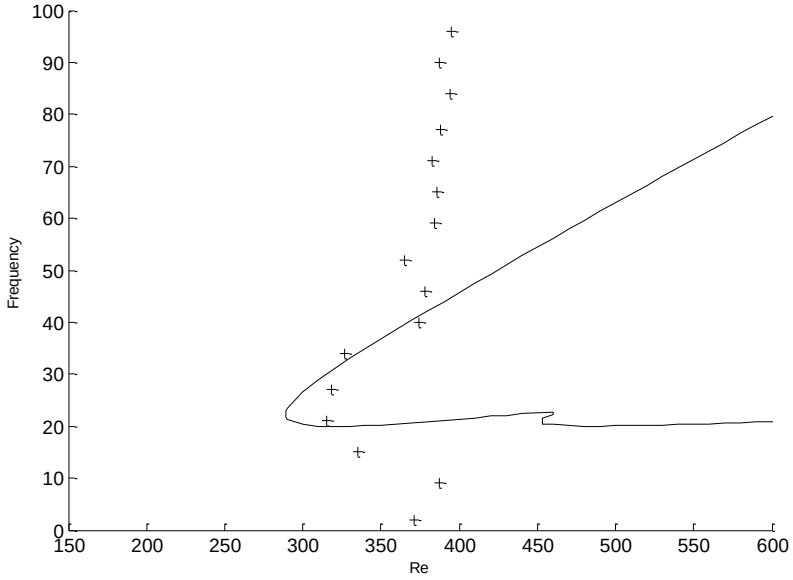

Figure 6.24 - Neutral curves for (-) $\delta = 0$, $\gamma = 1$ surface profile and (+) smooth disk rotating at $\Omega = 7.85$ rad/s.

Figure 6.24 shows the experimental neutral curve taken from the smooth glass disk positioned over the theoretical smooth curve created in Figure 4.3. Comparing the experimental neutral curves to the numerically computed ones, we notice that at as we do not get the curve dropping away at high frequencies in the experimental curves. Instead it continues upwards resulting in a much shallower, almost flat, curve. This is most likely due to nonlinear effects in the flow, i.e. higher harmonic frequencies which are contained within the flow which are not found in the linear numerical neutral curve. Similarly at low frequencies, the experimental data points are affected by the large peak found on all the disks at $\omega = 1$ caused by the imbalance of the disk, so we do not find as large a drop-off as one would expect here. Other than these discrepancies, the agreement for the smooth case is acceptable, with a lobe appearing at the frequency and Reynolds number predicted by the numerical code. This confirmation for the smooth case is comparable to the results seen by Jarre et al. (1996b) and Colley et al. (1999) .

We can also overlay the frequency field on top of the neutral curve to see how well the lobes of the curve line up with the peaks associated with the spiral vortices.

This plot in Figure 6.25 helps show the reason why the experimental neutral curves do not tend to high Reynolds numbers at high frequencies. The peak of the experimental curve appears to be falling way at the same rate as the numerical curve (between ω = 30 and 50) before a second, smaller peak in the frequency contour plot appears at ω = 55 which serves to divert the neutral curve into the shallower trajectory. This second peak occurs at approximately twice the frequency of the main vortex peak and is therefore most likely a superharmonic of the fundamental mode.

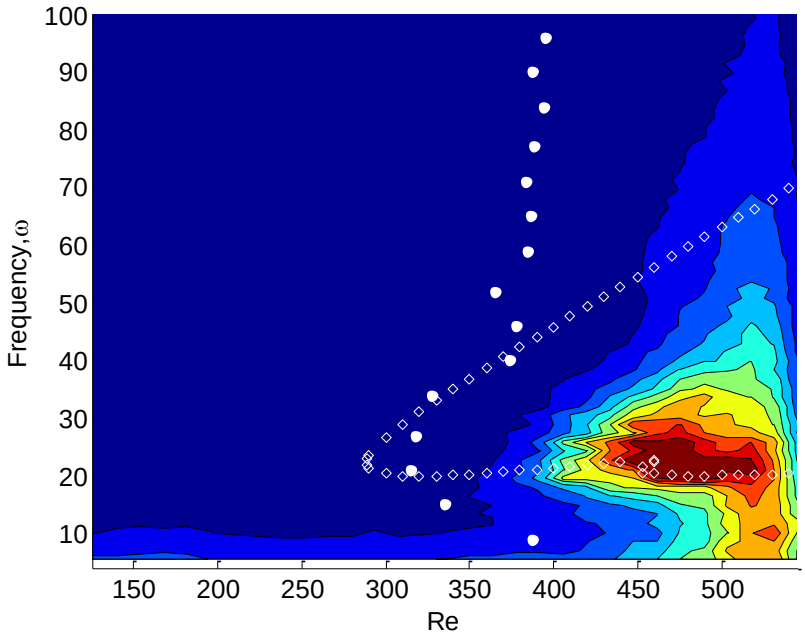

Figure 6.25 - Smooth disk neutral curves shown in Figure 6.24 with overlaid frequency plot. (○) shows the experimental curve, (◊) shows the numerical curve.

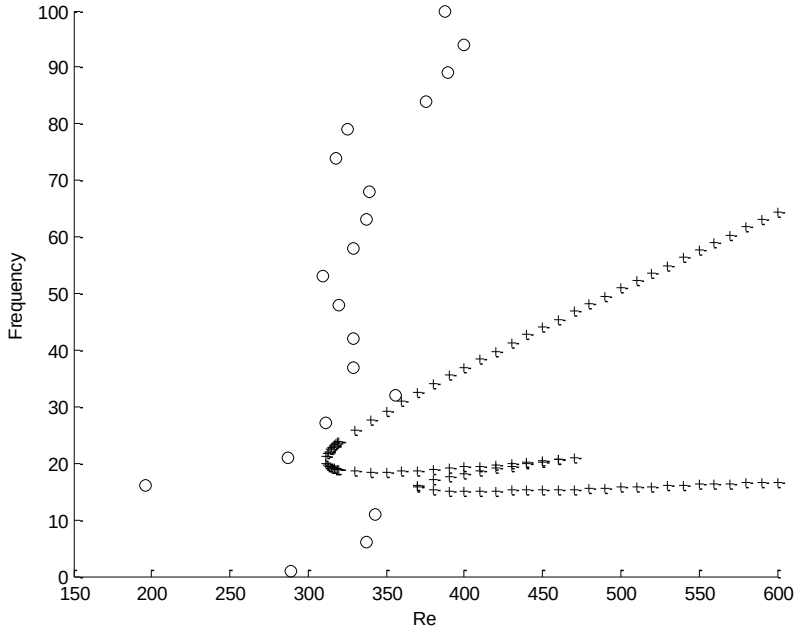

Figure 6.26 - Neutral curves for (-) δ=0.1, γ=1 surface profile and (+) $\delta/\gamma = 0.1$ disk rotating at Ω = 9.42 rad/s.

Figure 6.26 shows the neutral curve for a $\delta/\gamma = 0.1$ disk and its corresponding numerically derived curve. Again there is an agreement between the positioning of the instability lobe and the experimental data at low frequencies. While there is no visible stabilisation of the neutral curve, the frequency of the main lobe of the experimental data does appear to have shifted down slightly in comparison to the smooth curve, something that was predicted in Chapter 4.1.

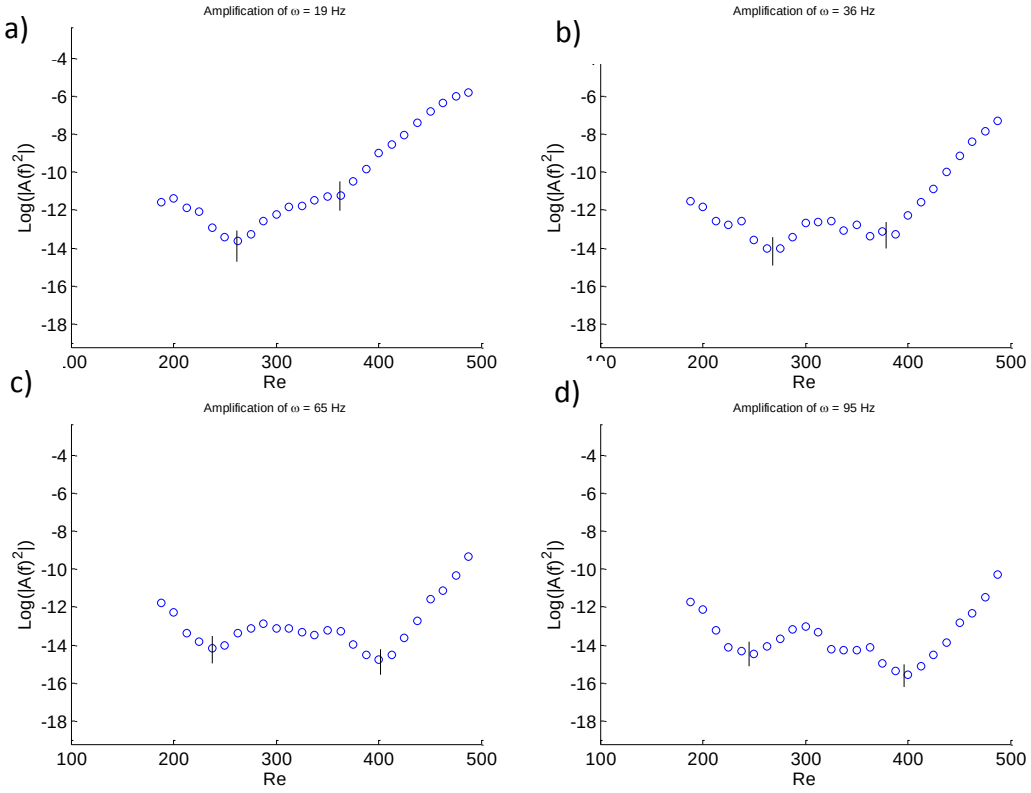

Figure 6.27 - Amplification curves for a $\delta/\gamma = 0.2$ rough disk rotating at 6.28 rad/s. Curves are taken at a) $\omega = 19$Hz b) $\omega = 36$Hz c) $\omega = 65$Hz and d) $\omega = 95$Hz. Curves have been smoothed with a 3-point moving average filter to aid in visualising minima.

Increasing the roughness further produces some interesting results. Figure 6.27 shows some example amplification curves from a disk with a roughness ratio of 0.2. There is a noticeable difference to these as they appear to have two points of minimum energy rather than the single point seen in Figure 6.21 or plots from other authors such as Jarre et al.(1996b) or Colley et al. (1999). This is interesting because it suggests that there may be two points of neutral stability in the flow over this particular disk.

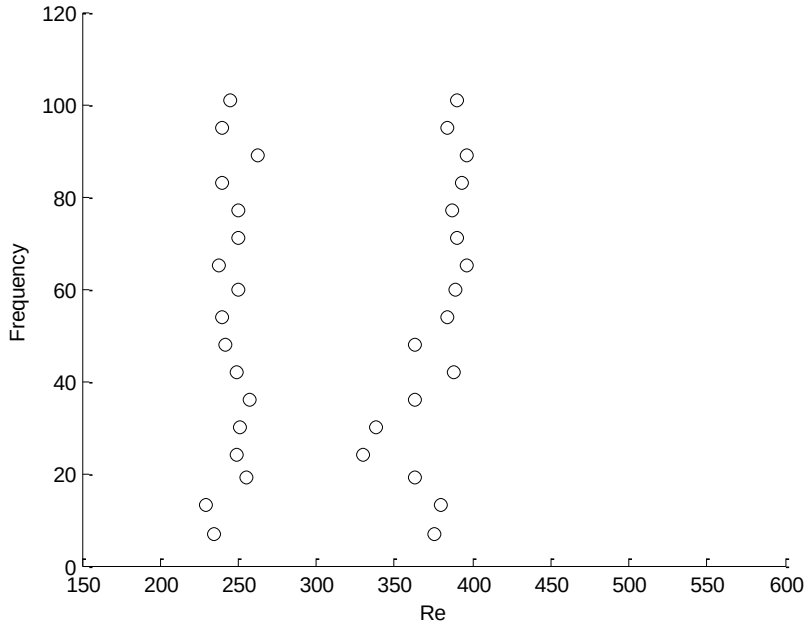

Figure 6.28 - Double neutral curves for $\delta/\gamma = 0.2$ disk rotating at 6.28 rad/s.

Due to the double minimum seen in the amplification curves, there are two neutral curves in Figure 6.28. There is a visible peak in the right hand neutral curve at a frequency of approximately 24Hz and a Re≈330, and a smaller, less visible peak in the left hand curve at 13Hz and Re≈229. These points are intriguingly close to the positions of the critical points of the numerical neutral curve for a ratio of 0.2. In Figure 4.3 the critical points of instability of the Type 1 lobe occurs at a value of $\beta = 20$ and Re = 428, while the critical point of the Type 2 lobe occurs at $\beta = 11$ and Re = 260. This would suggest that the left hand neutral curve is caused by the Type 2, streamline-curvature mode, and the right hand curve is caused in the standard way by the Type 1, cross-flow mode. This would also provide validation of the results in Chapter 4 that the rough surface causes the Type 2 mode to become dominant and influence the flow. To see how this double neutral curve manifests in the flow field, the contour plot can again be superimposed over the plot from Figure 6.28.

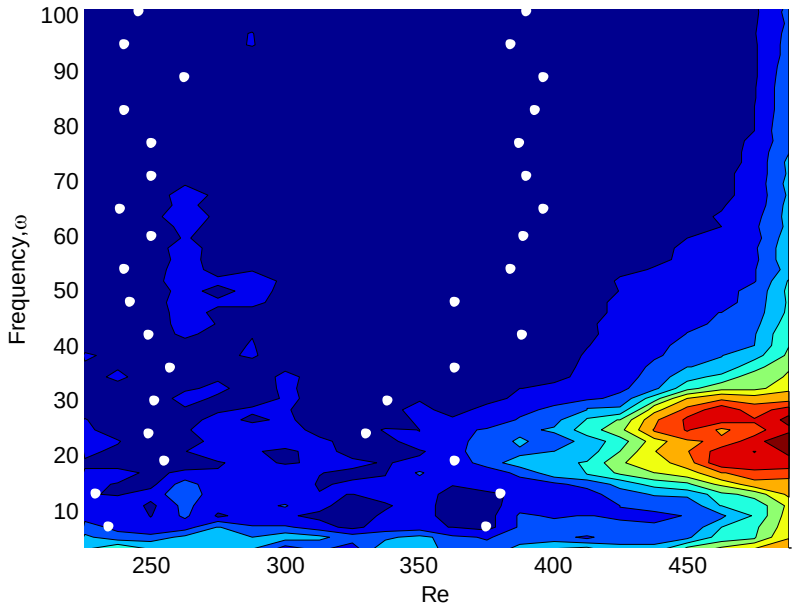

Figure 6.29 - Contour plot of a $\delta/\gamma = 0.2$ rough disk rotating at 6.28 rad/s with double neutral curve superimposed on top.

From Figure 6.29 it can be seen that the large amplitude peak centred on $\omega = 22$ matches up well with the right hand neutral curve and from this it can be concluded that the instability that caused the large peak originates from the increase in energy associated with this neutral front.

Meanwhile, there is a small amplitude peak occurring at a frequency of 13Hz and a Reynolds number of 263, along with a small burst of excited frequencies, all of which quickly die down as they move downstream. This small peak coincides both with the peak in the left hand neutral curve as well as the critical point of the Type 2 lobe on the numerical curve for a disk with a ratio of 0.2. It appears that this small peak is caused by the increase in energy associated with the left hand neutral curve and so this, coupled with its proximity to the theoretical location of the Type 2 lobe suggests that this peak is caused by the Type 2 instability, while the larger peak downstream is cause by the Type 1 instability.

It is widely agreed that the Type 1 cross-flow instability causes the spiral vortices seen on the disk. However, it could be that the Type 2 simply does not manifest itself as spiral vortices in the same way as the Type 1. As such, the unstable waves may not grow and produce a similar vortex pattern in the frequency field plot similar to the Type 1 vortices. This behaviour further confirms the finding from Chapter 6.4 where the decrease in the number of vortices is deemed to be due to a stabilising and shrinking of the Type 1 mode, rather than a switch in the mechanism by which the vortices are created. For this roughness ratio, although the Type 2 mode has a critical point further upstream, and has equal growth rates to Type 1, it does not appear to affect the number of vortices directly.

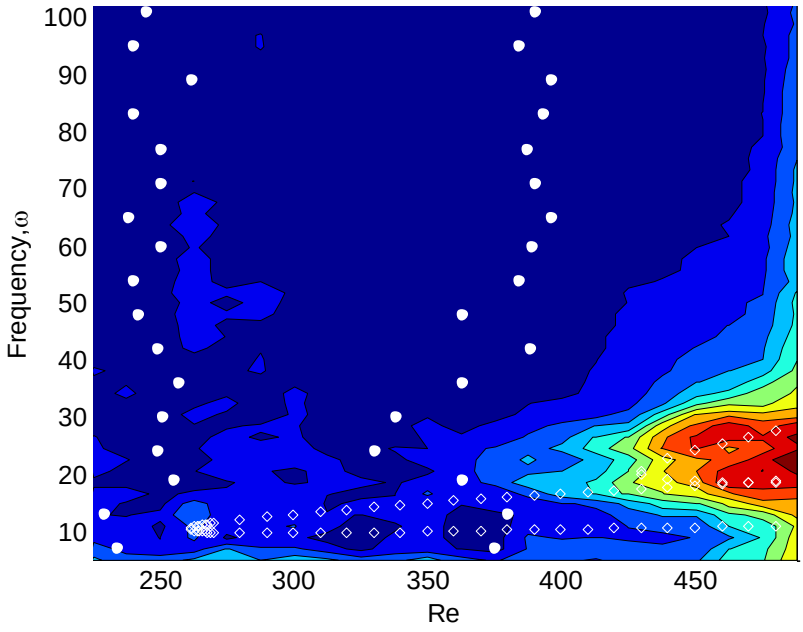

Figure 6.30 - Contour plot of a $\delta/\gamma = 0.2$ rough disk rotating at 6.28 rad/s with experimental and numerical neutral curves superimposed on top.

Figure 6.30 has had the numerical neutral curve for a roughness of 0.2 superimposed on top, which helps to visualise the proximity of the small burst of

excited frequencies with the location of the Type 2 lobe. However, the initial Reynolds location of the main, large peak does not match up with the Type 1 numerical lobe. Theory predicts that the main vortex peak in this case should not appear until Re = 425 and yet the unstable region seems to have occurred much further upstream than this. The reasons for this will be discussed in Chapter 6.6.

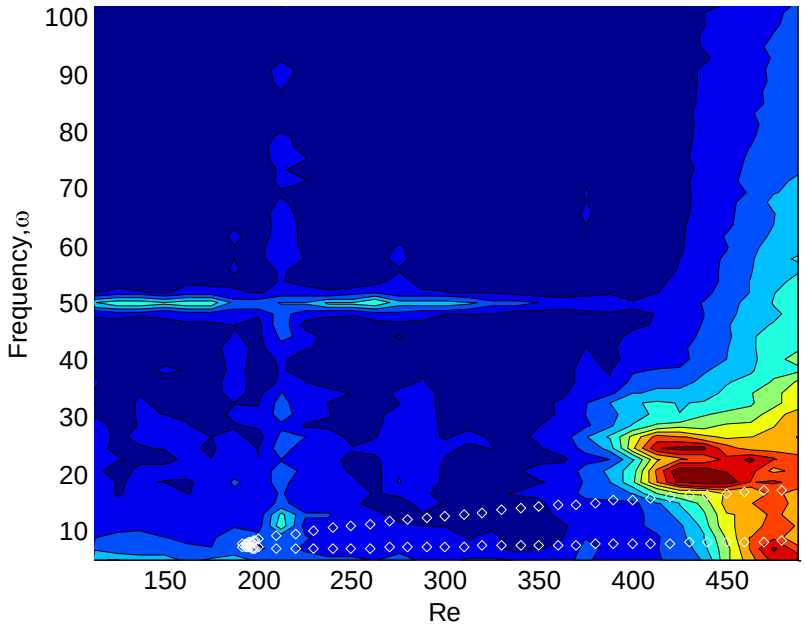

Figure 6.31 - Contour plot of a $\delta/\gamma = 0.33$ rough disk rotating at 6.28 rad/s with numerical neutral curves superimposed on top.

Figure 6.31 shows the frequency flow field for a disk with a roughness of 0.33 and the corresponding numerical neutral curve. This disk was another which displayed a small burst of frequencies at a low Reynolds number, which then die away downstream before the main vortex peak emerges. The superposition of the numerical neutral curve again shows an intriguing proximity between this small peak and the Type 2 lobe in both radial location and frequency. Once again though, the location of the disturbance caused by the Type 1 instability does not match up with the Type 1 lobe. Figure 6.32 shows the same disk rotating at a higher velocity

and displays the Type 2 emergence as well. For this disk, the small burst of frequencies at Re = 248 barely has time to fade away before the Type 1 instability occurs and grows to form spiral vortices.

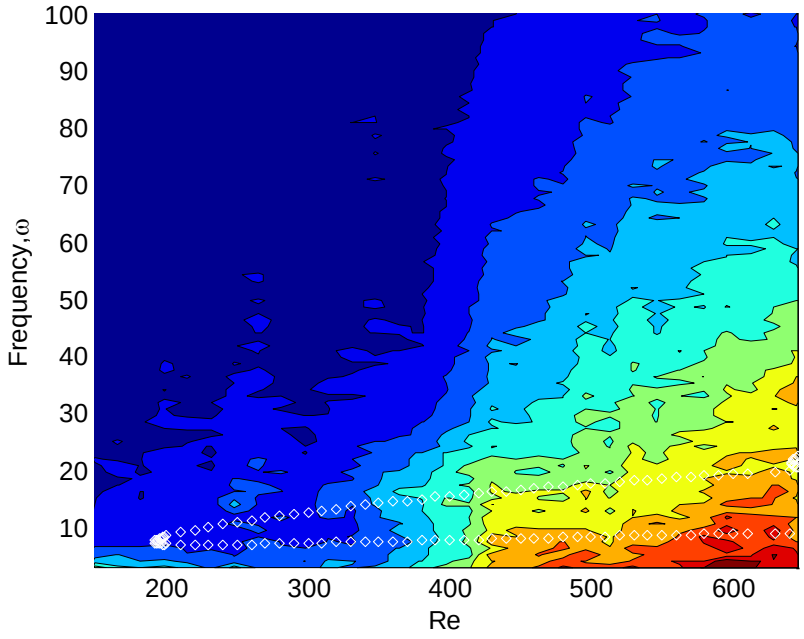

Figure 6.32 - Contour plot of a $\delta/\gamma = 0.33$ rough disk rotating at 10.99 rad/s with numerical neutral curves superimposed on top.

If these small peaks are caused by the Type 2 instability, there remains the question why the excitation dies away downstream rather than grow in a similar manner to the cross-flow instability. According to Figure 4.2c the growth rate of the Type 2 instability at this roughness should be large enough to cause the flow to stay excited at least until the Type 1 mode takes over at a higher Reynolds number.

In the contour plots above, there is a range of excited frequencies downstream of the small peak, so it could be that this is how the Type 2 mode manifests itself. It is known from the amplification plots that there is an increase in the total energy in the boundary-layer downstream of the Type 2 burst, and so rather than all the

excited energy forming the spiral vortices at a single frequency peak, instead the energy is spread out over a broad frequency range and so does not show up in the contour plots as strongly (appearing as a vertical strip above the small peak in each of the above plots). If this is the case, then it would explain why the Type 1 instability occurs earlier than the neutral curve predicts it should; the unstable growth and subsequent rise of energy in the flow caused by the Type 2 instability trips the Type 1 mode earlier than would be the case in a flow with no Type 2 mode. Clearly for the two modes to interact with one another in this way, non-linear effects would have to be occurring physically during the experiments, which therefore explains why the locations of the critical instabilities taken from the linear theory do not match up.

The appearance of these low frequency bursts so close to the expected theoretical locations of the Type 2 lobes adds credibility to the validity of the experimental findings and hot-film anemometry system, and can be considered one of the few incidences when the streamlines curvature instability has been seen experimentally in the rotating disk boundary-layer.

6.6 The onset of instability

As stated in Chapter 2.3 there are two important radial locations to look out for in the rotating disk boundary-layer. The first is the point of initial instability, which has been found numerically to be at Re≈287 for the smooth disk (Mack 1985; Malik 1986) and experimentally to be anywhere from Re≈294-377 (Kobayashi et al. 1980; Malik et al. 1981), while the second is the critical Reynolds number for transition to

turbulence. Values for this have been varied and many, but it is generally excepted that laminar flow cannot continue beyond Re=507 due to an absolute instability occurring near this value, which rapidly forces a transition to turbulence (Lingwood 1995a).

The point of initial instability can be predicted numerically by using the point on the neutral curves furthest upstream, which of course produces the data contained in Figure 4.5. To calculate the critical instability Reynolds number experimentally, we can use the method alluded to in Chapter 6.5; pick out the onset of instability using the frequency contour plots. The resolution of the initial instability or transition point may be within ±5mm of the actual value as this is the radial distance between each measurement. This translates to a maximum possible error of ±15 for the Reynolds number.

We generate a numerical value of Re=281 for our onset of instability, and between 294 and 382 for our experimental values for the smooth disk case, which are comparable to the previous studies mentioned above, which helps certify our method.

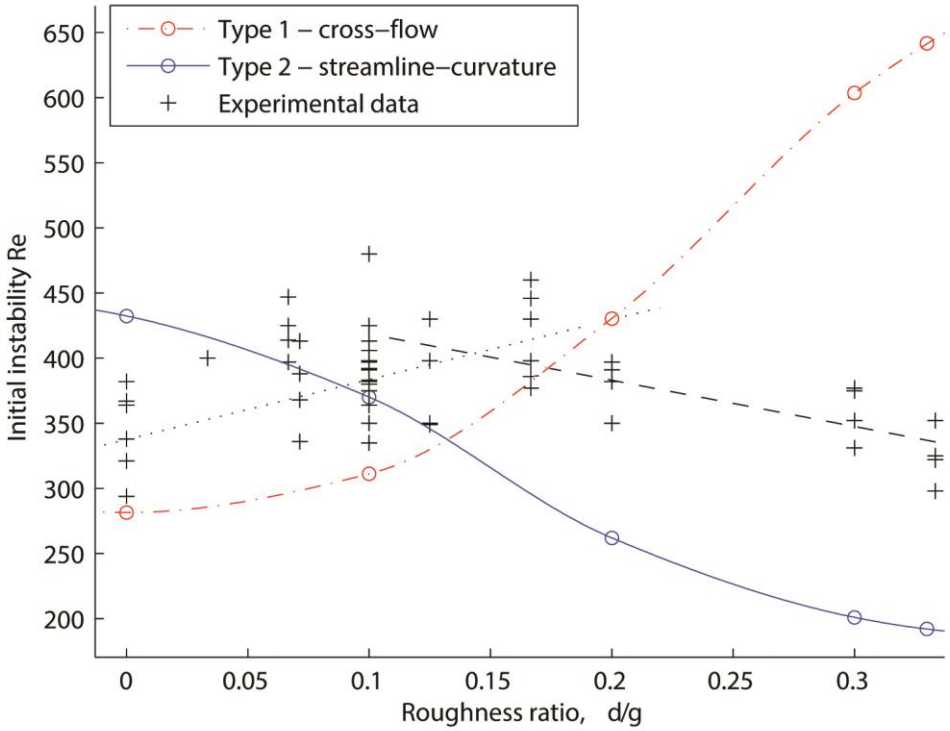

Figure 6.33 - Initial instability Reynolds numbers from numerical results with added experimental data. Dotted and dashed lines show lines of best fit through the first (δ/γ ≤ 0.16) and second (δ/γ > 0.16) halves of data respectively.

Figure 6.33 shows the same plot from Figure 4.5 with the experimental initial instability Reynolds numbers added for comparison. As mentioned before, the experimental values are likely higher than those actually occurring on the disk due to issues with reading the exact location through noisy data. In addition, with rougher disks producing a noisier base flow, the values for higher roughness ratio are likely to be further removed from the instability location than for lower degrees of roughness. For the disks such as that in Figure 6.29 which appear to have a Type 2 instability, the point of initial instability was measured from the start of the main vortex peak. Since the Type 2 disturbance dies down soon after it forms, it does not appear to lead to transition and as such we are not interested in it here.

The results in Figure 6.33 appear to show the results initially following the points from lobe 1. The left hand dotted trend line (for roughness ratios of less than and including 0.16) shows that as the roughness increases, the onset of instability is pushed downstream. This is true up until a roughness value of 0.2, wherein the second dashed trend line (for roughness ratios greater than 0.16) shows the instability point moving back upstream to lower Reynolds numbers. In Chapter 4 it was mentioned that the stabilizing of lobe 1 (the cross-flow instability) to occur at a higher Reynolds number could signify a delay in transition, if the cross-flow instability were the only route to turbulence. From Figure 6.33 it looks as though this may be the case. For low levels of roughness, the onset of initial instability can be delayed in the manner predicted by the shrinking of the cross-flow lobe of the neutral curve.

However, beyond 0.2 there is a change in the behaviour. Looking back to Figure 4.4 we see that this is roughly the ratio at which the growth rate of the streamline-curvature instability overtakes the cross-flow, and we know from Figure 6.29 that disturbances caused by the Type 2 instability can appear upstream at this level of roughness. It seems possible that the appearance of these Type 2 disturbances causes the Type 1 to occur earlier than it normally would, i.e. 'tripping' the instability by increasing the energy in the boundary layer, and therefore bringing forward the point of initial instability. It can be surmised that if the Type 2 disturbances did not appear, the point of initial instability would not be tripped early in this manner, and would continue to be delayed further for greater values of roughness.

6.7 Transition to turbulence

6.7.1 Location methods

The exact point of transition to turbulence is harder to pinpoint than the point of initial instability, and so a few different methods were used to narrow down the location. The first method used was to look directly at the raw voltage data from the probe to see if the radius at which the velocity trace descended into turbulence could be seen. This is the method used by many previous studies as it is often the easiest way to spot the breakdown of vortices in a clean flow (Kobayashi et al. 1980; Wilkinson & Malik 1985). In many of the current studies cases, the velocity data was too noisy, or the transition into turbulence was too gradual to pick out an exact radius, and so other methods needed to be employed. One other method was to look at the 'turbulence intensity' of the flow at each radius. The turbulence intensity is essentially just the variance of the velocity data points around the mean, where a larger variance indicates a more turbulent flow, and can be found using the formula:

$$TI = \left(\frac{\sqrt{\overline{x^2} - \bar{x}^2}}{\bar{x}} \right) \times 100 \qquad 6.2$$

Thus when this value is plotted against Reynolds number, the point of transition is usually found accompanied by a sudden increase in the turbulence intensity.

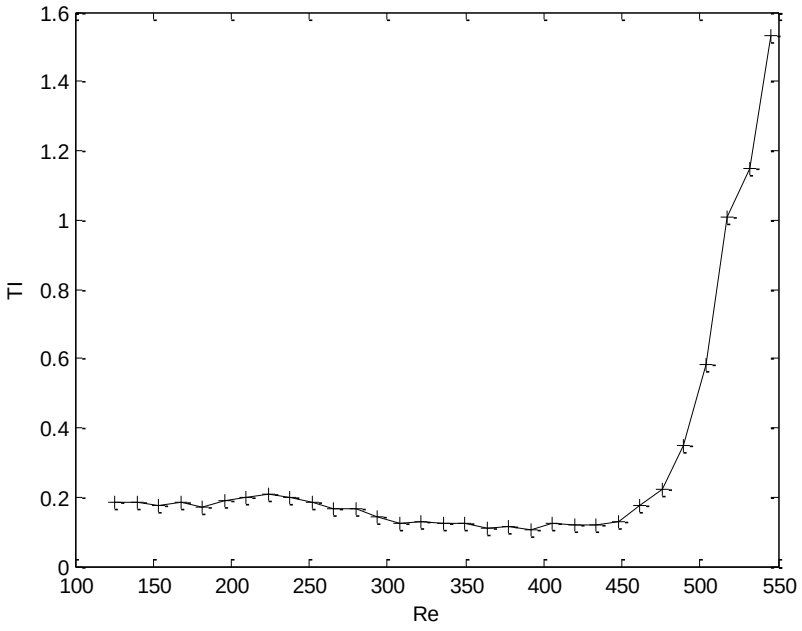

Figure 6.34 - Ensemble averaged turbulence intensity for $\delta/\gamma = 0.07$ disk rotating at 7.85 rad/s.

The turbulence intensity of an example disk is shown in Figure 6.34 and from it one can see the sharp increase in turbulence that signals transition. For this particular disk, the formation of the spiral vortices causes a small increase in turbulence intensity up to Re=480 before a sharp rise signals the transition region and breakdown of the vortices into turbulence.

Another way to help visualise the point of transition is use probability density function contour maps. This method was used successfully by Imayama (2012) to visualise the characteristics of the flow field and possibly detect the presence of the secondary instability seen by Kohama (1984).

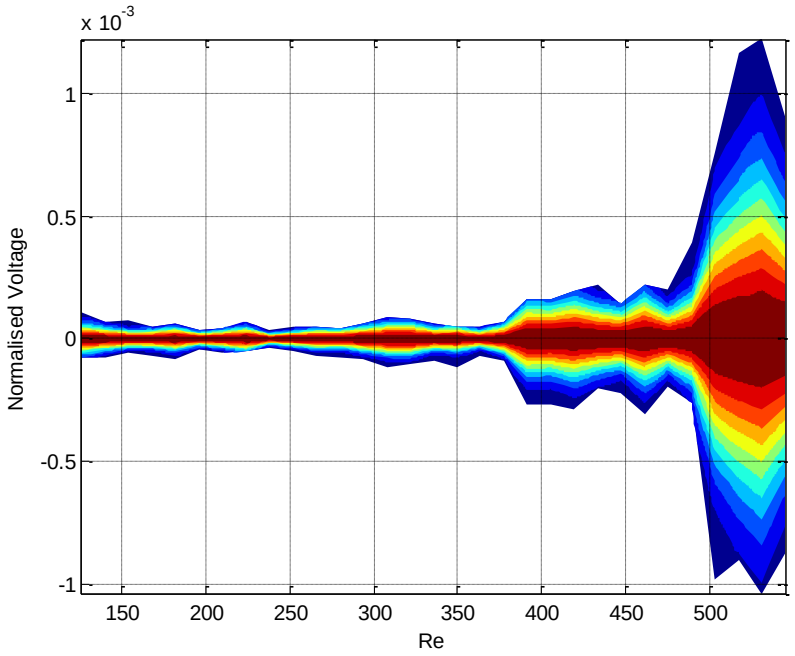

Figure 6.35 - Probability density function contour for $\delta/\gamma = 0.07$ disk rotating at 7.85 rad/s. Contours represent 10% intervals of the local PDF value.

Figure 6.35 shows an example PDF contour plot for the same rough disk as in Figure 6.34. The PDF differs from Imayama's in that due to the probes in this study not being calibrated, these are based on the voltage direct from the probes. Imayama's are made using their velocity measurements, and so can be normalised at each Reynolds number by the wall speed. The local wall voltage in the present study is unknown and so the PDF in Figure 6.35 has simply been normalised using the average voltage. Hence we lose a lot of the skewed structures seen in Imayama's plots, but retain the locations of the main changes in the flow. For example the locations of the initial instability and transition into turbulence are quite obvious in the above figure as the points where the PDF first bulges at Re≈375 and Re≈490 respectively.

6.7.2 Results

Using all the above methods to narrow down and confirm each point, the transition location for each flow field can be found and plotted in the below figure.

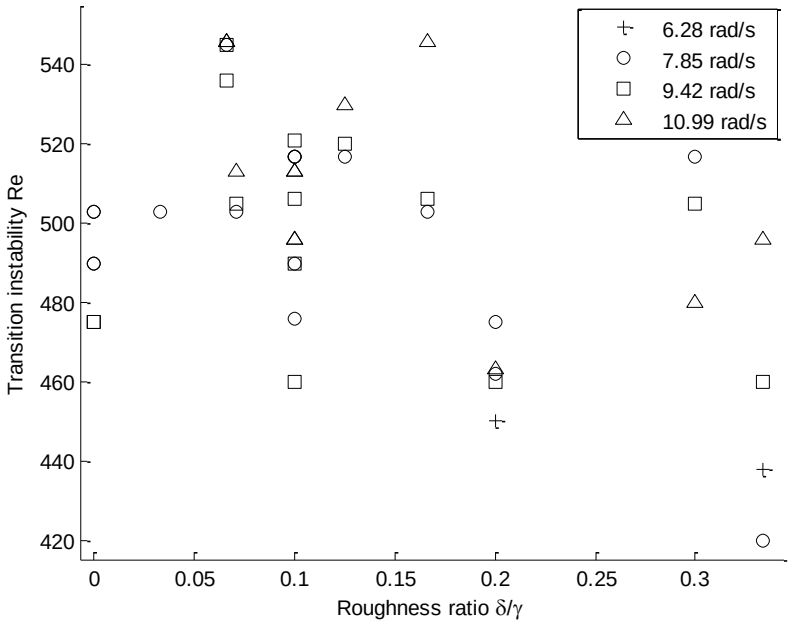

Figure 6.36 - Transition Reynolds numbers for varying roughness ratios.

Once again we have the problem that the roughness ratio does not always signify the actual amount of roughness, as two disks with the same roughness ratio can have significantly different roughness heights depending on their roughness pattern and rotational velocity. In Figure 6.36 it can be seen that increasing the roughness ratio does not necessarily change the transition point in either direction from the smooth case. It should be noted that for certain disks rotating at 6.28 rad/s the transition point is brought forward by the close proximity of the edge of the disk. Hence, either transition did not occur for these disks, or it occurred at the edge Reynolds number, due to effects from the disk edge. Thus these points have not been shown in the above plot.

To properly visualise the effect of roughness on the transition to turbulence in this case it is necessary to again use the non-dimensional roughness as a parameter. Figure 6.37 shows the data plotted against non-dimensional roughness.

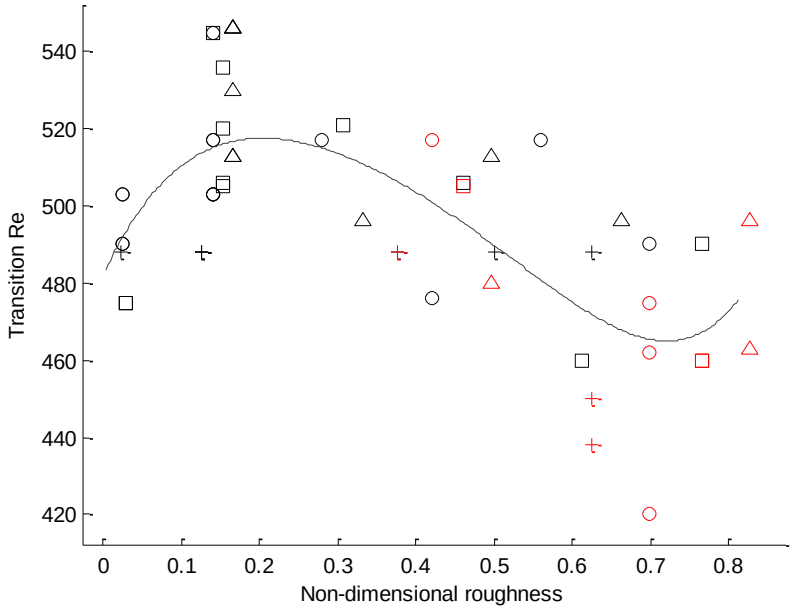

Figure 6.37 - Transition Reynolds numbers for non-dimensional roughness heights. Black markers show ratios < 0.2 and red markers are for ratios of ≥ 0.2. Rotational velocity markers are the same as in Figure 6.36.

As a result we see a much more obvious trend for the transition to turbulence, highlighted by a fifth degree polynomial interpolation curve. The smooth disk cases (adjusted here to have a small amount of non-dimensional roughness due to the O(10μm) roughness measured on the glass disks by the surface profiler) can be seen clustered below and around the theoretical transition point for smooth disks found by Lingwood (1995a) of Re=507, which supports the theory that the absolute instability at this point on smooth disks will trigger the onset of turbulent transition and nonlinearity and therefore ensure transition flow above this value of Re. For small roughnesses above smooth however, it seems as though the transition point has been delayed to create a cluster of results above Re=507. This is the first time

that roughness has been seen to delay transition for a rotating disk boundary-layer, although corresponding results have been described for the similar 3D swept wing boundary-layer (Reibert et al. 1996; Saric et al. 1998; Radeztsky et al. 1999). This new result helps cement the idea that roughness elements within certain criteria can be beneficial to a flow. Additionally, having already seen the point of initial instability delayed by low amounts of roughness in Chapter 6.6, it makes sense that this would in turn help to delay transition further downstream.

Similarly to the initial instability plot, we experience a drop in the transition point as the roughness moves above a certain value. However, unlike with initial instability which appeared to be dependent on roughness ratio, the critical level of roughness does not seem to be the same for the transition point. Whereas the stabilising effect of the initial instability seemed to occur for ratios up to a value of 0.2, it seems the beneficial effects of the roughness on transition has more to do with effective roughness height rather than roughness ratio. In Figure 6.37 the results for disks with ratios less than 0.2 are coloured black, while the disks with ratios of 0.2 and higher are red. The trend of decreasing transition point begins before the ratio reaches 0.2, and thus the turning point seems to instead be dependent on non-dimensional roughness height instead.

A non-dimensional roughness height of between 0.1 and 0.3 appears to be the most beneficial to transition delay. Using the boundary-layer thickness formula provided by von Kármán (1921) it can be shown that with a non-dimensional boundary-layer of thickness of $\zeta = 5.5$, the roughness needs to be in the region of

1.8-5.5% of the height of the boundary-layer to provoke the transition delay seen above.

6.8 Nonlinearity

Although the numerical half of this research is linear, the likelihood of having only linear behaviour in the experimental data is low. While every care has been taken to avoid any nonlinear effects (the placing of the annular shroud to prevent feedback of turbulence, for example) there will still be some effects which exist within the boundary-layer.

Nonlinear effects can be looked at by examining the higher frequency harmonics that arise with them, and comparing them to the fundamental frequencies. We know that the fundamental wave packet is centred on the main vortex peak between $\omega = 15 - 35$, and so the first superharmonic wave packet will exist at roughly double that value, $\omega = 36 - 70$. The amplitudes of the superharmonics are proportional to the amplitudes of the fundamental modes, and so if the higher harmonic data points $|H|$ are plotted against the squared fundamental amplitudes $|F^2|$, it should be possible to distinguish regions where the first set of harmonics increase at an equal or higher rate than the squared fundamental data. The region where the superharmonics begin increasing faster than the fundamental frequencies should point to a region of nonlinear behaviour. This approach is taken by Jarre et al. (1996b) to create log plots which display the regions of nonlinearity for smooth disks rotating in water in a similar manner to the setup in the current study.

Figure 6.38 shows a typical nonlinear amplitude plot for a $\delta/\gamma = 0.06$ disk. Rather than being ensemble averaged as in most of the above analysis, every amplitude value from each of the 50 disk rotations was plotted to give a much larger data set.

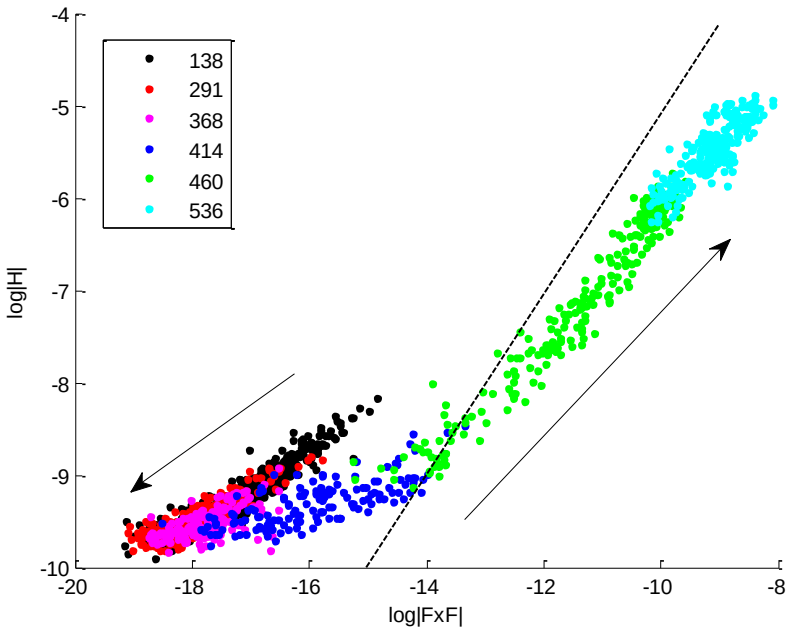

Figure 6.38 - Amplitude of the harmonic frequency wave packet against the square of the fundamental frequency wave packet. Arrows indicate increasing Reynolds numbers on a $\delta/\gamma = 0.06$ disk rotating at 9.42 rad/s. Legend indicates lower bound for each coloured region. Dotted line shows gradient = 1.

For the data at a low radius, the amplitudes of both modes appear to be damped, as the data points from Re=138 onwards decrease in amplitude on both axes. This verifies what was seen in the amplification curves from Chapter 6.5 where the power of the Fourier plots lost energy initially to reach a minimum before increasing further downstream. The data points in this region tend to clump together, indicating no growth of any kind, either with the fundamental or harmonic modes.

From Re=414 however, the blue region of points suddenly spreads outwards; the fundamental mode wavepacket increasing at a higher rate than the superharmonic

mode. This growth suggests that the energy in this part of the flow is increasing at a linear rate. It is interesting to note that this Reynolds number is the approximate radius in the flow that the initial vortex instability is found for this particular disk in Chapter 6.6. Thus we can conclude that the start of this blue linear region describes the point of initial instability. The fact that this occurs during a linear region in the flow is reassuring in that it helps validate the results for the numerical initial instability calculated using linear stability theory.

From Re=460 onwards there appears to be another change in the behaviour, as the harmonic modes appear to increase proportionally with the squared fundamental amplitudes, causing a kink in the data points. This indicates a shift from linear to nonlinear behaviour at this location.

Above a certain Reynolds number, the data points appear to cluster in the top right hand corner of the figure. This is down to the saturation we saw in the amplification curves, which is usually a sign of turbulent transition. This does seem to coincide with the point in the flow at which transition for this disk was measured using the methods described in Chapter 6.7, which is marked in the above figure at Re=536. However, this saturation clustering and the recorded transition point do not always match up as succinctly, as will be discussed below.

It appears that nearly all of the data from the disks follows this trend: clustered data at low Reynolds numbers with no or negative growth; linear growth of the fundamental mode indicating the onset of instabilities; a switch to nonlinear behaviour resulting in a kink in the plot; finally clustering of the points at high Reynolds numbers as the flow reaches saturation through turbulence. Jarre et al.

(1996b) saw a very similarly shaped plot for their smooth disk flow, so it can be concluded that this is the standard shaped plot for the rotating disk flow.

Occasionally one would find a disk that skipped the linear region and progressed directly from the low stagnant growth to the nonlinearly increasing region such as in the example below.

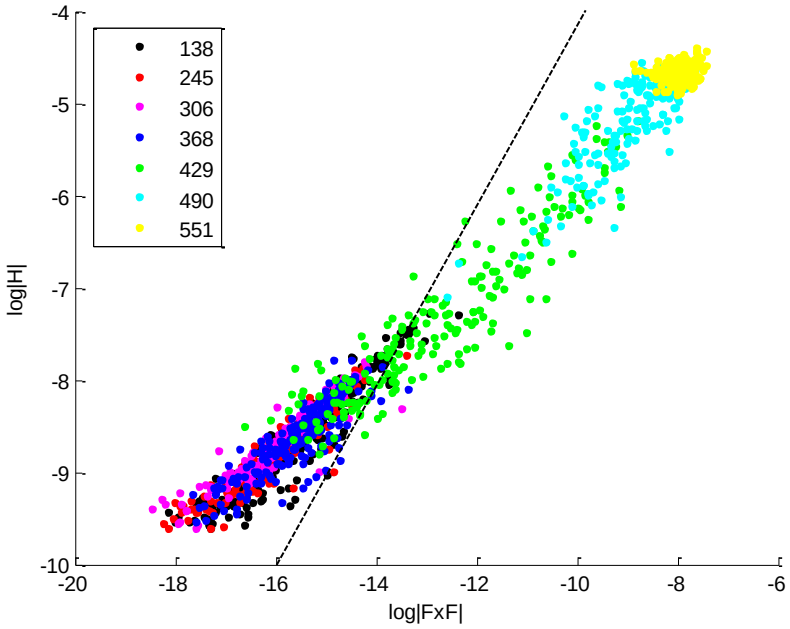

Figure 6.39 - Nonlinearity plot for a $\delta/\gamma = 0.167$ disk rotating at $\Omega = 9.42$ rad/s. Dotted line shows gradient = 1. Linear region is absent.

For the disk shown in Figure 6.39 the flow experiences the same negative growth, nonlinear and saturation regions as the other disks, but the linear region is absent. It appears that the harmonic modes in this case are amplified when the initial instability occurs, causing the instability to develop nonlinearly from its genesis. However, this activity does not seem to be a repeatable behaviour, as it occurs only for a few disks at certain speeds but not others. It could therefore be caused by some external reason such as debris on the disk surface triggering the nonlinear behaviour early for example. Whatever the cause, it is interesting that the

nonlinear behaviour is picked up in the frequency contour plot for that disk, emerging as a second, smaller superharmonic peak at a frequency of $\omega = 68$ (See Figure 6.40).

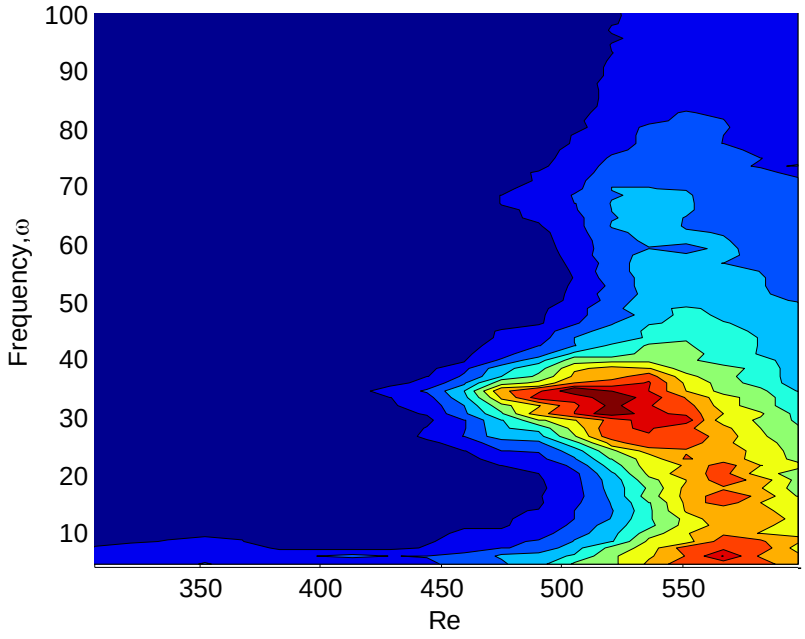

Figure 6.40 - Contour plot for $\delta/\gamma = 0.167$ disk rotating at $\Omega = 9.42$ rad/s. The harmonic mode can be seen as a peak at $\omega = 68$.

The nonlinearity plot can be used to look at the data from disk in Figure 6.29 to see how the possible emergence of the Type 2 instability affects the nonlinearity diagram. This plot is shown in Figure 6.41 and is noticeably different to the standard shaped plot seen above. The black points positioned at a Reynolds number of Re=225 and upwards appear to follow the normal trend of having damped amplitudes which are decreasing slightly in energy and align to a downward trajectory on the nonlinearity plot. However at Re=263, the position of the small peak in Figure 6.29, the cluster of red data points experiences a jump up in harmonic frequencies and fundamental frequencies. This behaviour suggests a small burst of energy at that radius in which the flow experiences nonlinear growth.

After this small burst, the flow returns to normal, with the pink data points experiencing negative or stagnant growth symbolised by a clustering in the lower left-hand corner. It seems as though the burst at Re=263 caused the rest of the plot to shift upwards, before continuing with the usual regions seen in the smooth case although now at a higher energy state. At Re=363 (dark blue data points) there begins a short region of linear growth which signifies the triggering of the Type 1 instability. This region only lasts for a short distance compared to the linear region in Figure 6.38 (ΔRe20 compared to ΔRe50), with the nonlinear growth beginning at Re=388.

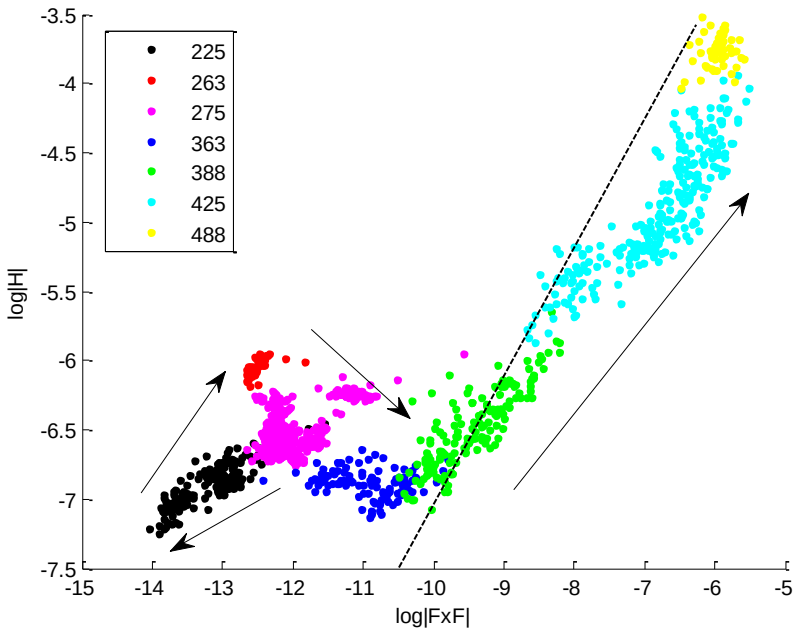

Figure 6.41 - Nonlinearity plot for a $\delta/\gamma = 0.2$ disk rotating at $\Omega = 6.28$ rad/s. Dotted line shows gradient = 1. Arrows show the direction of increasing Reynolds number.

It seems that the shape of the flow has been altered by this small unstable burst upstream. The Type 1 instability occurs earlier (Re=363 compared to Re=414) and the linear region has been reduced, similar to the flow in Figure 6.39. The reason is most likely due to the emergence of the Type 2 burst further upstream. Although

the burst itself does not grow, it appears to trigger the early Type 1 instability, as well as the early nonlinear section of the flow by shifting the whole plot to a higher energy state.

7 Conclusions

This thesis is concerned with observing the effects that a distributed, patterned roughness has on the three-dimensional rotating boundary of a rotating disk. The study is split into two parts; a numerical stability analysis in which a sinusoidal disk surface is used to modify the basic flow profiles, which are then used in the stability analysis, and a complementary experimental study in which grooved disks designed to mimic the sinusoidal surface are rotated in a water tanks while the boundary-layer flow characteristics over the disks are measured with a hot-film anemometry system. The results of this study are summarised in the following section, before a brief outline of possible further work is contained in Chapter 7.2.

7.1 Current work

The numerical section extends the work presented in a paper by Yoon et al. (2007) in which the surface of a rotating disk system is replaced with a sinusoidal function and a new set of von Kármán's differential equations are derived. The focus of the original Yoon paper was to see how the wavy surface affected the heat transfer characteristics of the rotating disk system. The aim of this thesis however was to use this new system of equations to predict the mean velocity profiles of a flow with a wavy surface. This involved using a commercially obtained routine from NAG which reduced the system of partial differential equations to a system of solvable ordinary differential equations.

The results from the NAG routine show a decrease in the velocity of the radial profile wall jet as well as a thickening of the boundary-layer in general as the

roughness ratio of the sinusoidal function is increased. These two effects result in the increase in the height of the inflection point in the radial profile.

A similar thickening of the boundary-layer is seen for the azimuthal flow profile, with the overall velocity in the central region of the boundary-layer increasing as the roughness is increased. The axial profile experiences an increase in velocity too, which makes physical sense in that more fluid would need to be drawn down into the boundary-layer to conserve the mass lost through the thickening of the boundary-layer in the other two directions.

For the experimental study, aluminium disks with grooved patterns cut into them were manufactured to mimic the sinusoidal surface described by the numerical surface function. These disks were then placed into an existing rotating disk system, and hot film probes were used to measure the velocity profiles. Overall, the quality of the measured velocity profiles was poor, but in the absence of anything better, conclusions were derived from these results to try and visualise the effect the roughness had on the flow. Disks with a high roughness ratio appeared to experience a larger drop in the radial wall jet velocity as well as a thickening of the boundary-layer. Estimates of the inflection point height showed an increase with roughness ratio as well. The azimuthal flow profile saw an increase in overall velocity and a thickening of the boundary-layer. Experimental velocity profiles from other investigations to compare against are relatively scarce, as few authors choose to use a global distributed roughness on the surface of the disk, while those that did chose to focus on drag reduction or heat transfer rather than flow profiles. However, Watanabe et al. (2007) performed a study where a disk with fine spiral

grooves was rotated in an enclosed space during which the velocity profiles were measured. Groove depths were comparable to those used in this study, although velocity profiles are presented for one disk only. Their results show a deceleration in the radial velocity similar to that predicted in our numerical results and seen in the experimental hot-film data. Any boundary-layer thickening for the radial or the azimuthal profiles however is missing, although this could be due to the disk being enclosed rather than open. The enclosed nature of Watanabe's disk may also account for their azimuthal profile showing a deceleration in velocity where ours shows acceleration.

The changes induced by the roughness on the velocity profiles lead to the next numerical result, namely the differences in the neutral curves. The mean flow profiles produced by the NAG routine were then subjected to a linear stability analysis using code created by R. Lingwood and used in preceding studies by Lingwood (1995a) and Garrett (2002).

The results of the numerical stability study show a stabilising effect of the main Type 1 cross-flow lobe as it becomes thinner and is pushed back to higher Reynolds numbers. The critical point of the Type 1 lobe also decreases slightly in terms of azimuthal vortex number as roughness is increased. The Type 2 lobe however increases dramatically with increased roughness ratio. The streamline-curvature lobe eventually overtakes the Type 1 lobe at a ratio of 0.12, becoming the instability that occurs furthest upstream. However, it is not until a ratio of 0.2 that the growth rates of the Type 2 instability become large enough to suggest it will be the dominant mode.

The reduction of the Type 1 lobe can be explained by the behaviour of the radial velocity profile when exposed to an increasing rough surface. The decrease in the velocity of the centrifugal wall jet in comparison with the non-changing azimuthal velocity suggests a reduction in the strength of the cross-flow effect, leading to a reduction in the growth of that mode.

Meanwhile, the apparent growth of the Type 2 mode must also be affected in some way by the altered mean flow. Looking at Itoh's streamline-curvature parameter κ (Itoh 1996), it can be seen that it depends on the boundary-layer thickness divided by the radius of the curved streamlines. Now, a decrease in the wall jet velocity seen in the radial profiles will act to reduce the radius of the resultant spiral velocity of the flow as the component of velocity forcing the fluid outwards is reduced. Hence the radii of the curved streamlines of the flow are reduced as roughness is increased. Similarly, the thickening of the boundary-layer seen in all three velocity profiles can be seen to increase the effect of the streamline-curvature terms on the flow. These two effects add to the overall streamline-curvature parameter strength and therefore to the growth of the streamline-curvature instability mode.

In addition to the velocity profiles, the experimental set-up was also used to plot frequency fields for each rough disk, which helped to visualise the flow structure over the disk surface. The frequency fields were created by taking a Fast Fourier Transform of the velocity trace to detect the frequencies contained in the flow at a range of disk radii. Results were taken many times at each radius and ensemble averaged to remove any temporally changing data. The frequency fields could then

be used to look for a variety of features which would complement the numerical half of the study.

Small amounts of roughness ($\delta/\gamma < 0.2$) appear to push back the experimental initial point of instability seen in the frequency fields, following the numerical trend set by the front of the cross-flow (Type 1) lobe as it stabilises and decreases. This is caused by the reduction of the strength of the cross-flow effect from the decreased wall jet velocity and change in height of the inflection point. This trend continues up until a roughness of 0.2, at which point the initial instability point drops back to occur at locations upstream of the smooth case. This behaviour coincides with the emergence of the disturbance thought to be caused by the Type 2 streamline-curvature instability. It is thought that the Type 2 mode occurring upstream might triggers the Type 1 to occur earlier than it would normally do. The Type 2 mode does not cause vortices in the same way that the Type 1 does, but the energy it introduces into the system helps bring forward the location of the Type 1 initial instability. This appears to be confirmed by the nonlinear plots, which plot the squared amplitudes of the fundamental frequencies against the amplitudes of the harmonics. This highlights regions of linearity and nonlinearity in the flow, where one set of frequencies grows in relation to the other. These plots show a sudden jump in the amplitudes of the flow frequencies at the location of the Type 2 disturbance. This shifts the rest of the nonlinear plot up to a higher energy state, and hastens the onset of the nonlinear region of the flow, suggesting that the Type 1 instability location has been brought forward.

Another important result was that in general, a higher amount of roughness causes a decrease in the number of spiral vortices seen around the circumference of the disk, confirming the results seen by Watanabe (1987; 1993) and the predictions of the neutral curves created by the stability analysis. However, simply increasing the roughness height while keeping the roughness ratio the same, such as in many other roughness studies, will not necessarily have the same effect. The roughness ratio must increase as well for there to be a drop in the number of vortices. This finding may be linked to a study by Floryan and Asai (2011) who found that roughness elements that were spaced too far apart transitioned to act like isolated roughness resulting in a stabilising effect on the stationary vortices. For the disks in this investigation, this means that for a set of disks with equal roughness heights, an increase in groove separation will stabilise the stationary vortices and result in a number of spirals close to the smooth case. Moving the grooves closer together however will couple the disturbances passing over the roughness elements and destabilise the vortices, resulting in fewer of them forming.

This decrease in the number of vortices does not appear to be caused by any switch in the dominant mode, as the reduction of the vortex number appears to begin at a roughness before the Type 2 mode even becomes dominant. The slope of the decreasing experimental vortex numbers is also too steep to be caused by the slight reduction in the initial instability vortex number of the Type 1 mode (the upper line in Figure 4.4). Instead, the behaviour of the vortex number is thought to be caused by the decrease in the strength of the Type 1 growth rate. The reduction of this growth rate begins immediately at small roughness ratios, unlike the growth of the

Type 2 mode which requires a higher ratio to take effect (see Figure 4.2). Also, the reduction of the Type 1 growth rates occur to a greater degree with increasing roughness (decreasing by a factor of approximately 10), which would account for the steeper drop-off in vortex number; the Type 2 growth rates instead increase at a much shallower level (increasing by a factor of approximately 2).

By utilising a variety of methods to measure the transition point, it was found that a small amount of roughness can cause a beneficial delay in the transition point of the flow, similar to what has been seen in many previous studies on roughness induced transition delay (Carrillo et al. 1996; Fransson et al. 2006). In this case it is dependent on roughness height rather than roughness ratio, and a roughness of between 1.8-3.6% of the height of the boundary-layer seems to show the transition point moving downstream. Roughness larger than this however, causes the transition point to move back upstream. Carrillo et al. (1996) performed experiments in a wind tunnel that showed a similar delay in the transition point for a swept wing that was caused by micron sized roughness elements positioned near the attachment line. By carefully spacing the roughness elements at a distance apart close to the wavelength of the most unstable wave, Carrillo managed to suppress that wave and delay the transition beyond what was achieved with no additional roughness (55 per cent chord to 80 per cent chord with roughness). It is not known whether the transition delay seen in this study are due to a similar wave suppression or perhaps by breaking up any turbulent coherence, similar to that seen in the study by Sirovich and Karlsson (1997). Of course, it could simply be that by delaying the point of initial instability by reducing the cross-flow effect, the

follow-on effect is a delay in the final transition location, a theory which is strengthened by the decrease in both initial instability location and transition point at higher roughness levels.

7.2 Further work

The entirety of this study has been concerned only with waves stationary with respect to the rotating disk, but of course stationary waves are not the only disturbances present in the boundary-layer. Travelling waves will also have an effect on the stability of the flow, and as such the effect of roughness on the travelling waves will need to be studied. For example, a channel flow study by Floryan (2011) found that increasing the distance between the roughness elements in a system could destabilise it by producing travelling waves, while placing the elements closer together had a stabilising effect.

Identifying travelling waves with the numerical stability code is relatively simple, in that one can adjust the ratio of wave speed to disk speed to look for waves which are not stationary on the disk surface. For the results of this study, the ratio was set to $\frac{\omega_r}{\beta} = 1$ but waves travelling at any fraction of the disk speed can be found easily. The difficulty arises in the experimental stage, as the ensemble averaging process erases any travelling waves picked up in the velocity traces. However, it is possible to pick out non-stationary waves by utilising a pair of hot-film probes rather than one, such as in the study by Jarre et al. (1996b). They conclude that only the stationary waves are caused by the surface roughness, and that any travelling waves present have been introduced by recirculation of turbulence at the edge of

the disk. Seeing how the travelling waves are affected by increasing surface roughness would seek to confirm this.

Another way to possibly measure travelling waves effectively while continuing to use only one probe would be to affix the probe stationary with respect to the disk so that the stationary waves were not picked up, and only travelling waves passed over the probe sensor. While attempting to produce an alternative calibration method during this present study, the probe was mounted onto the rotating turntable and attached to the anemometer system through a slip-ring connection. Although this method was abandoned as a calibration method in lieu of a simpler one, it proved that the probe could function while mounted in the rotating frame of reference. Thus, in the future, the probe could be mounted onto the disk itself to attempt to study the travelling waves passing through the boundary-layer.

The function used to describe the surface of the rough disk need not necessarily be as simple as a sine wave. Since any dependence on r is lost upon averaging over one wavelength, the function can, in theory, be any superposition of any combination of waves, providing the function remains oscillatory. Thus the function can be tailored to suit any kind of concentric surface roughness. For example if the grooves in the disk were of a similar width to the pitch between the grooves, a square wave function might describe the surface more accurately. Figure 7.1 shows a comparison between a sine wave and a finite approximation of a square wave with equal amplitude and wavelength, described by the function:

$$s = \delta sin\left(\frac{\pi r}{\gamma}\right) + \frac{1}{3}\delta sin\left(\frac{3\pi r}{\gamma}\right) + \frac{1}{5}\delta sin\left(\frac{5\pi r}{\gamma}\right) + \frac{1}{7}\delta sin\left(\frac{7\pi r}{\gamma}\right) + \frac{1}{9}\delta sin\left(\frac{9\pi r}{\gamma}\right) \quad 7.1$$

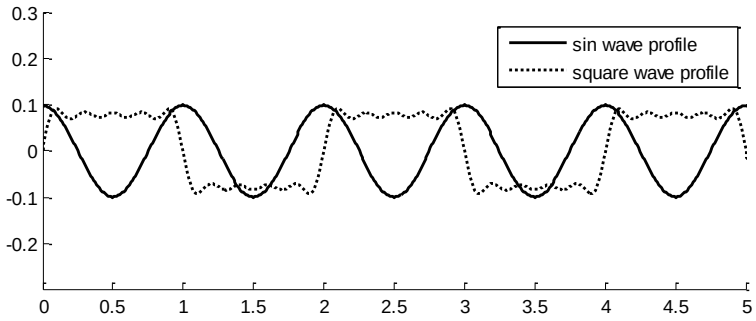

Figure 7.1 - Visual comparison between a sine wave and a square wave both with $\delta = 0.1$ and $\gamma = 1$.

The function could just as easily be a triangular wave or a combination of both.

Such functions were trialled for use with the current study, but in general adding the square wave function in place of the sinusoid increased the computation time of the NAG routines and decreased the reliability of the code. No full sets of data were obtained due to constant crashing and any results gained were inconclusive. Thus it was decided to focus on the simpler sinusoidal function and not the square or any other. Perhaps in future studies the code can be optimised to work with a variety of different profiles, in order to produce a rough surface closer to those found in the physical world.

It has been noted in Chapter 6.1 that the system used to obtain the velocity profiles was somewhat unreliable in terms of calibration, and as such the results obtained did not fit the expected theoretical curves. The system used was installed over 15 years ago and is due for an update. A new, possibly simplified, hot film anemometry

system would be able to confirm the velocity profiles produced by the numerical code much more accurately, which would improve the validity of the code. In addition to this, more sets of results could be taken on a greater variety of rough disks over $\partial/\gamma = 0.2$ to confirm the finding of the emergent Type 2 instability at high levels of roughness.

It has been noticed by P. Thomas (personal communication) that the growth of the Type 2 instability due to roughness is qualitatively very similar to results seen in a study by Cooper and Carpenter (1997) in which the compliant levels of the disk surface are increased by using a viscoelastic wall model. For high levels of compliance, the Type 2 region of the neutral curve increased in size and the critical Reynolds number moved upstream in the same manner seen in this roughness study, but there was no visible reduction in the Type 1 region of the flow. It would be interesting to discover whether the two effects are related, and in what way, by comparing results from the two investigations more closely and possibly adding compliance to this stability model.

8 Bibliography

Adkins, D.R. & Brennen, C.E., 1988. Analyses of hydrodynamic radial forces on centrifugal pump impellers. *Transactions of the ASME*, 110, pp.20–28.

Balachandar, S., Streett, C.L. & Malik, M.R., 1992. Secondary instability in rotating-disk flow. *Journal of Fluid Mechanics*, 242, pp.323–347.

Banks, W.H.H., 1965. the Boundary Layer on a Rotating Sphere. *The Quarterly Journal of Mechanics and Applied Mathematics*, 18(4), pp.443–454.

Baron, A. & Quadrio, M., 1993. Some preliminary results on the influence of riblets on the structure of a turbulent boundary layer. *International Journal of Heat and Fluid Flow*, 14(3), pp.223–230.

Barrow, A. & Garrett, S.J., 2013. Convective and absolute instabilities in the boundary layer over rotating spheres with surface mass flux and incident axial flow. *European Journal of Mechanics - B/Fluids*, 38, pp.93–100.

Bechert, D.W., Bruse, M. & Hage, W., 2000. Experiments with three-dimensional riblets as an idealized model of shark skin. *Experiments in Fluids*, 28(5), pp.403–412.

Bertrand, J. & Couderc, J.P., 1978. Hot-film calibration in liquids. *DISA Info*, 23, pp.28–32.

Braslow, A.L., 1999. A history of suction-type laminar-flow control with emphasis on flight research. *NASA monographs in aerospace history*, 13.

Brown, G.O., 2002. The history of the Darcy-Weisbach equation for pipe flow resistance. *Environmental and Water Resources History*, 38(7), pp.34–43.

Brown, W.B., 1961. A stability criterion for three-dimensional laminar boundary layers. *Boundary layer and flow control*, 2, pp.913–923.

Bruun, H.H., 1995. *Hot Wire Anemometry: Principles and Signal Analysis*, Oxford University Press, Incorporated.

Carpenter, P.W., 1997. The right sort of roughness. *Nature*, 388(August), pp.713–714.

Carpenter, P.W., Davies, C. & Lucey, A.D., 2000. Hydrodynamics and compliant walls : Does the dolphin have a secret ? *Current Science*, 79(6), pp.9–13.

Carrillo, R.B., Reibert, M.S. & Saric, W.S., 1996. *Distributed-roughness effects on stability and transition in swept-wing boundary layers*,

Cheng, S.-I., 1953. On the stability of laminar boundary layer flow. Rep. 211. *Aero. Eng. Lab., Princeton University*, pp.346–350.

Choi, K., 2006. The rough with the smooth. *Nature*, 440(April), p.2006.

Cochran, W.G. & Goldstein, S., 1934. The flow due to a rotating disc. *Mathematical Proceedings of the Cambridge Philosophical Society*, 30(03), p.365.

Colley, A.J., 1997. *An experimental investigation of the flow in the boundary layer above a rotating disc, with compliant characteristics, in water*. University of warwick.

Colley, A.J. et al., 1999. An experimental study of boundary-layer transition over a rotating, compliant disk. *Physics of Fluids*, 11(11), p.3340.

Colley, A.J. et al., 2006. Experimental verification of Type-II-eigenmode destabilization in the boundary layer over a compliant rotating disk. *Physics of Fluids*, 18(5), p.054107.

Coltrin, M.E., Kee, R.J. & Evans, G.H., 1989. A Mathematical Model of the Fluid Mechanics and Gas-Phase Chemistry in a Rotating Disk Chemical Vapor Deposition Reactor. *Journal of The Electrochemical Society*, 136(3), pp.819–829.

Cooper, a. J. & Carpenter, P.W., 1997. The stability of rotating-disc boundary-layer flow over a compliant wall. Part 1. Type I and II instabilities. *Journal of Fluid Mechanics*, 350, pp.231–259.

Corke, T.C., Bar-Sever, A. & Morkovin, M. V., 1986. Experiments on transition enhancement by distributed roughness. *Physics of Fluids*, 29(10), p.3199.

Corke, T.C. & Knasiak, K.F., 1998. Stationary travelling cross-flow mode interactions on a rotating disk. *Journal of Fluid Mechanics*, 355, pp.285–315.

Davies, C., Thomas, C. & Carpenter, P.W., 2006. Global stability of the rotating-disk boundary layer. *Journal of Engineering Mathematics*, 57(3), pp.219–236.

Dryden, H.L., 2012. Review of published data on the effect of roughness on transition from laminar to turbulent flow. *Journal of the Aeronautical Sciences (Institute of the Aeronautical Sciences)*, 20(7).

Elsamni, O., Chun, H. & Yoon, H., 2007. Drag reduction of turbulent flow over thin rectangular riblets. *International Journal of Engineering Science*, 45(2-8), pp.436–454.

Faller, A.J., 1991. Instability and transition of disturbed flow over a rotating disk. *Journal of Fluid Mechanics*, 230, pp.245–269.

Fedorov, A. V, 1989. Excitation of Waves of Instability of the Secondary Flow in the Boundary Layer on a Swept Wing. *Journal of Applied Mechanics and Technical Physics*, 29(5), pp.643–648.

Fedorov, B.I. et al., 1976. Transitional Flow Conditions on a Rotating Disk. *Journal of Engineering Physics*, 31, pp.1448–1453.

Fish, F.E. & Lauder, G.V., 2006. Passive and Active Flow Control By Swimming Fishes and Mammals. *Annual Review of Fluid Mechanics*, 38(1), pp.193–224.

Floryan, J.M., 1997. Stability of wall-bounded shear layers in the presence of simulated distributed surface roughness. *Journal of Fluid Mechanics*, 335, pp.29–55.

Floryan, J.M. & Asai, M., 2011. On the transition between distributed and isolated surface roughness and its effect on the stability of channel flow. *Physics of Fluids*, 23(10), p.104101.

Fransson, J.H.M. et al., 2006. Delaying Transition to Turbulence by a Passive Mechanism. *Physical Review Letters*, 96(6), pp.1–4.

Garrett, S.J., 2002. The Stability and Transition of the Boundary Layer on Rotating Bodies. *Thesis*.

Garrett, S.J., 2010. Vortex-Speed Selection within the Rotating-Disk Boundary Layer. *Algorithms & Computational Technology*, 4(1), p.71.

Garrett, S.J., Hussain, Z. & Stephen, S.O., 2010. Boundary-Layer Transition on Broad Cones Rotating in an Imposed Axial Flow. *AIAA Journal*, 48(6), pp.1184–1194.

Garrett, S.J. & Peake, N., 2002. The stability and transition of the boundary layer on a rotating sphere. *Journal of Fluid Mechanics*, 456, pp.199–218.

Gaster, M., 1974. On the effects of boundary-layer growth on flow stability. *Journal of Fluid Mechanics*, 66(3), pp.465–480.

Gray, W.E., 1952. The nature of the boundary layer at the nose of a swept back wing. *Unpublished, Min. Aviation, Lond*.

Gregory, N., Stuart, J.T. & Walker, W.S., 1955. On the stability of three-dimensional boundary layers with application to the flow due to a rotating disk. *Phil. Trans. R. SOC. Lond*, 248(943), pp.155–199.

Hall, P., 1986. An Asymptotic Investigation of the Stationary Modes of Instability of the Boundary Layer on a Rotating Disc. *Proceedings of the Royal Society of London . Series A , Mathematical and Physical*, 406(1830), pp.93–106.

Healey, J.J., 2007. Instabilities of flows due to rotating disks: preface. *Journal of Engineering Mathematics*, 57(3), pp.199–204.

Healey, J.J., 2010. Model for unstable global modes in the rotating-disk boundary layer. *Journal of Fluid Mechanics*, pp.1–12.

Hosseini, S.M. et al., 2013. Stabilization of a swept-wing boundary layer by distributed roughness elements. *Journal of Fluid Mechanics*, 718, pp.1–11. Available at: http://www.journals.cambridge.org/abstract_S0022112013000335 [Accessed July 31, 2013].

Imayama, S., Alfredsson, P.H. & Lingwood, R.J., 2012. A new way to describe the transition characteristics of a rotating-disk boundary-layer flow. *Physics of Fluids*, 24(3), p.031701.

Imayama, S., Henrik Alfredsson, P. & Lingwood, R.J., 2013. An experimental study of edge effects on rotating-disk transition. *Journal of Fluid Mechanics*, 716, pp.638–657.

Itoh, N., 1996. Simple cases of the streamline-curvature instability in three-dimensional boundary layers. *Journal of Fluid Mechanics*, 317, pp.129–154.

Jarre, S., Le Gal, P. & Chauve, M.P., 1991. Experimental Analysis of the Instability of the Boundary Layer over a Rotating Disk . *Europhysics Letters*, 14(7), pp.649–654.

Jarre, S., Le Gal, P. & Chauve, M.P., 1996a. Experimental study of rotating disk flow instability. II. Forced flow. *Physics of Fluids*, 8(11), p.2985.

Jarre, S., Le Gal, P. & Chauve, M.P., 1996b. Experimental study of rotating disk instability. I. Natural flow. *Physics of Fluids*, 8(2), p.496.

Kármán, T. V, 1921. Über laminare und turbulente Reibung. *ZAMM - Journal of Applied Mathematics and Mechanics / Zeitschrift für Angewandte Mathematik und Mechanik*, 1(4), pp.233–252.

Kobayashi, R., Kohama, Y. & Takamadate, C., 1980. Spiral vortices in boundary layer transition regime on a rotating disk. *Acta Mechanica*, 35(1-2), pp.71–82.

Kohama, Y., 1987. Some Expectation on the Mechanism of Cross-Flow Instability in a Swept Wing Flow. *Acta Mechanica*, 66, pp.21–38.

Kohama, Y., 1984. Study of boundary layer transition of a rotating disk. *Acta Mechanica*, 199, pp.193–199.

Lessen, M. & Gangwani, S.T., 1976. Effect of small amplitude wall waviness upon the stability of the laminar boundary layer. *Physics of Fluids*, 19(4), p.510.

Leventhal, L. & Reshotko, E., 1981. Preliminary experimental study of disturbances in a laminar boundary-layer due to distributed surface roughness. *Final Report Case Inst. of Tech., Cleveland, OH. Dept. of Mechanical and Aerospace Engineering.*, 1.

Lilly, D.K., 1966. On the instability of Ekman boundary flow.pdf. *Journal of the Atmospheric Sciences*, pp.481 – 494.

Lingwood, R.J., 1995a. Absolute instability of the boundary layer on a rotating disk. *Journal of Fluid Mechanics*, 299(-1), p.17.

Lingwood, R.J., 1996. An experimental study of absolute instability of the rotating-disk boundary-layer flow. *Journal of Fluid Mechanics*, 314(-1), p.33.

Lingwood, R.J., 1995b. Stability and Transition of the Boundary Layer on a Rotating Disk. *Thesis*.

Lufthansa-Technik, 2013. Like a shark in the water. Available at: http://www.lufthansa-technik.com/en/multifunctional-coating [Accessed May 7, 2013].

MacDonough, R.N. & Whalen, A.D., 1995. *Detection of Signals in Noise*, Academic Press.

Mack, L., 1985. The Wave Pattern Produced by a Point Source On A Rotating Disk. *AIAA Journal*.

Malik, M.R., 1981. Instability and transition in rotating disk flow. *NASA Contractor Report*.

Malik, M.R., 1986. The neutral curve for stationary disturbances in rotating-disk flow. *Journal of Fluid Mechanics*, 164(-1), p.275.

Malik, M.R., Wilkinson, S.P. & Orszag, S.A., 1981. Instability and transition in rotating disk flow. *AIAA Journal*, 19, pp.1131–1138.

Miklavcic, M. & Wang, C.Y., 2004. The flow due to a rough rotating disk. *Zeitschrift fur Angewandte Mathematik und Physik (ZAMP)*, 55(2), pp.235–246.

Nikuradse, J., 1933. Strömungsgestze in rauhen Rohren. *VDI-Forsch*, 361.

Owen, J.M. & Rogers, R.H., 1989. Flow and heat transfer in rotating-disc systems.

Le Palec, G. & Rondot, P.N.A.D., 1990. Study of laminar heat transfer over a sinusoidal-shaped rotating disk. *Int. J. Heat Masa Transfer*, 33(6), pp.1183–1192.

Pfenninger, W., 1946. *Untersuchungen {ü}ber Reibungsverminderungen an Tragflugeln, insbesondere mit Hilfe von Grenzschlichtabsaugung*, Verlag AG. Gebr. Leemann.

Pier, B., 2007. Primary crossflow vortices, secondary absolute instabilities and their control in the rotating-disk boundary layer. *Journal of Engineering Mathematics*, 57(3), pp.237–251.

Prandtl, L., 1938. Zur Berechnung der Grenzschichten. *ZAMM - Journal of Applied Mathematics and Mechanics / Zeitschrift für Angewandte Mathematik und Mechanik*, 18(1), pp.77–82. Available at: http://dx.doi.org/10.1002/zamm.19380180111.

Radeztsky, R.H., Reibert, M.S. & Saric, W.S., 1999. Effect of Isolated Micron-Sized Roughness on Transition in Swept-Wing Flows. *AIAA Journal*, 37(11), pp.1370–1377.

Rayleigh, Lord, 1879. On the stability, or instability, of certain fluid motions. *Proceedings of the London Mathematical Society*, 1(1), pp.57–72.

Reed, H.L. & Saric, W.S., 1989. Stability of Three-Dimensional Boundary Layers. *Annual Review of Fluid Mechanics*, 21(1), pp.235–284.

Reibert, M.S. et al., 1996. Experiments in nonlinear saturation of stationary crossflow vortices in a swept-wing boundary layer. *AIAA paper*, 184, p.1996.

Reshotko, E., 1984. Laminar flow control-Viscous simulation. *AGARD Spec. Course on Stability and Transition of Laminar Flow*.

Samad, A. & Garrett, S.J., 2010. On the laminar boundary-layer flow over rotating spheroids. *International Journal of Engineering Science*, 48(12), pp.2015–2027.

Saric, W.S., Carpenter, A.L. & Reed, H.L., 2011. Passive control of transition in three-dimensional boundary layers, with emphasis on discrete roughness elements. *Philosophical transactions. Series A, Mathematical, physical, and engineering sciences*, 369(1940), pp.1352–64.

Saric, W.S., Carrillo, R. & Reibert, M.S., 1998. Leading-edge roughness as a transition control mechanism. *AIAA Paper*, 781.

Saric, W.S., Reed, H.L. & White, E.B., 2003. Stability and Transition of Three-Dimensional Boundary Layers. *Annual Review of Fluid Mechanics*, 35(1), pp.413–440.

Schlichting, H., 1933. Zur Enstehung der Turbulenz bei der Plattenstromung. *Nachrichten von der Gesellschaft der Wissenschaften zu Gottingen, Mathematisch-Physikalische Klasse*, 1933, pp.181–208.

Schlichting, H. & Gersten, K., 2004. *Boundary-layer theory* 8th ed., Springer.

Sirovich, L. & Karlsson, S., 1997. Turbulent drag reduction by passive mechanisms. *Techniques*, (February), pp.728–730.

Smith, N.H., 1946. Exploratory investigation of laminar-boundary-layer oscillations on a rotating disk. *NACA*, 4.

Tatro, P.R. & Mollo-Christensen, E.L., 1967. Experiments on Ekman layer instability. *Journal of Fluid Mechanics*, 28(03), p.531.

Tollmien, W., 1928. Uber die Entstehung der Turbulenz. 1. Mitteilung. *Nachrichten von der Gesellschaft der Wissenschaften zu Gottingen, Mathematisch-Physikalische Klasse*, 1929, pp.21–44.

Vajravelu, K. & Prasad, K. V, 2013. *Keller-Box Method and Its Application*, Walter De Gruyter Incorporated.

Visser, F.C., Brouwers, J.J.H. & Jonker, J.B., 1999. Fluid flow in a rotating low-specific-speed centrifugal impeller passage. , 24, pp.275–292.

Wang, J., Lan, S. & Chen, G., 2000. Experimental study on the turbulent boundary layer ow over riblets surface. *Fluid Dynamics Research*, 27, pp.217–229.

Watanabe, K., Ogata, S. & Uemura, K., 2007. Drag Reduction of an Enclosed Rotating Disk with Fine Spiral Grooves. *Journal of Environment and Engineering*, 2(1), pp.97–107.

Watanabe, T., 1987. Effect of Surface Roughness on a boundary layer transition in a rotating disk. *Transactions of the Japan Society of Mechanical Engineers B*, 55(515).

Watanabe, T., Warui, H.M. & Fujisawa, N., 1993. Effect of distributed roughness on laminar-turbulent transition in the boundary layer over a rotating cone. *Experiments in Fluids*, 14(5), pp.1988–1990.

Wazzan, A.R., Okamura, T. & Smith, A.M.O., 1968. The Stability of Water Flow Over Heated and Cooled Flat Plates. *Journal of Heat Transfer*, 90(1), pp.109–114.

Wilkinson, S.P. & Malik, M.R., 1985. Stability Experiments In the Flow Over a Rotating Disk. *AIAA Journal*, 23(4), pp.588–595.

Yoon, M.S., Hyun, J.M. & Park, J.S., 2007. Flow and heat transfer over a rotating disk with surface roughness. *International Journal of Heat and Fluid Flow*, 28(2), pp.262–267.

Zoueshtiagh, F. et al., 2003. Laminar-turbulent boundary-layer transition over a rough rotating disk. *Physics of Fluids*, 15(8), pp.2441–2444.